2019

Nanoscale Functional Imaging by Tailoring Light-matter Interaction to Explore Organic and Biological Systems

Negar Otrooshi
University of Central Florida

NANOSCALE FUNCTIONAL IMAGING BY TAILORING LIGHT-MATTER INTERACTION TO EXPLORE ORGANIC AND BIOLOGICAL SYSTEMS

by

NEGAR OTROOSHI

B.S. Azad University Tehran Central Branch, 2008
M.Sc. University of Tehran, 2012
M.Sc. University of Central Florida, 2015

A dissertation submitted in partial fulfillment of the requirements
for the degree of Doctor of Philosophy
in the Department of Physics
in the College of Science
at University of Central Florida
Orlando, Florida

Spring Term

2019

Major Professor: Laurene Tetard

ABSTRACT

Probing molecular systems with light has been critical to deepen our understanding of life sciences. However, conventional analytical methods fail to resolve small quantities of molecules or the heterogeneity in molecules assembled into complex systems. This bottleneck is mostly attributed to light diffraction limit. In recent years, the successful implementation of new approaches to achieve sub-wavelength chemical speciation with an Atomic Force Microscope (AFM) has paved the way to a deeper understanding of the effect of local composition and structure on the functional properties of a larger scale system. The combination of infrared light, to excite the vibrational modes of a sample, and AFM detection to monitor the resulting local photothermal expansion has emerged as a powerful approach. In this work, we explore new applications of AFM-infrared (IR) to further the understanding of proteins and bacterial cells.

We first consider the vibrational modes and secondary structure of proteins. We show that beyond the localized IR fingerprint of the system, light polarization could affect the response of the protein. To investigate this further, we combine the AFM-IR measurements with plasmonic substrates to tune the electromagnetic field. Using plasmonic structures, we map the electromagnetic field confinement using nanomechanical infrared spectroscopy. We detect and quantify, in the near field, the energy transferred to the lattice in the form of thermal expansion resulting from the heat generated. We compare the photothermal expansion patterns in the structures under linearly and circular polarized illumination. The results suggest the formation of hot spots, of great interest for biomolecules detection. Using a model system, poly-L-lysine, we show that the IR spectrum and the vibrational circular dichroism fingerprint of a chiral biological system can be probed at the nanoscale, far beyond the conventional limits of detection. The second

part of the study focuses on utilizing the capabilities of AFM-IR to investigate bacterial cells and their responses to nanoparticle-based treatments. We highlight the potential of these new capabilities to further dive into the fundamental molecular mechanism of antibacterial activity and of development of drug resistance. We conclude this work by providing a perspective on the impact nanoscale functional imaging and spectroscopy can have on life sciences and beyond.

To my husband Nima and my parents

ACKNOWLEDGMENTS

I would like to thank all those contributed to this achievement. First and foremost, I would like to thank my advisor, Dr. Laurene Tetard for giving me this opportunity to work on my idea and accomplish this work. It was her constant guidance that developed my research project and also helped me grow into the scientist that I am today. I would like to thank my committee members, Dr. Peale, Dr. Tatulian, and Dr. Santra, whose inputs have helped me to stay on track with my research.

This work was accomplished in collaboration with several researchers. I would like to thank to Dr. Abraham Vazquez Guardado from the UCF College of Optics (CREOL) for fabricating the cavity-coupled achiral microdisks, and for personal communications on the topic. I would like to thank Dr. Santra and his students Mitsushita and Ali for providing the bacteria and synthesizing the nanoparticles for antibacterial treatments. I would like to thank the University of Central Florida, the Department of Physics and also the Nanoscience Technology Center for providing numerous opportunities to pursue this work. I would like to thank all my teachers and mentors, who have taught me and helped me to get to this level.

Lastly, I would like to thank my family, lab members, and friends. I would like to thank my husband, Nima, and my parents who always believe me and support me. I would like to thank all my amazing lab members, specifically Mikhael, Briana, Fernand, Raphael, Chance and Ahmad. Lastly, I would like to thank my friends, who are like my sisters, Javaneh, Haleh, Nahal, Fereshteh, and Mina.

TABLE OF CONTENTS

LIST OF FIGURES

CHAPTER 1 INTRODUCTION

1.1 Motivation

The development of telescopes and optical microscopes to track natural phenomena marked a new era of science. Galileo Galilei first used a telescope in 1610 to observe mountains and craters on the moon, which marked the beginning of the field of astronomy [1]. At the end of the seventeenth century, Antony van Leeuwenhoek and Robert Hooke used optical microscopy to explore biological systems such as plant tissues and microorganisms (bacteria, protozoans) [2] . Before this critical step, only biological objects that were visible to the naked eye could be considered. Overall, even today, scientific instrument developments are necessary to enable the discovery of important fundamental phenomena in Nature.

In recent years, tools to explore material properties at the nanoscale have emerged. They have transformed our understanding of physics, chemistry and biology. More recently, new progress in studying light-matter interactions at the nanoscale, notably benefiting from technological development allowing bypassing the conventional diffraction limit of optical instruments, have paved the way to exploring chemical and optical properties of complex systems at a level that has never been used before. Complementing imaging and spectroscopy, nanoscale synthesis, fabrication system (lithography, focused ion beam), or manipulation (optical tweezers) make it possible to design and control systems at a level that is suitable to systematically investigate previously unexplored empirical laws.

The introduction of Scanning Probe Microscopy (SPM), particularly with Atomic Force Microscopy (AFM), has been critical in breaching the frontiers between physics and biology. Atomic force microscopy is currently one of the only techniques capable of reaching sub-10 nanometer resolution under physiological conditions, which constitutes a paradigm shift in our understanding of living systems and their constituents. Beyond the morphology of system in their native environments, AFM is an extremely versatile. For instance, Scheuring et al [3] previously reported nanodissection to investigate the subunits of the reaction center of multiprotein photosynthetic systems in plants. The first nanodissection reported consisted in pulling DNA by tuning the applied force of with the AFM very precisely to unfold chromosomes [4, 5] . The AFM tip has also been considered as a mechanical scalpel to extract and manipulate macromolecular assemblies such as proteins [6-8]. A more common application of AFM is to investigate local mechanical properties of cells by indentation [9]. The investigation of cells, including mammalian, bacterial and plant cells [10], using multi-functional AFM probing has received significant attention in recent years. AFM can provide a three-dimensional profile of living cell in their physiological environment [11, 12]. Despite the wealth of information provided by AFM measurements on biological systems, to date, AFM alone cannot provide a complete picture of the system. Complementary techniques such as fluorescence imaging or optical spectroscopy often have to be performed to bridge the gaps of knowledge that remain uncharted with AFM. Chemical composition of a three-dimensional heterogeneous system such as a cell is one example of such a limitation.

The work presented in this dissertation pertains to characterization of biological sample at nanoscale with combining AFM with light to advance the fundamental understanding of biological systems from biomolecules, their secondary structures and the role they play is larger cellular systems.

1.2 Background

1.2.1 Chirality in life science

The secondary structure of a biomolecule holds is highly correlated to its functionality [13]. In Nature, a plethora of systems have specific similarities. For instance, most living creatures have pairs of ears or hands. A special rule of symmetry in natural systems is called *chirality*. A chiral system is not superimposable on its mirror image, such as a human hand. Chiral objects do neither have plane or center of symmetry.

In chemical terms, a molecule with a stereocenter (i.e., an atom bound to four different groups) is chiral. The most common chiral center is Carbon, Hence, chirality is recurrent in Nature at all scales, as in proteins, nucleic acids, amino acids, sugars, lipids, hormones, insects, plant, animal, or marine life, etc. The mirror image of a chiral molecule is called an enantiomer. Enantiomers exhibit significantly different functions in biology, as we will discuss in more details in Chapter 3. For this reason, understanding the chirality of biological systems and their correlation to functionality is very important for biology. For instance, the detection of chirality is very critical in drug formulation and in the food industry. This is because one enantiomer can be beneficial while its mirror image can have lethal human consequences. Thus, at the submicrometer scale,

determination of chirality could support our understanding and control of conditions for tragic, dramatic or triumphal consequences.

In Chapter 3, the state of the art of chiral biomolecules detection and identification will be discussed. The common technique to determine the chirality of molecules using far field measurements will be introduced. The review of the literature will illustrate the necessity of new approaches for the characterization of chirality at the nanoscale. A novel approach combining AFM and polarized infrared (IR) spectroscopy will be presented. The development of the proof-of-concept for this new measurement will be described in details. The viability will be confirmed using a model system poly-L-lysine.

1.2.2 Bacteria characterization at nanoscale

The need for advancing nanoscale characterization techniques expands to larger entities such as living cells. The ability to resolve smaller structures of a complex system to deepen the understanding of how local heterogeneities contribute to the overall activity of a biological ensemble is very timely. In microbiology, the relatively small size of bacteria limits the information that can be accessed using conventional microscopes [14]. Scanning electron microscopy (SEM)[15], transmission electron microscopy (TEM) [16] and SPM [17] have all been used for bacterial studies. However, although these techniques are capable of nanoscale resolution, they only provide morphological and structural information of the cells. Further, they are hindered by the requirements for image acquisition, such as the vacuum environment for electron microscopy. In addition, most approaches critically lack chemical speciation related to functional groups.

To address the growing need of understanding and controlling biological interactions in complex living systems, new advances in instrumentation are necessary. A new technique combining AFM and IR spectroscopy enables the investigation of the behavior of bacteria and their response to external stresses. The principle of this technique will be detailed in Chapter 2. In addition, its optimization and application to exploring the mode of action of selected antibacterial treatments will be discussed in Chapter 4.

1.3 Thesis overview

In this work, we will provide, in Chapter 2, an overview of all the instrumentation requirements and principles taken into account to carry out the work presented in the following chapters. Namely, IR spectroscopy, AFM and atomic force microscopy-Infrared spectroscopy (AFM-IR) will be described in details.

Moving forward, Chapter 3 focuses on the new technique to characterize the chirality of biomolecules at nanoscale. We will present the state of the art and discuss the limitations deterring nanoscale chirality measurements to date. A firsthand approach aiming at confining the electric field to enhance the molecular response of a chiral system for detection with an AFM – based nanomechanical measurement will be presented. The potential applications of the new platform for biology and pharmacology will be highlighted.

Chapter 4 deals with the multi-functional characterization of bacterial cells at the nanoscale. The bacterial cells treated with nanoparticles are investigated to identify the potential modes of action of the formulations. We discuss how AFM-IR technique can contribute to gain a more detailed

understanding of the interaction of nanoparticles and living systems to accelerate material design for health, but also to prevent toxicity and health concerns.

Finally, chapter 5 will conclude this work, with a general discussion of the implication of the advances presented in chapter 3 and 4. Future directions for each topic will also be considered.

CHAPTER 2 CHARACTERIZATION METHODS

In this chapter, we discuss the fundamental principle and technical implementation of the characterization methods used in Chapter 3 and 4. We first cover IR spectroscopy, followed by AFM, and we conclude with AFM-IR.

2.1 Infrared (IR) Spectroscopy

The IR region of the electromagnetic radiation spectrum extends from 700 nm to 1000 μm, which includes the near-infrared (700 nm-2.5 μm), mid-infrared (2.5-25 μm) and far-infrared (25-1000 μm) range. Photon energies of IR region are sufficient to excite vibrations in chemical bonds of materials and molecules. To explain the physical concept of IR spectroscopy, we first consider a poly-atomic (N-atoms) molecule, its degrees of freedom, and its different types of vibrational modes.

A molecule is defined as N atoms that are bound together via chemical bonds. A molecule can be homonuclear, which means that it is composed of one chemical element, such as N_2, or heteronuclear molecule, if it is composed of more than one element, such as CO_2. Chemical bonds and molecules are not rigid. In this sense, molecules can be modeled as a system of masses joined by springs. As a simple case, a diatomic (N=2) molecule behaves like a mass-spring-mass system, where each mass represents an atom and the spring represents their chemical bond.

The motion of a molecule in space is described in terms of degrees of freedom. For a molecule with N atoms, the total degree of freedom is 3N since each atom has three degrees of freedom. A

nonlinear molecule with N atoms has 3N-6 vibrational degrees of freedom as the 3 translational degrees of freedom in x, y, and z direction and 3 rotational degrees of freedom around x, y, and z axis do not contribute to vibrational modes. A linear molecule with N atoms may have 3N-5 vibrational degrees of freedom, as the 3 translational degrees of freedom in x, y, and z direction and 2 rotational degrees of freedom around two axes which are perpendicular to the linear molecule axis. For instance, H_2O is a nonlinear molecule with 3 degrees of rotational freedom, and CO_2 which is a linear molecule, only has 2 degrees of rotational freedom since there is no energy involved in rotation of molecule around O=C=O axis.

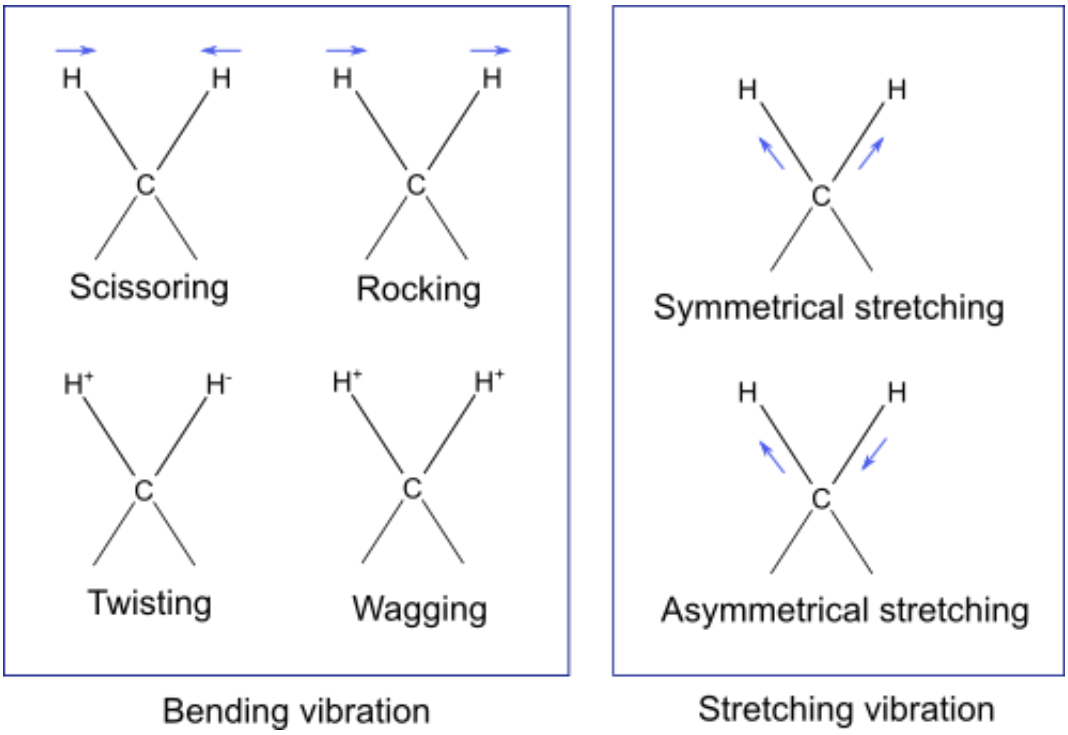

Figure 2.1 Left panel: Different types of bending vibration modes: scissoring, rocking, twisting, and wagging. Right panel: Fundamental stretching vibrations: symmetrical and asymmetrical stretching.

In the 3N-6 degrees of vibrational freedom, there are different fundamental modes of vibrations such as stretching, scissoring, rocking, twisting, and wagging which contribute to the IR spectrum of molecules.

Stretching: Stretching is defined as a change in bond length. There are two different types of stretching, symmetrical and asymmetrical. In symmetrical stretching vibration, similar bonds attached to an atom move away and toward the common atom simultaneously. In asymmetrical stretching vibrations, one bond moves away from the common atom while the other bond moves toward the common atom as shown in Figure 2.1 (right panel).

Scissoring: This vibrational mode is called in-plane bending. The bonds motion, in-plane, deforms the bond angle as shown in Figure 2.1 (left panel).

Rocking: The bonds swing to the left and right simultaneously as the atoms stand in the same plane as shown in Figure 2.1 (left panel).

Twisting: The bonds twist out of plane around the common atom as shown in Figure 2.1 (left panel).

Wagging: The bonds swing back and forth together and simultaneously out of plane of the bond as shown in Figure 2.1 (left panel).

As shown in Figure 2.1, stretching vibrations are in the direction of the bonds, while bending vibrations such as rocking, scissoring, twisting, and wagging change the angle between the bonds.

The theory associated with IR spectroscopy stems from work presented in the 19th century. Einstein, Bohr, and Planck showed that electromagnetic radiations are composed of quanta of energy, which is explained by Bohr equation E=hν where h is the Plank constant ($h = 6.62 \times 10^{-34}\ Js$) and ν is the frequency. Vibrations and rotations of bonds associated with IR excitation can be represented via quantized discrete energy levels, E_0 , E_1 , E_2, ... as shown in Figure 2.2. When a molecule is irradiated with light, if the quantum of energy (photon hν) is absorbed, the system is excited to an excited state ($if E_i - E_j = h\nu$, i, j =1, 2, 3,…). Quantum mechanics ought to be considered as well. Development of quantum mechanics led to the creation of a model of spring-mass system for a chemical bond described by a simple harmonic oscillator, whose potential energy is modeled as a parabola with discrete energy levels as shown in Figure 2.2 (green line). The harmonic oscillator has discrete energies $E_n = \left(n + \frac{1}{2}\right) \hbar\omega$, where n is an integer, ħ = $\frac{h}{2\pi}$ (h if the Planck's constant) and ω is the angular frequency of the oscillator. The energy levels of the harmonic oscillator are uniformly spaced as $\Delta E = \hbar\omega$. However, a more realistic interatomic potential energy involves a more complex anharmonic oscillator, as shown in Figure 2.2 (blue line). In the anharmonic oscillator model, the lowest energy levels can be considered as evenly spaced as in the harmonic oscillator whereas the energy spacing decreases as higher energies closer to the dissociation energy D_0, as shown in Figure 2.2 b.

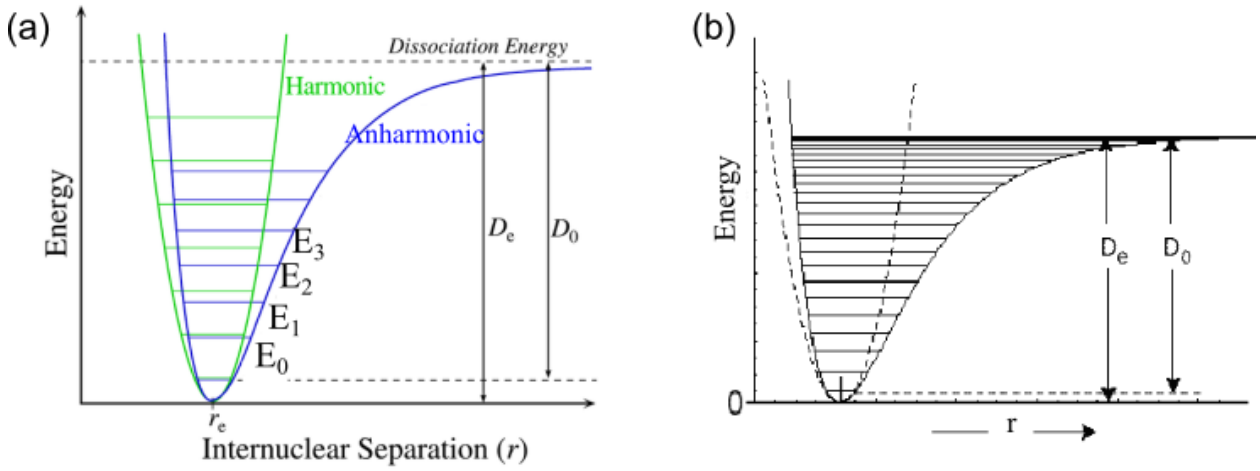

Figure 2.2 a) Quantized discrete energy levels E_0 , E_1 , E_2, ... of vibrations of molecule in the system modeled as a harmonic (green line) and anharmonic oscillator (blue line). b) The anharmonic potential energy shows decreasing ΔE at higher energies. D_e is the well depth and it is defined as dissociation energy of the bond, D_0 is defined as a true energy to dissociate the bond from the lowest energy E_0.

Quantum mechanics imposes some selection rules on vibrational transitions. A molecule is IR active if its electric dipole moment ($\vec{\mu}$) changes during the vibration mode considered. As shown in Figure 2.3 a, for a heteronuclear diatomic IR active molecule, the dipole moment changes when its bond expands and contracts. In physics, the direction of $\vec{\mu}$ is defined from the electronegative toward the electropositive charge. Electronegativity is a measure of an atom's ability to attract electrons and electropositivity is a measure of an atom's ability to donate electrons. Since $\vec{\mu}$ is a vector quantity, a molecule such as CO_2 has no dipole moment if the two

C=O bonds are stretched symmetrically as shown in Figure 2.3 b. In such a case, the symmetrical stretching vibration mode is considered IR inactive. If the bonds stretch asymmetrically, the transition is IR active as $\vec{\mu}_{total} \neq 0$ (Figure 2.3 b). The full derivation of the selection rules has been presented in multiple textbooks [18-20].In essence, the derivations describes the induced electric or magnetic field moment in a molecule due to a given light excitation. When the frequency of the induced moment matches the energy difference between two eigenstates of the system, the system is in resonance. Using Born-Oppenheimer approximation, the electronic and vibrational selection rules can be expressed. The derivation leads to the $\Delta\upsilon=\pm1, \pm2, \ldots$ for an anharmonic potential, where υ is the number of states, although the intensity of the IR bands is generally weaker as $\Delta\upsilon$ increases.

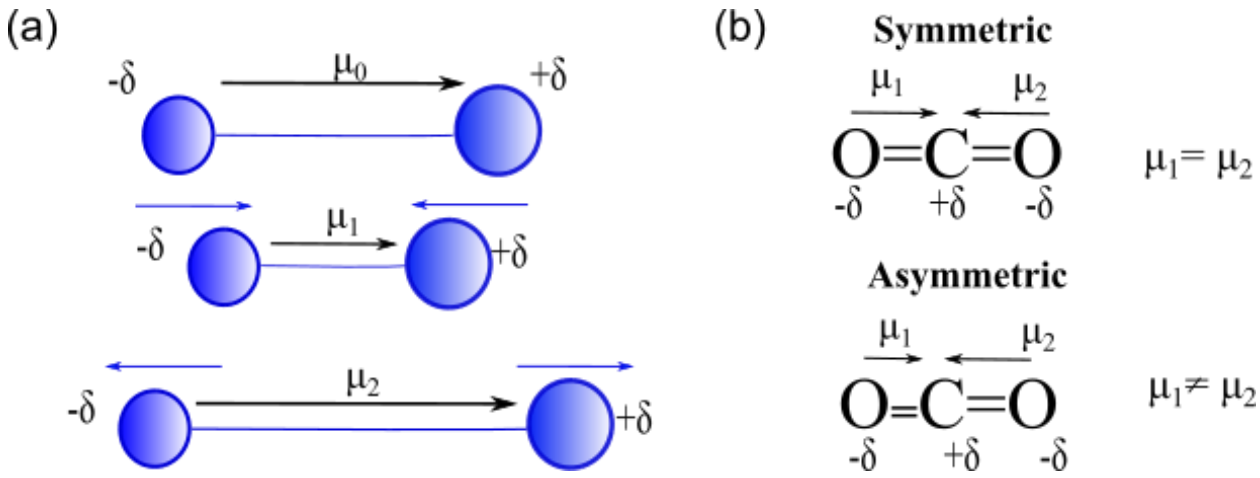

Figure 2.3 a) Change in the dipole moment μ of heteronuclear diatomic molecule, +δ and – δ indicate the electropositivity and electronegativity b) Symmetric and asymmetric vibrations of molecule CO_2.

The most common tool used for IR spectroscopy is a Fourier Transform Infrared (FTIR) spectrometer. In this configuration, a Michelson Interferometer [21] with fast Fourier transform (FFT) are implemented for faster data acquisition, analysis, and processing. This replaces the very first version of IR spectrometer, which used a prism as a dispersive element and measured absorption wavelength by wavelength [21]. In FTIR spectrometers, the incident infrared light passes through an interferometer and through the sample before the transmitted components reach the detector to form an IR spectrum. In the next section, the Michelson Interferometer is discussed in details.

2.1.1 Michelson Interferometer

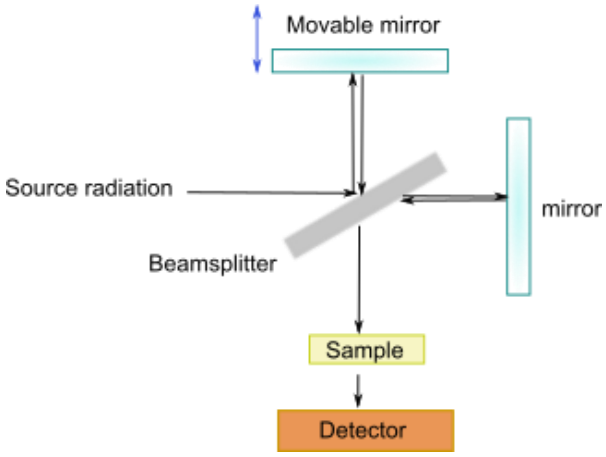

Figure 2.4 Schematic of Michelson Interferometer, which consists of two perpendicular mirrors, a beam splitter and a detector. One mirror is movable to create the optical path difference necessary for the interferogram.

A Michelson interferometer consists of two perpendicular mirrors as shown in Figure 2.4. One of these mirrors moves back and forth in a direction perpendicular to that of the second mirror.

When a beam of radiation passes through the beamsplittter, 50% of the incident radiation is reflected to the moving mirror and the other 50% of radiation is transmitted to the fixed mirror. When the two beams are reflected from the respective mirrors, they travel back to the beamsplitter, recombine and interfere. Recombination at the beamsplitter comprises a set of destructive or constructive interferences, depending on the optical path length difference (δ). The moving mirror is used to create the optical pathlength difference. If $\delta = n\,\boldsymbol{\lambda}$, the interference is constructive. If $\delta = \left(n + \frac{1}{2}\right)\boldsymbol{\lambda}$, the recombination results in a destructive interference. For a monochromatic source, the interferogram is represented by a cosine wave as shown in Figure 2.5 a. For a polychromatic radiation, such as the black body source used in FTIR spectrometers, the interferogram is more complex function, as shown in Figure 2.5 b. The interferogram is recorded as the light intensity (I) with respect to δ. Next, the beam passes through the sample which absorbs some of the energy due to its IR active bonds. The computer performs Fast Fourier transform (FFT) on the interferogram to produce the IR spectrum as shown in Figure 2.6.

After subtracting the background spectrum, which is the IR spectrum obtained in the same environmental conditions but without a sample, the IR spectrum representative of the sample is generated as shown in Figure 2.6 (right).

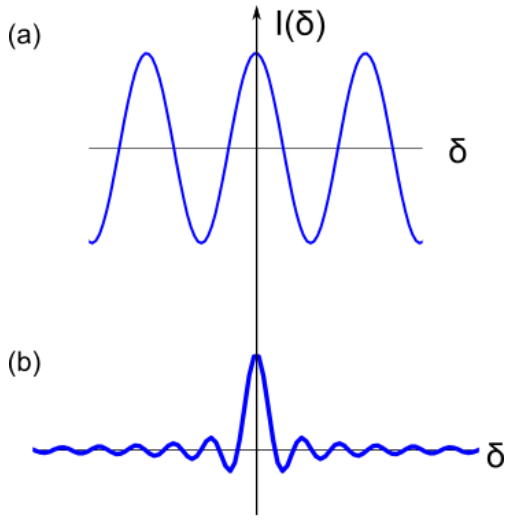

Figure 2.5 a) For a monochromatic source, the interferogram is represented by a cosine wave, b) For the black body source in FTIR spectrometer, the interferogram is more complex function recorded as function of the δ.

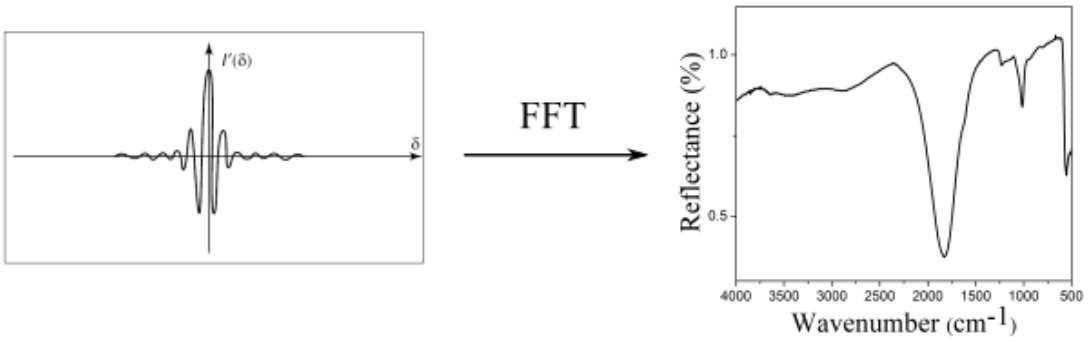

Figure 2.6 FFT transformation of interferogram into an IR spectrum in frequency domain.

Depending on the nature of the sample, FTIR spectrometer can be used in transmission or reflection mode. For non-transmitting samples, such as plasmonic, opaque sample, reflective measurements are required. The amount of radiation reflected off the surface of the sample can depend on some parameters such as angle of the incident beam, thickness, index of refraction, roughness and absorption properties of the material. The measurement does not take into account the orientation or twist of the secondary structure or crystallinity of the system. To probe this information, the light has to be polarized.

2.2 Polarization of light

Light can be described as a transverse electromagnetic wave. The electric and magnetic fields constitutive of light oscillate perpendicular to the direction of motion of the wave. For linear polarization, the plane of oscillation of the electric field corresponds to the polarization. For circular polarization, the electric field E components (E_x, E_y) oscillate in such a way that the electric field E vector rotates with a constant magnitude circularly around the direction of propagation in a right-handed coordinate system with x, y and z axes as shown in Figure 2.7. The light travels along the +z direction, and observer looks along the opposite direction of z (i.e. -z) toward the light source. The handedness of the circularly polarized light is defined by direction of rotation of E observed by this virtual observer. Circularly polarized light can rotate either in the clockwise (right-handed) or counter-clockwise (left-handed) direction. As shown in Figure 2.7, each circular polarization is composed of two orthogonal linear polarizations. Two components of the electric field E components (E_x, E_y) have same magnitude. For left-handed circularly polarized light, the phase shift of y component of electric field relative to the x

component is $\Delta\varphi = \pi/2$ (Figure 2.7.b), while for right-handed circularly polarized light, the phase shift is $\Delta\varphi = -\pi/2$ (Figure 2.7 a). Therefore, a clockwise rotation relates to the right-handed polarization while the counterclockwise rotation corresponds to the left-handed polarization.

.

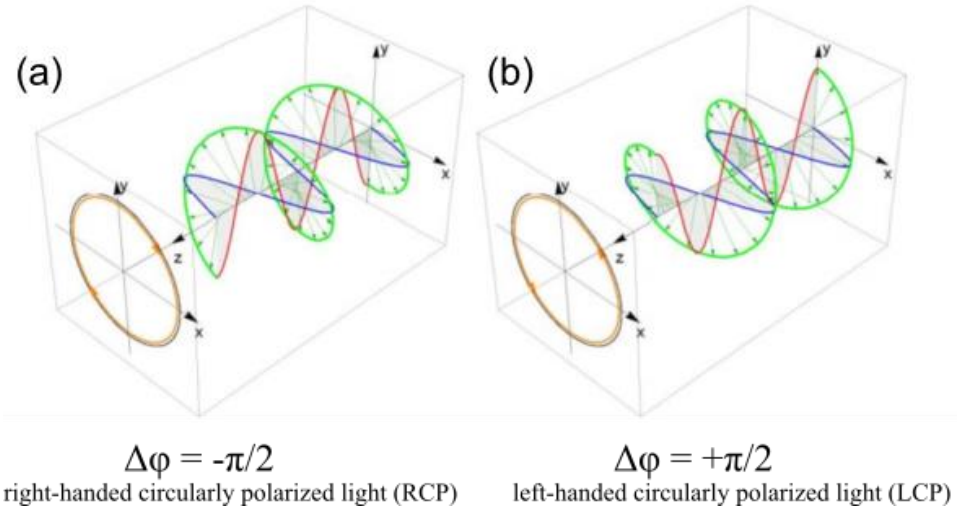

Figure 2.7 Circularly polarized for the cases a) $\Delta\varphi = -\pi/2$ (RCP) and b) $\Delta\varphi = \pi/2$ (LCP), $(E_x = E_y)$[22].

In order to convert a linear polarization of light into any other polarization, a retardation plate is required. Retardation plates or wave plates are polarization transformers. To transform linearly polarized light to circularly polarized light, a quarter waveplate is used. Quarter waveplate has two axes, labeled “fast” and “slow”. The plate is made of x- or y-cut uniaxially anisotropic material along fast and slow axes. The refractive indices along the fast and slow axes are different; thus, the phase velocity of the wave is different along each axis. As the light passes

through the quarter wave plate, the two components will have a phase delay because of difference in phase velocity. This phase retardation for quarter waveplate is $\pi/2$, which leads to circular polarization of the light. To polarize the light in the FTIR spectrometer, we take into account that the FTIR source emits unpolarized light. In chapter 3, we will discuss the use of a linear polarizer and a quarter waveplate to first change the FTIR unpolarized light to a linearly polarized light before polarizing the light circularly. The handedness of circular polarized light can be modified for circular dichroism (CD) spectroscopy as will be discussed in chapter 3, for nanoscale CD measurements.

2.3 Atomic Force Microscopy (AFM)

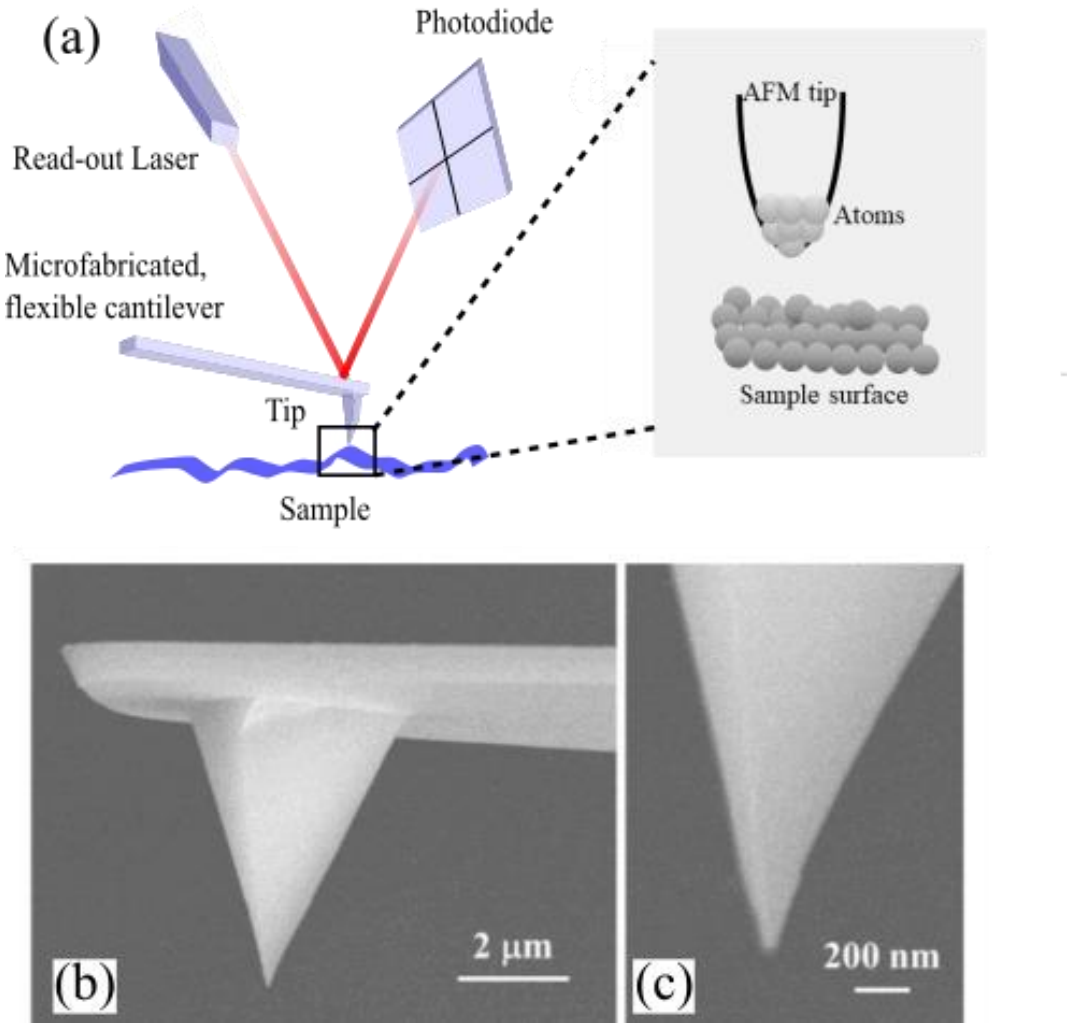

Figure 2.8 a). Schematic of Atomic Force Microscope (AFM), (b) and (c) Scanning electron microscope (SEM) image of Pt/Ir coated Si_3N_4 AFM probe taken from [23]

AFM is a technique commonly used to determine the morphology of a sample in three dimensions (X, Y and Z), with resolution up to the atomic range (angstrom) [24]. AFM can image systems from the condensed and soft matter family. The measurements are commonly performed in air but are also possible in liquid or vacuum environments [25]. Besides its imaging

capability, the AFM offers additional modules to measure various properties of a material with nanoscale resolution, such as its stiffness [26], its work function [27], its magnetic [28] or thermal [29] properties. For this reason, since its invention in the 1980s, the applications of AFM have reached a plethora of fields including physics [30-32], biology [33-36], chemistry [37, 38], nanotechnology[39, 40], and medicine [41, 42].

The nanoscale spatial resolution of AFM is enabled by a sharp tip (~ 5-20 nm in diameter) attached to a flexible microcantilever structure (with dimensions about tens of micrometer), as shown in SEM image in Figure 2.2.b. and c. Contact mode, intermittent-contact mode (also known as tapping mode) and peak-force imaging are currently the three main modes of imaging used for AFM.

To monitor the tip-sample interaction, the AFM is equipped with a read-out laser and a position sensitive photodiode detector (Figure 2.2 a). The read-out laser beam is used to track the cantilever deflection over time. The laser is aligned to the back end of cantilever structure and reflected to the detector. Any cantilever deflection due to a change in morphology results in a vertical translation of the position of the laser beam on the detector. The position sensitive photodiode detector records the changes (in volts), which are then converted into height measurement (in nm). The topography of the sample is acquired by scanning the AFM cantilever over the regions of interest of the sample. To control the cantilever scanning and the tip-sample distance, the AFM uses a piezoelectric transducer. The feedback control adjusts the tip-sample distance as it receives the signal from the detector to keep the cantilever deflection, amplitude or peak force at the desired setpoint, in contact, tapping and peak force modes respectively. The scanning operation of AFM is different for each mode of imaging.

In contact mode, the tip is in continuous contact with the surface of a sample while the probe scans the sample. The feedback control keeps the cantilever deflection at the defined value, to maintain a constant force (which is known as constant-force contact mode AFM). Thus, the deflection signal is corrected by adjusting the height via Z-piezo displacement of the scanner. The change in deflection of the cantilever is directly converted in a topography map of the sample. In our study, we carried out all measurements in constant-force contact mode.

In tapping mode, the AFM cantilever is oscillated at one of its resonance frequencies with an additional piezoelectric element built-in the AFM holder. The AFM tip touches the sample periodically. This scheme reduces the frictional forces exerted on the sample. The cantilever is driven at or close to one of its resonance frequencies using the piezoceramic (piezo) component incorporated in the AFM cantilever holder. The piezo is driven at constant amplitude. As the cantilever approaches the sample surface the amplitude of the cantilever oscillations decreases. This is used to control the force applied to the sample for imaging. During imaging, the amplitude, phase and frequency of the oscillation can be monitored. The feedback control generally acts to maintain the amplitude of oscillation at the setpoint. The AFM controller achieves this by adjusting the height via Z-piezo of the scanner.

2.3.1 The physics behind tip-sample interactions

The interatomic and intermolecular forces at play between the cantilever tip and the sample surface will be discussed next.

2.3.1.1 Attractive forces

Van der Waals forces, which encompass Keesom forces, Debye forces, and London (or dispersion) forces, most commonly describe attractive forces in AFM. They represent dipole-dipole interactions. The dipole can be permanent or induced.

The Keesom force represents the permanent dipole–permanent dipole electrostatic interaction between two atoms or molecules. This interaction is temperature dependent because thermal energy causes dipoles to fluctuate. So, a weighted average using classical Boltzmann statistics is required. The interaction energy *or Keesom energy* between two dipoles is calculated by the thermal average over different rotational orientations (over θ and φ) [24, 43].

The Debye force is the permanent dipole-induced dipole interaction between two atoms or molecules. A molecule with permanent dipole induces a dipole in adjacent molecule. For example, if the molecules of the surface of the sample have permanent dipoles, they can induce dipole moments in the AFM tip (which is usually oxidized) and vice versa [24, 43].

The London or dispersion force is the induced dipole-induced dipole interaction between two atoms or two molecules. This force is the most important contributor to van der Waals forces and acts between all molecules. This type of interaction is caused by instantaneous dipole moments of atoms or molecules due to random fluctuations of their electron density in their electron clouds [24, 43].

The potential energies associated with these three forces vary as $\frac{1}{r^6}$, where r is the separation of atoms or molecules. After adding the potential energies of these three forces, the potential

energy of van der Waals force is proportional to ($\frac{-C}{r^6}$), where C is a constant and r is the separation of atoms or molecules (see "blue" dashed line curve in Figure 2.3.a) [24, 43].

2.3.1.2 Repulsive forces

Repulsive forces in an AFM measurement are commonly described as the Pauli Exclusion Principle, which determines how close two atoms or molecules can ultimately approach each other. This principle is quantum mechanics in origin, as electrons of atom A and electrons of atom B cannot occupy the same energy states. The potential energy of the repulsive force varies as $\frac{1}{r^{12}}$, where r is the separation of atoms (see "black" dashed curve in Figure 2.9.a)[24].

2.3.1.3. Lennard-Jones potential

Taking into account the attractive and repulsive forces between to tip and the sample, the potential energy can be described using the Lennard- Jones potential as shown in Figure 2.9.a. The Lennard-Jones potential is expressed by:

$$U(r) = 4\,U_0\,[\left(\frac{\sigma}{r}\right)^{12} - \left(\frac{\sigma}{r}\right)^{6}] \qquad (1)$$

Where r is the distance between two atoms, U_0 is the depth of potential (minimum of potential energy) and σ is the value at which $U(r = \sigma) = 0$, as shown in Figure 2.9.a.

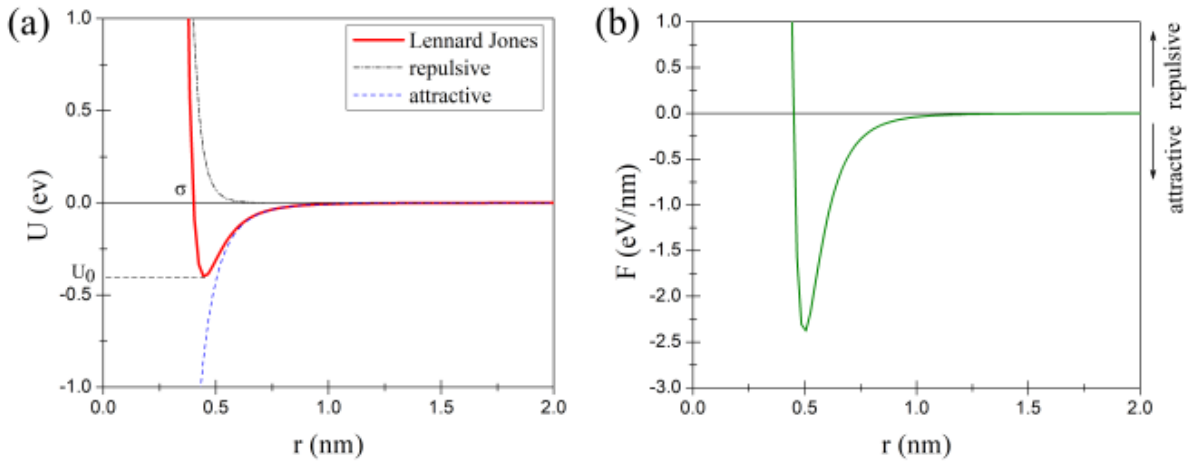

Figure 2.9 Potential energy and forces at play between the AFM tip and the sample. (a) The Lennard-Jones interatomic potential overlaid with attractive van der Waals ($\frac{1}{r^6}$) (blue dashed line) and repulsive ($\frac{1}{r^{12}}$) (black dashed line) energies. (b) Corresponding force-distance curve.

When the tip is far from the sample (i.e., when r is large) the potential energy tends to zero. As the tip approaches the sample, the attractive forces become dominant, corresponding to a potential energy $U(r) \propto -\left(\frac{\sigma}{r}\right)^6$. As the tip continues its motion toward the sample, it eventually jumps into contact with the surface of the sample. After this, the repulsive forces become dominant, with a potential energy $U(r) \propto \left(\frac{\sigma}{r}\right)^{12}$. When imaging in AFM contact mode, the distance between the tip and the sample remains small, most often in the repulsive force region. When imaging in tapping mode, the tip-sample varies during each oscillation of the cantilever. As the distance between the atoms of the tip and surface of the sample decreases, the interaction can span the predominantly attractive and repulsive regions, depending on the amplitude of the cantilever oscillation [44].

Experimentally, the tip-sample interactions are often studied using a force-distance curve, as shown in Figure 2.9.b ($F = -\frac{dU}{dr}$). Such a curve is obtained by monitoring the deflection of the cantilever as it approaches the sample surface. F = 0 represent the point at which the potential energy U is minimum.

Beyond indicating the nature of the forces, the force-curve provides the information about local material properties of the sample such as elasticity, adhesion and energy dissipated in the interaction [45-48]. New methods including Peak Force QNM [49] and nanoDMA [50] have emerged to improve the quantification of nanomechanical properties of materials using AFM. This aims to address one of the major drawbacks of AFM, which is that conventional AFM operation does not provide any compositional information about the sample.

In next section, we will discuss in more details one aspect of advances made in AFM-based technique in recent years to overcome this limitation of AFM for chemical speciation of the sample.

2.4 AFM-IR

Infrared spectroscopy has been recognized as an analytical approach that is compatible for implementation with AFM. As presented in previous sections, these two techniques are widely used in their respective fields of research. However, conventional IR spectroscopy has two main drawbacks: low intensity of thermal IR source and spatial resolution limit set by the optical diffraction limit, of about $\lambda/2$ where λ is wavelength of the IR source. In the mid-IR range, this would constitute a spatial resolution of about $\sim 2 - 5\ \mu m$. Atomic force microscopy, on the other

hand, can reach nanoscale spatial resolution, but is limited by lack of chemical information as described in the previous section.

A new approach coined AFM-IR overcomes these limitations by providing the chemical information of IR spectroscopy with high spatial resolution of AFM. Hammiche et al. [51] in the UK and Anderson [52] at the US Jet Propulsion Laboratory first proposed to combine AFM and IR spectroscopy. They both used commercial FTIR as an IR source and coupled the IR excitation to the AFM tip-sample system. A most recent AFM-IR technique was developed by Dazzi et al. [10, 11, 53] who applied a tunable free electron laser to excite IR absorption modes in the sample. Dazzi's work, coined Photothermal Induced Resonance (PTIR) was patented (U.S. patent 11/803421) and later licensed for commercialization.

As shown in Figure 2.10, the IR illumination is focused at the AFM tip apex. When the wavelength of the laser corresponds to the absorption band of the material probed, the light is absorbed. The heat released during the process of vibrational excitation causes the temperature to rise in the excited region, resulting in thermal expansion of the material. To achieve a detectable signal that can be probed with the AFM, the illumination is modulated. Hence the IR lasers used for this measurement are pulsed. The first implementation of AFM-IR used an IR source with low repetition rate, at about few Hz. It was performed by Dazzi using a free electron laser at the Synchrotron SOLEIL in Paris [11]. Later, an optical parametric oscillator (OPO) laser with 1 kHz pulse rate was developed to provide a benchtop adaptation of the AFM-IR. This system was commercialized by Anasys Instrument (now Bruker) in the early 2010s. The newest version of the AFM-IR was modified to use a high repetition rate tunable pulsed laser source. This can be obtained with a quantum cascade laser (QCL). This makes it possible to tune the laser pulse with

the resonance of the cantilever, thus increasing the signal to noise ratio. The thermal expansion increases for the duration of the laser pulse, after that, the sample temperature decreases exponentially to the ambient temperature. The rate of temperature decay depends on the thermal properties of the sample. This thermal expansion exerts a force on the cantilever that is related to the cantilever deflection. The pulse of light, especially when tuned to the cantilever resonance, sets the cantilever into oscillations. This process can also be referred to as "ringing" of the cantilever, as shown in Figure 2.10 b.

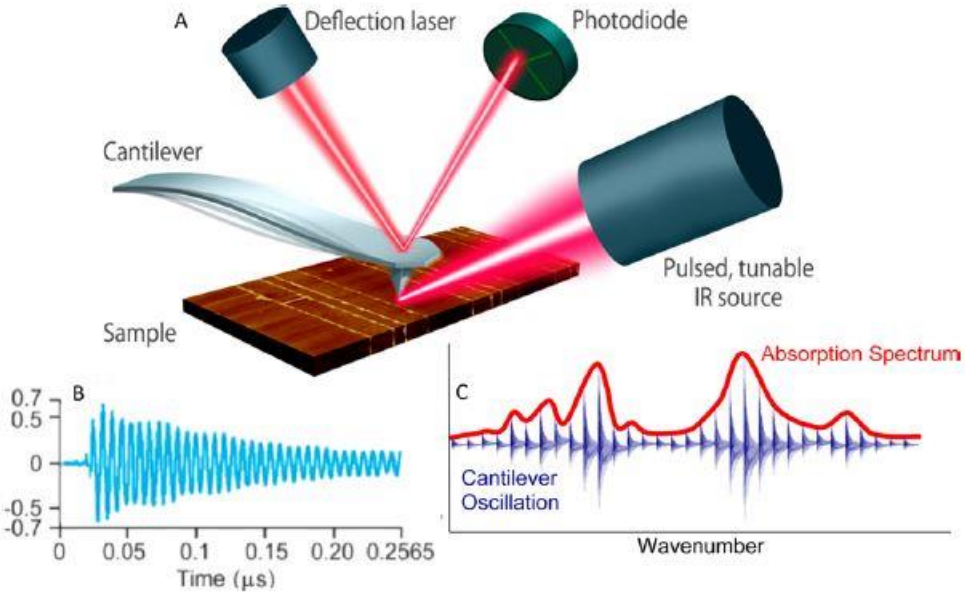

Figure 2.10 a) AFM-IR schematic, pulsed tunable laser source is focused on a sample near the AFM cantilever tip. The AFM probe is used as an IR absorption detector the cantilever response to the actuation is detected by the read-out laser and the photodiode. (b) Cantilever oscillation resulting from the force impulse of the IR laser exciting the sample. (c) Representative AFM-IR

spectrum illustrating how the amplitude of the cantilever oscillations recorded at each pulse corresponds to the IR fingerprint of the material [10].

When applying a Fourier Transform on the "ringing" signal, the signal indicates multiple frequencies of oscillations are contained in the cantilever response. These are due to the multiple eigenmodes of the cantilever beam structure [10, 53]. The eigenmodes of cantilevers correspond to the contact resonance of cantilever during AFM-IR measurements, as the tip contacts the sample surface for all measurements presented in this work. We note that the frequency of contact resonances provides complementary information about the mechanical properties of the material in contact with the tip [10, 53].

Overall, it has been previously reported that the AFM-IR signal depends on several material properties such as thermal expansion coefficient, heat capacity, density, and Young's modulus [10]. The detailed understanding of how these properties affect the signals measured remains an active area of research. For instance, it has previously been discussed that the contact resonance frequencies of cantilever can shift due to temperature dependent stiffness of some materials [53]. To circumvent this limitation, the amplitude and the peak position of the selected eigenmode are both monitored during chemical measurements [10]. It has also been found that higher eigenmodes tend to offer better signal to noise ratio in presence of heating of the air around the cantilever [10].

Despite the continued need for fundamental understanding of the instrumentation, AFM-IR has already impacted numerous fields of applications, particularly in life science researches for protein folding [12], nanoscale chemical imaging of tissues [54], or protein secondary structure

[55]. Additional applications such as photonic, semiconductor, and pharmaceutical systems have also been reported [56-61].

2.4.1. AFM-IR theoretical overview

The principle of AFM-IR is based on the premise that IR light can be tuned to excite vibrational modes in the samples. In turn, a part of the light absorbed is converted into heat and dissipated through the system. The heat dissipated causes a local and transient dilatation of the material that releases thermal stress, which can be detected by the AFM probe in contact with the sample surface. In this section, we discuss the theoretical landscape accompanying this measurement. The discussion here is adapted from the analytical model presented by Dazzi et al in 2010 [62].

The optical properties of a material are generally defined by its complex refractive index,

$$\tilde{n}\,(\lambda) = n(\lambda) + \mathrm{i}\,K(\lambda) \qquad (2)$$

where n(λ) is the real part, also referred to as refractive index, while K(λ), the imaginary part, is referred to as the extinction coefficient. λ corresponds to the wavelength of light hereafter.

"Spectroscopy", which consists in evaluating the different energies (or wavelength) absorbed by a sample illuminated with light, has been formalized, for the case of light absorption, in the Beer-Lambert law for an infinite layer of a material of thickness *d*:

$$Abs(\lambda) = \frac{4\pi d}{\lambda}\, Im\,(\tilde{n}\,(\lambda)\,) \propto \frac{1}{\lambda}\, Im\,(\tilde{n}\,(\lambda)\,) \qquad (3)$$

where λ is the wavelength of the incident light and $Abs(\lambda)$ is the absorption of the material at λ. This expression indicates that the absorption of a material is proportional to the imaginary part of

the refractive index, i.e. to the extinction coefficient K(λ), and inversely proportional to the wavelength λ.

The Poynting's theorem is used to describe the power delivered to the volume of a material. The theorem states that this power, representing the rate of gain in energy, is equal to the sum of the rate of loss of electromagnetic energy stored in the fields within the volume considered and of the rate of energy transported out of the volume. To describe AFM-IR, Dazzi et al formulate two approximations about the system:

1) the sample size (or volume probed in the measurement) is smaller than the wavelength, leading to the approximation that the electric field is constant in the volume considered, and

2) the sample absorption corresponding to vibrational modes in the sample is weak, suggesting that $Re\ (\tilde{n}^2) \gg Im\ (\tilde{n}^2)$.

Based on these considerations, the power absorbed by the sample, P_{abs} , is formulated as:

$$P_{abs} = \frac{2\pi c}{\lambda}\ \varepsilon_0\ \frac{9\ n\ .K}{[n^{\ 2}+2]^2}\ |E_{inc}|^2\ V \qquad (4)$$

where *n* and *K* represent the real and imaginary parts of $\tilde{n}$, respectively, E_{inc} represents the incident electric field, V the volume considered, *c* the speed of light and ε_0 the permittivity of free space.

Based on the approximation that n << K when λ corresponds to an IR absorption band of the sample, we find the common expression for IR spectroscopy:

$$P_{abs} \propto \frac{K}{\lambda}. \qquad (5)$$

P_{abs} will influence the temperature increase in the material. This can be described using Fourier law, as discussed by Dazzi et al [62]:

$$\rho C_p \frac{\partial T}{\partial t} = \frac{\Pi(t_p) * P_{abs}}{V} + k_{th} \Delta T \qquad (6)$$

where ρ is the density, V is the volume, C_p is the specific heat capacity and $k_{th}$is the heat conductivity of the sample. The other terms define the heating and temperature T of the sample during the laser irradiation, with $\Pi(t_p) * P_{abs}$ describing the laser shape to be rectangular using the Π rectangular box function of length t_p.

The duration of the pulse, which we note τ_p here, is critical to determine the processes at play in the material during excitation.

In the case of the OPO laser, the laser pulse of 5-20ns and the heat diffusion time (τ_{relax}) of the materials are shorter than the response of the cantilever in the microsecond range. Experimentally, it was determined that the sample retrieves its static states after ~ 0.5 ms. As a result, a pulse emitted every second, as with the OPO laser, has an effect on the sample that is independent from the previous pulse. In addition, if $\tau_p \ll \tau_{relax}$, the analytical work by Dazzi et al. indicates that:

$$\Delta T(t) = T_{max} \frac{t}{t_p} \qquad for\ 0 \ll t \ll t_p \qquad (7)$$

$$\Delta T(t) = T_{max}\, e^{\frac{t-t_p}{\tau_{relax}}} \qquad for\ t \geq t_p \qquad (8)$$

where T_{max} is the maximum temperature that can be reached in the system, and τ_{relax} can be derived based on the shape and composition of the sample.

Hence, the behavior temperature of the sample illuminated by a single laser pulse that is shorter than the thermal relaxation time of the sample can be represented as in the graph shown in Figure 2.11.

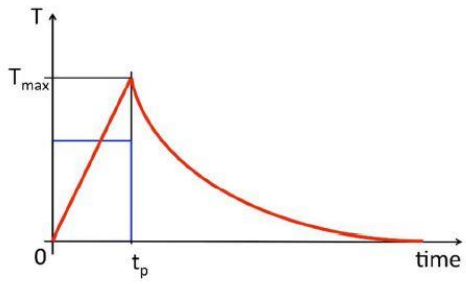

Figure 2.11 Representation of the evolution of the sample temperature upon irradiation by a single laser pulse under the assumption that the heat diffusion time of the sample is longer than laser pulse duration, showing an initial linearly increase followed by an exponential decay with a rate that is dependent on the thermal properties of the sample [10].

Increasing the temperature of the sample causes internal stress, which results in thermal expansion of the irradiated regions of the material. In the special case of a sphere (heat diffusion ~ $1.27*10^{-4}$ m^2/s) in a homogeneous and isotropic medium, we can describe the relative expansion a of the sphere as

$$da(t) = \frac{1}{3}\, a\, \alpha_T\, \Delta T(t) \qquad (9)$$

where α_T is the thermal expansion coefficient of the sphere.

By extension, as the temperature increase is related to the absorbed power (ΔP_{abs}), which is proportional to $\frac{K}{\lambda}$, the thermal expansion of the sphere should be related to the optical absorption coefficient. In other words, by measuring the thermal expansion as a function of wavenumber, the variation of the maximum thermal expansion as a function of wavelength should represent the absorption spectrum of the material probed.

2.4.2. Cantilever response to the thermal expansion

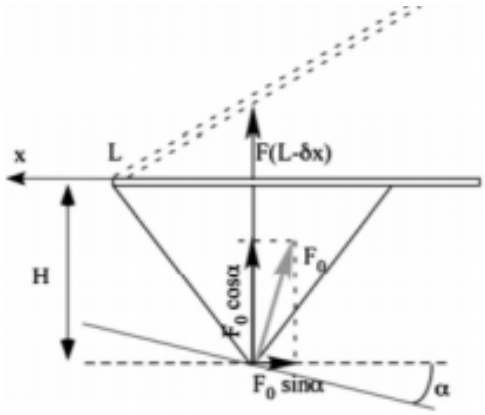

Figure 2.12 a) AFM cantilever schematic. The lever length is L and it is embedded at x=0. The tip is located at x=L-δx. The contact stiffness is represented by two springs, one for vertical displacement and the other for lateral interactions, b) normal and lateral forces exerted to the tip due to photothermal expansion of the sample [10].

The AFM cantilever is commonly modeled by the beam of length L. Its motion can be described using Euler-Bernoulli equation:

$$E\ l\ \frac{\partial^4 z}{\partial x^4} + \rho A\ \frac{\partial^2 z}{\partial t^2} + \gamma\ \frac{\partial\ z}{\partial t} = W(x,t) \qquad (10)$$

where E is the Young modulus of the cantilever beam, I is its area moment of inertia, ρ is the density, A is the cross section of the cantilever beam, γ as the damping of the beam and W represents the variation in the force exerted on the tip as the sample absorbs IR and expands. As shown in Figure 2.12. we set the x coordinate describes the longitudinal direction and z describes the deflection of cantilever. The cantilever is considered to be fixed at x=0 and the tip positioned at x=L-δx. is in contact with sample.

The general solution for the Euler-Bernoulli equation is expressed as a mode expansion [10, 62]:

$$z(x,t) = \sum_n P_n\ g_n(x)\ h(t) \qquad (11)$$

with P_n the amplitude of mode n of cantilever, $g_n(x)$ the spatial distribution of mode n and h(t) is the cantilever temporal behavior. The amplitude coefficient of the mode n, P_n, can be determined using the boundary conditions. The mode shape, g_n depends on the wave vector deduced from eigenvalue equation and can be calculated by different approaches such as analytically or finite elements.

$g_n(x)$ are the spatial eigenfunctions determined from the analysis of the clamped beam in free vibration as [10, 62]:

$$g_n(x) = \frac{Sin(\lambda_n L) - Sinh(\lambda_n L)}{Cos(\lambda_n L) - Cosh(\lambda_n L)}[Sin(\lambda_n x) - Sinh(\lambda_n x)] + [Cos(\lambda_n x) - Cosh(\lambda_n x)] \qquad (20)$$

where λ_n is the wavenumber and depends on the contact resonant frequency [45].

The force F(t) on the cantilever is often described as [10]:

$$F(t) = k_z\, u(t) \qquad (12)$$

where u(t) is the displacement of the cantilever tip, and k_z is the cantilever spring constant, calculated based on the Young modulus of the tip and the sample.

Considering the special case of the sphere mentioned above, the force on the cantilever due to the photothermal expansion of the sphere [62] can be described as:

$$F(t) = k_z \frac{a}{3} \alpha_T \Delta T(t) \qquad (13)$$

Finally z(x, t), the general solution for the Euler-Bernoulli equation, is expressed by combining the mode expansion in presence of the source term. Fourier transform can be used to isolate the temporal and spatial behaviors of the cantilever [62], in such a way that:

$$z(x,t) = \sum_n \frac{P_n}{\omega_n}\, g_n(x)\; Sin(\omega_n t)\, e^{-\frac{\gamma t}{2}} * T_{sph}(t) \qquad (14)$$

Initially, with IR OPO lasers, the energy deliver to the sample for each pulse was on the order of 50 μJ. If we consider the wavelength of light λ = 5 μm and a spherical sample of radius 100 nm with real component of refractive index $Re\left(\tilde{n}\,(\lambda)\right) = 1.7$ and the imaginary part $Im\,(\tilde{n}\,(\lambda))$ = 0.01, then the absorbed power is calculated as $P_{abs} = \frac{2\pi c}{\lambda}\, \varepsilon_0\, \frac{9\, n\, .K}{[n^{\,2}+2]^2} |E_{inc}|^2\, V = 4 \times 10^{-7}$ W.

The temperature increase corresponding to this situation is g about 4K for a density of ρ =1000

kg/ m^3, and specific heat capacity C_p=1500 J/K. By substituting $da(t) = \frac{1}{3}\, a\, \alpha_T\, \Delta T(t)$, where the thermal expansion coefficient is $\alpha_t = 1 \times 10^{-4}\, K^{-1}$, we find a thermal expansion smaller than a nanometer, making it difficult to detect it with an AFM probe in contact with sample. However, the force impulse is such that, even with the OPO pulsed at 1 kHz, well below the resonance of the cantilever, the eigenmode of the cantilever can be excited. The initial excitation corresponds to the "ringing" of the cantilever. The cantilever oscillation decay is dependent on the conditions of the measurement.

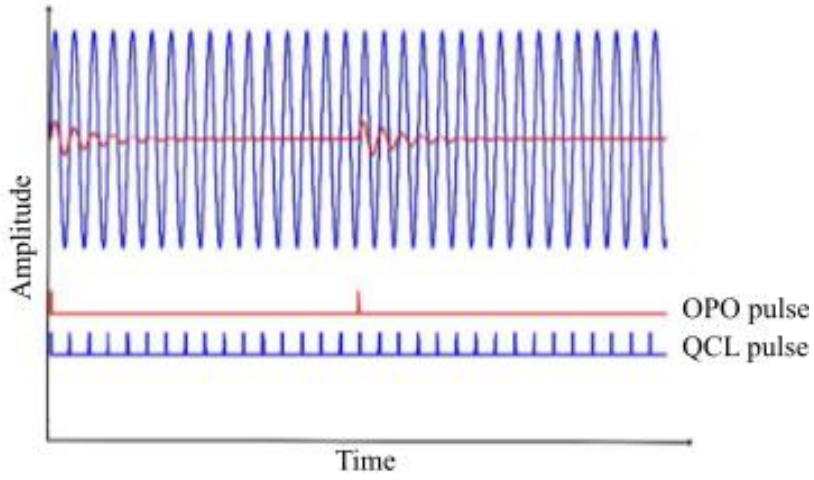

Figure 2.13 AFM deflection signal of the cantilever oscillation (top) as a function of the type of the laser pulse (bottom)-red is OPO which is the low repetition rate pulsed laser about 1kHz, and blue is QCL pulses which is high repetition rate pulsed laser 300 kHz. The cantilever oscillation due to OPO pulsed laser excitation is damped after each pulse, while the cantilever oscillation due to QCL pulsed excitation is continuous without damping [10].

Due to the low frequency of the pulse with respect to the cantilever resonance, the measurements using the OPO were found to be quite slow, and the signal-to-noise ratio to limit the sensitivity of the measurement. Advances in laser technology have made it possible to excite the sample more efficiently. Infrared quantum cascade laser (QCL) offer higher repetition rate (up to 1 MHz). Hence, it was found that the QCL laser pulse could be tuned to one of the contact resonance frequencies of the cantilever to create a system resembling a force oscillator. At the cantilever resonance the signal-to-noise ratio of the cantilever is highly improved, and so is the sensitivity of the measurement. Figure 2.13 demonstrates the AFM cantilever deflection signal for different laser sources, OPO (shown in red) and QCL (shown in blue) laser. In the two cases, the responses of cantilever z (x,t) are proportional to the absorbance.

In the case of QCL, τ_{relax} and the repetition rate of the laser are such that the excitation can be considered a forced oscillation. The expression of z(x,t) in the case of the QCL laser excitation becomes [10, 62]:

$$z(x,t) = \sum_n \frac{K\,\delta x}{\rho\,A\,L} B\; g_n(x)\; \left(\frac{\partial g_n(x)}{\partial x}\;|_{x=L}\right)^2 T_{max}\; \left(\frac{(t_p/2+\tau_{relax})}{\omega_n}\right) Sin(\omega_n t)\; \frac{Q_n}{2\pi} \quad (15)$$

$$z(x,t) \sim \sum_n \frac{P_n}{\omega_n}\; g_n(x)\; Sin(\omega_n t)\; * T_{sph}(t) \quad (16)$$

where Q_n is the quality factor related to the mode n [10, 62].

The result indicates that the oscillation is no longer damped in the configuration with AFM-IR is actuated with the QCL laser with laser pulse matching the cantilever contact resonance.

In next chapters, the AFM-IR is applied for characterization of plasmonic structures and biological samples with QCL laser as a source of IR radiation.

CHAPTER 3 CHIRALITY AT NANOSCALE

3.1 Introduction

Chiral structures are ubiquitous in our universe, with dimensions spanning from 200,000 light years in spiral galaxies, to a few centimeters in sea shells, to nanometers in human DNA: chirality divides our world into two parts, right and left-handedness [63]. The word chirality finds its origin in the Greek word "χειρ" - meaning "hand". Indeed, our hand is a chiral object: our right and left hands are the mirror image of each other, identical but not superimposable – *the right and left hands a*re *chiral with different handedness*. More generally, a structure is chiral is asymmetric and cannot be superimposed to its mirror image. A chiral molecule contains a chiral center. The most common chiral center is Carbon due ability to bind four different functional groups. Carbon is not the only atom that can act as a chiral center. Nitrogen, phosphorus, and sulfur can sometimes produce chiral molecules such as with methaqualone, cyclophosphamide and omeprazole respectively [64]. Due to the role Carbon plays in Nature, a plethora of biomolecules and living-organism building blocks are chiral, including amino acids, sugar, or proteins. Specific properties and functionalities often accompany chirality [65].

3.1.1 Chiral biomolecule overview

In chemistry, two chiral molecules with different handedness are called enantiomers, labeled S (or L) and R (or D) for left- and right-handedness, respectively. Enantiomers are defined by their

spatial arrangement of their substituents (chemical groups) around the chiral center. The handedness (spatial configuration) of the enantiomers is determined by the Cahn-Ingold-Prelog convention, which orders the chemical groups attached to the carbon based on their molecular weight [64] . As a simple example, Figure 3.1 shows the handedness of two enantiomers counting from highest priority (highest atomic number or highest mass) to the lowest one, from Br (atomic number:35)-> Cl (atomic number :17)-> F (atomic number :9). If the counting goes in the clockwise direction, the configuration is right-handed, and if it goes in counter-clockwise then the configuration of molecule is left-handed [64].

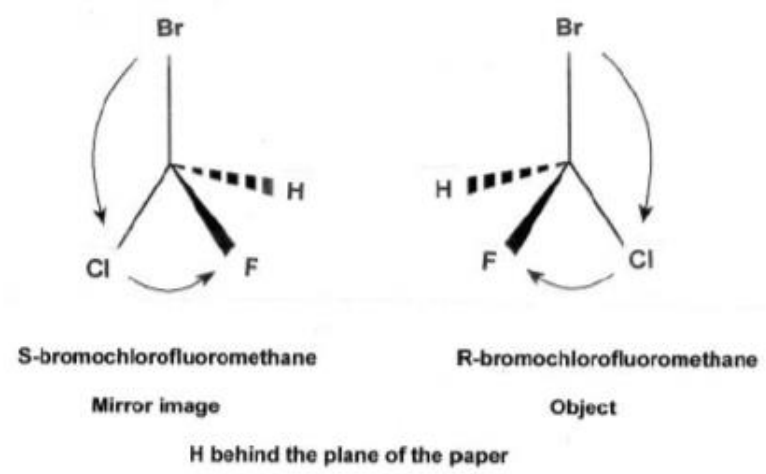

Figure 3.1 Example of handedness determination in a chiral molecule, with S-bromochlorofluoromethane, and R-bromochlorofluoromethane [64].

Enantiomers have the same physical properties including molecular weight, density, vibrational, and electronic transition frequencies. However, they can exhibit significantly different functions. For example, S and R enantiomers of limonene can be very difficult to distinguish with analytical

methods, but their smell varies considerably as S-limonene is found in lemon and R-limonene is found in oranges [66].

Beside the smell in fruits, molecular chirality can have substantially dangerous effects, as in the case of a drug called thalidomide [67]. In 1957, thalidomide was commercialized in 47 countries worldwide as a painkiller medication for pregnant women. Both enantiomers were contained in the formulations synthesized. Thousands of children with shortened limbs or without limbs were born because of this treatment. After the tragedy, it was found that although one enantiomer has a positive effect of pain and nausea, the other could fix itself onto the DNA of a growing fetus and inhibit the development of arms and legs. A number of other examples have been reported in medicine, as with ethambutol for which one enantiomer fights tuberculosis while the other causes blindness [67]. In methamphetamine, one enantiomer is used as a nasal decongestant while the other is a psychostimulant known as crystal meth [67]. Half of the drugs currently in use are chiral compounds and about 90% of these chiral drugs are in racemic mixtures, meaning a mixture of two enantiomers [68]. Although the enantiomers have the same chemical structure, they exhibit different biological activities which are important to distinguish in pharmacology, and toxicology. Most racemic drugs have at least one bioactive enantiomer. The other enantiomer can exhibit various level of a bioactivity [69]. Methadone is a racemic drug, which has been administered for treating opiate dependence and cancer pain. R-methadone is about 25-50 fold more potent than S-methadone as an analgesic, because S-methadone is metabolized and cleared by our body rapidly [70, 71]. In other racemic drugs, the two enantiomers are bioactive. However, one enantiomer may produce the desired therapeutic activities, while the other may be toxic [64] or lead to undesired effects [72]. For example, Dopa is a precursor of dopamine that is used for the treatment of

Parkinson disease. It was initially used in its racemic form, but had to be reformulated to L-dopa due to the toxicity of the D-enantiomer, which causes agranulocytosis (the condition of lack of one major types of infection-fighting white blood cells) [64]. Another example is propranolol. S-propranolol is a β-blocker medication, which controls abnormal heart rhythm and is used to treat hypertension. The side effects introduced by the presence of R- propranolol include reduction of the plasma concentration of triiodothyronine (T_3), which is only needed for patients suffering from hyperthyroidism [72]. Lastly, in some racemic drugs the "inactive" enantiomer can be transformed into a bioactive one under physiological conditions. Ibuprofen, which has an anti-inflammatory effect, is such a system [73]. S-ibuprofen is more potent than R-ibuprofen. Under *in vivo* conditions, the R- enantiomer is transformed into the S-enantiomer by hepatic enzymes [73, 74]. In summary, there are enormous pharmacodynamic differences between enantiomers. Due to the potential toxicity or side effects of racemic mixtures, the ability to detect trace amounts of chiral molecules, and selectively study their interactions and effects on cells, tissues, or other biological entities is highly desired. As a result, the US Food and Drug Administration (FDA) has issued guidelines for studying the development of enantiomers, including the need for their characterization and identification [75]. Currently, FDA requires manufacturers to identify the composition of enantiomeric products, the quality and purity of the chiral drugs in the market [75]. However, there are still challenges associated with detecting small amounts of molecules or impurities in formulations.

Next, we will review some of the state-of-the-art approach in studying chiral systems. Methods such as nuclear magnetic resonance spectroscopy (NMR) [76-78] and biosensors such as enantioselective immunosensors [79, 80] are often reported to study pure enantiomers or

enantiomeric solutions. In NMR, a magnetic field is applied to the system and exerts a torque on a magnetic dipole, which results in displacement of energy levels (uniformly spaced multiple splitting of the spectral lines). Because enantiomers have the same chemical and physical properties, they exhibit the same NMR spectra. Therefore, a special sample preparation is required to differentiate the handedness of a chiral molecule. Chiral substances of known handedness, called chiral alignment medium, can be used to create an environment in which the orientation of each enantiomer is different. For enantioselective detection of a racemic compound, different chiral alignment media are used. The limitations of NMR include the limitation of media with low alignment for some molecules, the high cost and the tedious process for data collection and analysis [77, 78].

Biosensors have also been reported for enantioselective characterization. For instance, enantioselective immunosensors can recognize the chirality of an antigen (enantiomer). In this design, the detection takes place based on an antibody-antigen preferential binding, similar to a key-lock mechanism. By designing a sensor sensitive to a functional group arrangement with selected handedness, it becomes possible to identify the presence of targeted enantiomers [80]. In an electrochemical immunosensor, the binding of the antigen to antibody results in a change in impedance on the electrode. Chen et al developed an electrochemical immunoassay to recognize the chirality of proline, using a carcinoembryonic antibody (anti-CEA) [79]. First, the proline enantiomers were coated on a glassy carbon electrode by immersion in 10 mM of D or L solution, followed by loading anti-CEA on the proline enantiomers. The experimental results demonstrate that the D enantiomers had a better recognition of anti-CEA than L for concentrations of anti-CEA between 0.17 ng/mL to 80 ng/mL [79]. Unfortunately, in cases of poor electrochemical

activity of the antigen and antibody, this technique would not be viable. In addition, false positive or lack of sensitivity may occur with this approach [79, 81].

On the other hand, single molecule detection techniques remain difficult to adapt to explore the chirality of individual molecules. Beyond the detection of impurities in drug formulations, single molecule studies would make it possible to explore fundamental questions regarding the role chirality play in Nature, particularly to unveil the heterogeneities at the molecular level contributing to average signals/properties measured at the micro- and macro-scale [82]. Among those single molecule techniques, we briefly discuss total internal reflection fluorescence (TIRF) microscopy and the near field scanning optical microscopy (NSOM) here [83].

TIRF microscopy has been designed to circumvent the background fluorescence of most conventional fluorescence techniques, by generating an evanescent wave at the crystal- sample medium interface. The excitation laser is totally internally reflected but the resulting evanescent wave can excite the fluorescent tags in the sample, limiting the region probed is limited to 100-200 nm above the surface. This configuration has been shown to be very sensitive for low concentration measurements [82]. However, it has not been explored for chiral spectroscopy.

NSOM is another method that aims as carrying out measurements for single or few molecules under light excitation. In NSOM, the laser light can be confined at the tip of the probe, far beyond the limit fixed by diffraction limit. The light confinement and E field enhancement has been achieved with both aperture and aperture-less probes configurations. For instance, single mode optical fibers coated with a thin film of Al can be used as a waveguide for the light with tiny aperture (70 nm). The fiber can be held very close from the sample surface (about 5 nm). The information collected is confined in the vicinity of the tip in contact with the sample.

Unfortunately, fiber tips are very brittle and subject to breakage and contamination. Due to the requirements of proximity to the metal coating on the tip to obtain an enhancement, this method is not suitable to explore features hidden in large systems such as cells. Further the small size of aperture limits the amount of light and hinders the detection of single molecule or minute amount of molecules [83].

In the present work, we propose a technique to characterize the chirality of enantiomers at the nanoscale by introducing a hybrid opto-mechanical method of detection to study chiral molecules, even in small quantities. We demonstrate that the chirality of a molecule can be determined using our proposed technique. Using considerations from circular dichroism (CD), an absorption spectroscopy technique quantifying the differential absorption of left and right circularly polarized light, we show that it is possible to enhance the detection sensitivity and spatial resolution of molecular handedness. In the next section, we discuss the general principle of CD spectroscopy.

3.1.2 Circular dichroism (CD) spectroscopy

In the nineteenth century, Fresnel and Biot introduced the concept of circular dichroism (CD) to differentiate two enantiomers [66]. Circularly polarized light can be used to probe the handedness of a molecule or system. CD spectroscopy is commonly defined as the difference in the absorption between the right and the left-handed circularly polarized light by an optically active material:

$$\text{Circular dichroism} = \Delta A(\lambda) = A(\lambda)\text{LCP} - A(\lambda)\text{RCP},$$

Where λ is the wavelength, $\Delta A(\lambda)$ is the difference between the absorption $A(\lambda)$ of left circularly polarized (LCP) light and the absorption $A(\lambda)$ of right circularly polarized (RCP) light. It has been demonstrated that, as in chiral materials, speed of light as well as real and imaginary parts of the

dielectric constants depend on the polarization handedness (LCP or RCP) and propagation [84]. CD spectroscopy has since been implemented in different regimes from ultraviolet [85] to infrared [86] to study the secondary structure of proteins and macromolecules, electronic transitions, as well as the geometric and electronic structure of optically active material [66].

In a CD spectrometer, when light passes through an optically active material, the right-handed and left-handed circularly polarized light moves into the material with different speed $c_L \neq c_R$. These two circularly polarized lights are absorbed to a different extent. To explain the circular dichroism in a standard way, we refer to the Beer-Lambert-Bouguer law. If the initial intensity of the light passing through the sample is I_0 and its intensity when it is leaving sample is I, the absorbance is defined as:

$$A = log \frac{I_0}{I} = \varepsilon\, c\, l \qquad (17)$$

where c is concentration (in mole per liter), l is pathlength (in centimeter), and ε is molar absorption coefficient. If right-handed and left-handed circularly polarized light pass through an optically active material, then the absorbance of each of these two polarizations are $A_{RCP} = log \frac{I_0}{I_{RCP}}$, $A_{LCP} = log \frac{I_0}{I_{LCP}}$ respectively. Commonly, any CD spectrometer passes the left-handed and right-handed polarization periodically through the sample, and records ΔA:

$$\Delta A = A_L - A_R = log \frac{I_0}{I_L} - log \frac{I_0}{I_R} = log \frac{I_R}{I_L} \qquad (18)$$

$$\Delta A = \Delta\varepsilon\, c\, l \qquad (19)$$

Circular dichroism can be also measured in terms of ellipticity. The shape of the ellipse is defined by the angle $\theta = tan^{-1}(\frac{b}{a})$, where b and a are the minor and major axes of the ellipse, respectively (Figure 3.2.c).

Linear polarized light can be transformed into elliptically polarized light after passing through an optically active material. We can consider that linearly polarized light is made up of two circularly polarized light components with equal magnitude, one component rotating clockwise (right-handed, R) and the other rotating counter-clockwise (left-handed, L), as shown in Figure 3.2 a. Circular dichroism (CD) indicates the differential absorption of these two circularly polarized components. After linear polarized light passes through a sample, the left-handed and right-handed components are examined. If the left-handed and right-handed components are not absorbed or if they are absorbed equally, the subsequent recombination will be transmitting linear polarized light (Figure 3.2.a). However, if left-handed and right-handed components are absorbed differently, the recombination of the transmitted (or reflected) waves will result in elliptical polarization, as shown in Figure 3.2 b. Thus, the linearly polarized light can be manipulated to become elliptically or circularly polarized.

CD instruments (spectropolarimeters) often measure ellipticity (θ) in degrees. In this method there is relation between ΔA and ellipticity $\theta = 32.98\,\Delta A$.

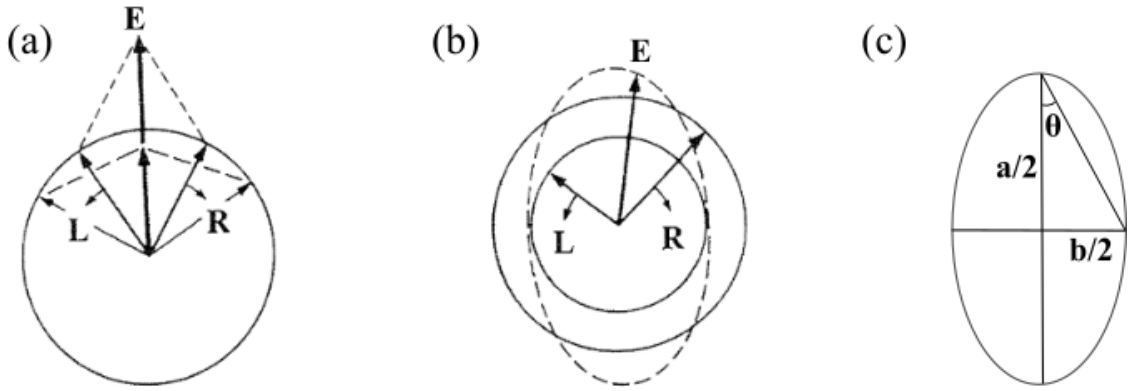

Figure 3.2 Polarization of light. (a) Linearly polarized light separated into left and right-handed components with the same intensity and phase, the two components have the same amplitude and produce linearly polarized light as they combine, (b) When a less intense left circularly polarized component combines with a more intense right circularly polarized component, the resulting electric vector of the electromagnetic wave follows an elliptical path , i.e. elliptically polarized light, (c) The semi-major and semi-minor axes of the ellipse make a triangle with an angle θ, referred to as ellipticity, circular dichroism can be measured [87]

CD can be measured by:

Modulation: the polarization is switched continuously between left-handed and right-handed circular polarization. Circular dichroism is measured as a function of wavelength to identify the signature of a molecule. In a CD spectrometer, the linear polarized light passes through a modulator which is connected to the alternating electric field. The modulator is composed of a piezoelectric quartz crystal and an isotropic plate which is tightly coupled to the crystal. The

alternating electric field makes changes in structure of quartz crystal, which results in transmit the circularly polarized light. The transmitted radiation is switched between left and right handed components [87],

Direct subtraction: The absorbance of the right-handed and left-handed polarized light are measured individually and then subtracted from each other.

Ellipsometry: The ellipticity of the transmitted light is measured.

3.1.3 CD spectroscopy limitation

Although advances in CD spectroscopy have enabled important findings in biology and chemistry, the approach is facing several drawbacks [88]. The CD signals of most biological studies are very weak. The ellipticities are usually in the range of 10 mdeg corresponding to the ΔA difference in absorbance in the order of 3×10^{-4} [87]. In order to meet the absorbance standard, either the concentration or the CD instrument cell pathlength or both should be adjusted. Molecular CD has low sensitivity and is restricted in terms of detectable molecular concentrations. For instance, the lower concentration limit for proteins is in the order if 0.1 $mg.mL^{-1}$ or 0.1 mM for single amino acids [89].

Studying the properties of single molecules is very challenging due to poor interaction strength. This can be explained, in part, by the small size of the molecules relative to the helical pitch of chiral light, which can only "twist" the circularly polarized light by an almost unnoticeable angle over the length of the molecule. This phenomenon is usually described using the dissymmetry factor "g": $g = 2\frac{\Gamma(RCP)-\Gamma(LCP)}{\Gamma(RCP)+\Gamma(LCP)}$, where Γ is the rate of excitation of the chiral molecule in RCP

and LCP light [90]. g is used to assess the interaction of circularly polarized light with a chiral molecule. For most small molecules, g is smaller than 10^{-3} in the visible wavelength range. Single molecules or small number of molecules cannot be readily studied with CD spectroscopy meaning that CD spectroscopy is not sufficiently sensitive to detect minute amount of molecules. As chiral responses of individual molecules are often too weak to be detectable by conventional approaches, a CD spectrum generally only represents the average response of the group of molecules occupying the volume probed by the excitation illumination (several micrometers in vibrational Circular Dichroism vCD). CD spectroscopy also faces limitations common to all optical techniques, which includes poor spatial resolution (diffraction limit which is about half of the wavelength of incident light). For other types of spectroscopy such as visible or infrared (non-polarized) spectroscopy, several near field approaches have been developed to obtain the chemical information at a much finer scale [91].

3.1.4 CD spectroscopy at nanoscale

Overcoming CD limitations with AFM and plasmonic structure

The properties of molecules adsorbed on or near structured metallic nanostructures or nanoparticles can be studied by taking advantage of a phenomenon known as plasmonic enhancement. Optical properties of metals over a wide range of frequency can be explained by the plasma model. The model considers a gas of free electrons in the metal, which organize in the material according to an applied electromagnetic field. At a given time, the positive and negative charges in the plasmonic structure separate upon polarization by the E field. Over time, is the E field is oscillating as is the case with light, the charges oscillate. The collective sustained

oscillation of the free electron gas is referred to as plasmons (or plasma oscillation). In spatially confined structures with dimensions smaller than the wavelength of the light, localized surface plasmon resonance (LSPR) can be excited as well. In a thin metallic layer which forms an interface with a dielectric medium, propagating surface plasmon resonance (pSPR) can be created at the interface [92]. This property of metallic nanostructure has been widely exploited for spectroscopy and sensing. The behavior is mostly exploited in the visible range, although work in the infrared range has also been reported as with surface enhanced infrared absorption (SEIRA) [93]. SEIRA was performed with substrates composed of gold nanoshell aggregates to enhance the vibrational modes of adsorbed adenine [94].

As CD spectroscopy suffers from poor sensitivity, studies exploiting the benefits of plasmonic enhancement for sensing have proposed designs to enhance the signal from CD for more sensitive detection of chiral molecules. In addition, the synthesis [63] and engineering of nanosystems [84] with carefully controlled chirality have been found to exhibit superior chiroptical properties [95] . In particular, optical activity larger than those found in nature and signatures with narrower CD bands have been reported for chiral quantum dots made of CdS or CdSe coupled with chiral ligands and for 3D chiral plasmonic metamaterial (oligomers) made of gold [96].

Planar plasmonic structures, both chiral and achiral, structures have also been considered to boost the limit of detection of chiral molecules. The CD response of chiral molecules can be enhanced [97] or can be used to excite the resonance of plasmonic nanostructures in their vicinity [98]. Many chiral molecules exhibit a CD signal in the ultraviolet to visible range. However, long exposure of the molecules to ultraviolet (30 min integration time in conventional

CD measurement) can affect the initial conditions of the biomolecules [99]. Some studies discuss how the chirality of the molecule in the UV cannot readily be detected but their coupling with the nanostructure can be detected [99]. This has reported for achiral gold nanoislands coupled with chiral molecules [100, 101]. As shown in Figure 3.3 b, from [101], after simple achiral gold nanoparticles that did not exhibit a CD signal were coated with riboflavin, a chiral molecule, a CD signal around 550 nm was measured. This band corresponds to the plasmon resonance of the structures. Based on the controls carried out in the study, the band observed at 550 nm can only be explained by the fact that riboflavin can induce a plasmonic CD induction in a near field mechanism. The induced plasmonic CD signal is due to the molecules placed in the vicinity of nanoparticles and it originates from plasmon-molecule Coulomb interaction mechanism. In this mechanism, dipole of chiral molecule induces chiral currents inside the plasmonic, which result in optical absorption and CD signal being generated. Figure 3.3 e presents the calculated CD spectra based on the simple dipolar interaction model considering a molecular dipole located from a surface of spherical plasmonic gold particle by distance d, where d is considered as 9.5 nm and with the particle radius of 23 nm, which is the radius average of the islands [101]. This theoretical result was found to be in good agreement with the experimental data. This approach illustrates that a chiral molecule does not have to be in resonance with the plasmonic nanoparticles to affect the behavior of the plasmons, as shown in Figure 3.3 c. However, as the overlap between the molecular absorption and the plasmon resonance increases, the enhancement and thus sensitivity of the sensor is expected to increase. The induced plasmonic CD signal is sensitive to small amounts of molecules but not single molecules. In the study a first set of results were reported to hold about 700 molecules per nanoparticle. The aim would be to reduce

this number to reveal the presence of chiral molecules in known or unknown samples [101]. We note that this technique will likely provide limited information regarding the detailed conformation of the probed molecule as the signal measured is a direct measurement of the CD of the molecule itself.

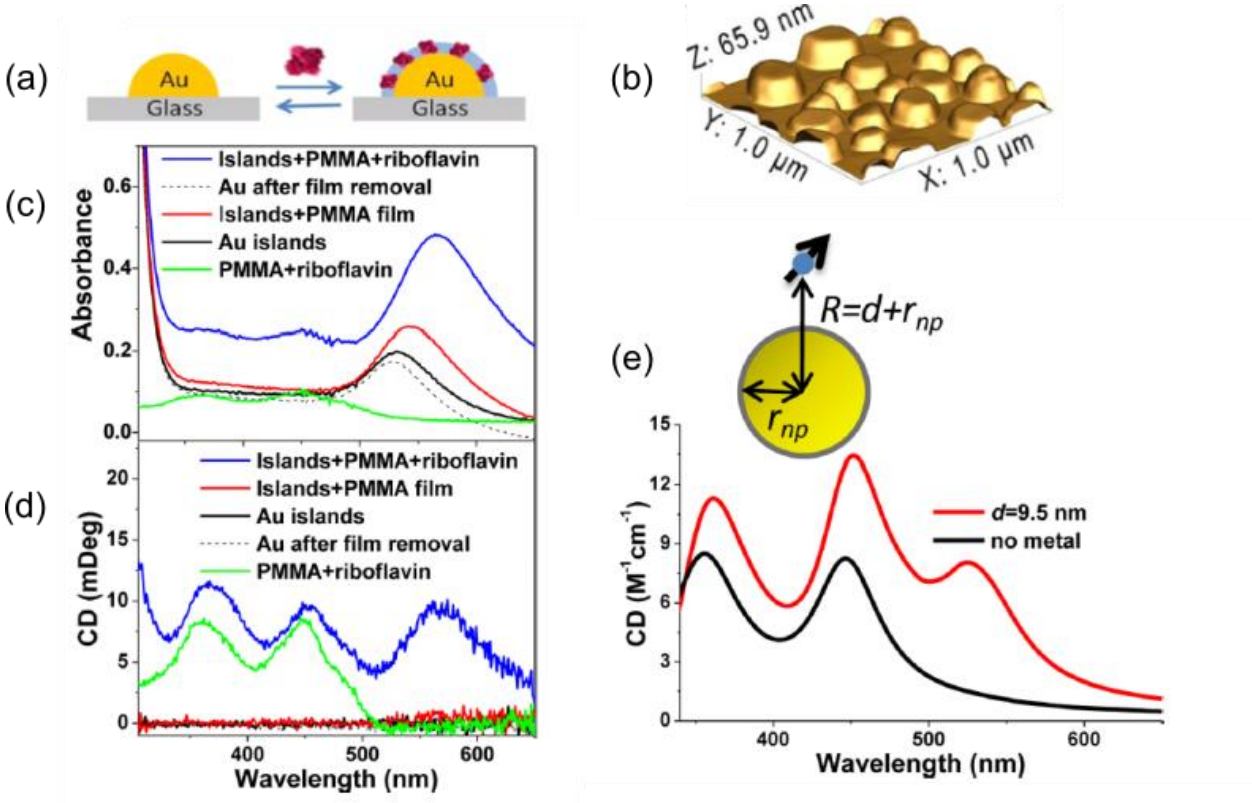

Figure 3.3 a) Schematic of a bare Au island and a coated Au island with riboflavin embedded in PMMA, b) AFM image of Au islands c) Absorption and d) CD spectra of bare Au islands, Au islands coated with PMMA, Au islands coated with PMMA and riboflavin, and PMMA with riboflavin without Au nano-islands. The absorption spectra of Au islands after the PMMA and

riboflavin were removed is also shown, e) Calculated CD spectra according to the dipolar model of interaction between chiral molecular dipole and spherical gold for riboflavin/PMMA only (black line) and riboflavin/PMMA near the spherical nanoparticle at distance of d=9.5 nm and radius of nanoparticle is 23 nm. From [101].

Twisted assemblies of metamaterials have also been considered for chiral molecule sensing. For instance, a stacking of two spaced achiral gold nanorods with a rotation between them ($+60°$ and $-60°$, as shown in Figure 3.4 a and b) was considered to enhance the CD signal of enantiopure molecules [99]. The two stacked nanorods were separated by a 80 nm dielectric layer. (S) and (R) propanediol enantiomers were probed in this study. First, (S) enantiomers were deposited on the structures and CD spectra were collected on the $+60°$ metasurface (blue solid circles in Figure 3.4 c) and $-60°$ (blue void circle in Figure 3.4 c). The same procedure was repeated to measure the CD signal of (R) enantiomer (Figure 3.4 d). The signatures were compared to a racemic mixture on both substrates for control. To remove the large background CD spectrum due to the metamaterial, the CD signals obtained with enantiomeric pair of plasmonic structures ($60°$ and $-60°$ substrates) holding the same analytes were added as shown in Figure 3.4 e. This response is related to the near-field interaction between the chiral molecules and the metasurface. It was estimated that this approach could detect about 55 zeptomoles of chiral analytes, which corresponds to about 44 molecules per unit cell of metamaterial structure [99].

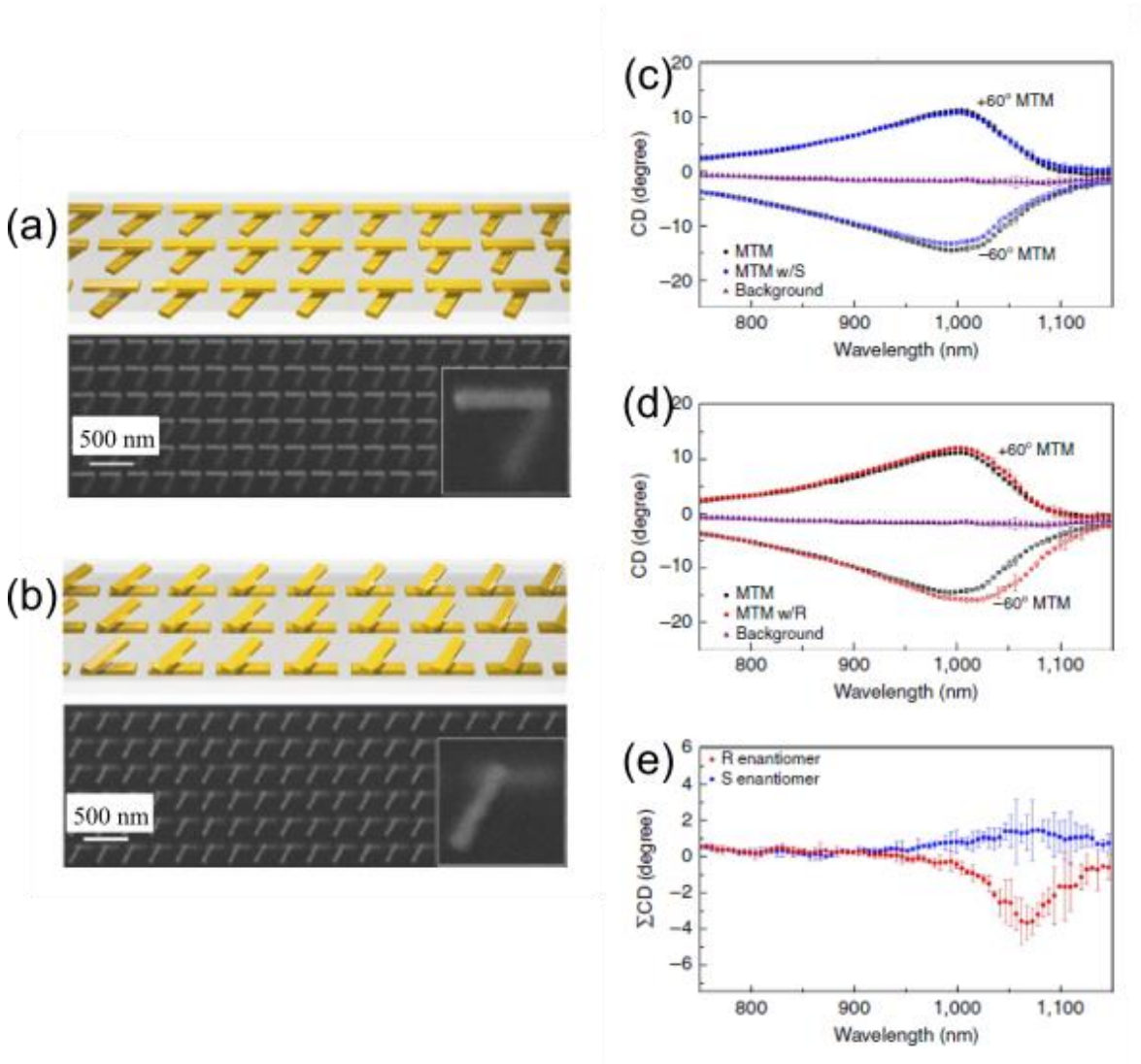

Figure 3.4 Scanning electron microscope image accompanied with illustration of the a) +60° and b)−60°metamaterial, c) Experimental measurement of (S)-1,2 Propanediol on the + 60 ° metamaterials (solid circles) and on the − 60 ° metamaterials (void circles). The black curves refer to ± 60 ° metamaterial with racemic mixture (1:1 ratio) , d) Experimental measurement of (R)-1,2 Propanediol on the + 60 ° metamaterials (solid circles) and on the − 60 ° metamaterials

(void circles). e) CD summation to remove the background of metamaterials, the curves show opposite signs for R and S enantiomers [99].

Chiral molecule detection has also been reported using chiral plasmonic structure [102]. Gold plasmonic metamaterial in the shape of gammadions were produced and reached a detection at the picogram level [102]. The CD spectra of right-handed and left-handed gammadions are shown in Figure 3.5.a. Three modes of bare gammadions were identified in the CD spectra. In presence of the chiral molecule, the modes exhibited a shift due to the changes in local environment of the plasmonic structures, as shown in Figure 3.5.b. In this work, the detection was mainly based on the shift of the CD modes. This can be hindered in cases of minute shifts for a low chirality molecule or a low concentration.

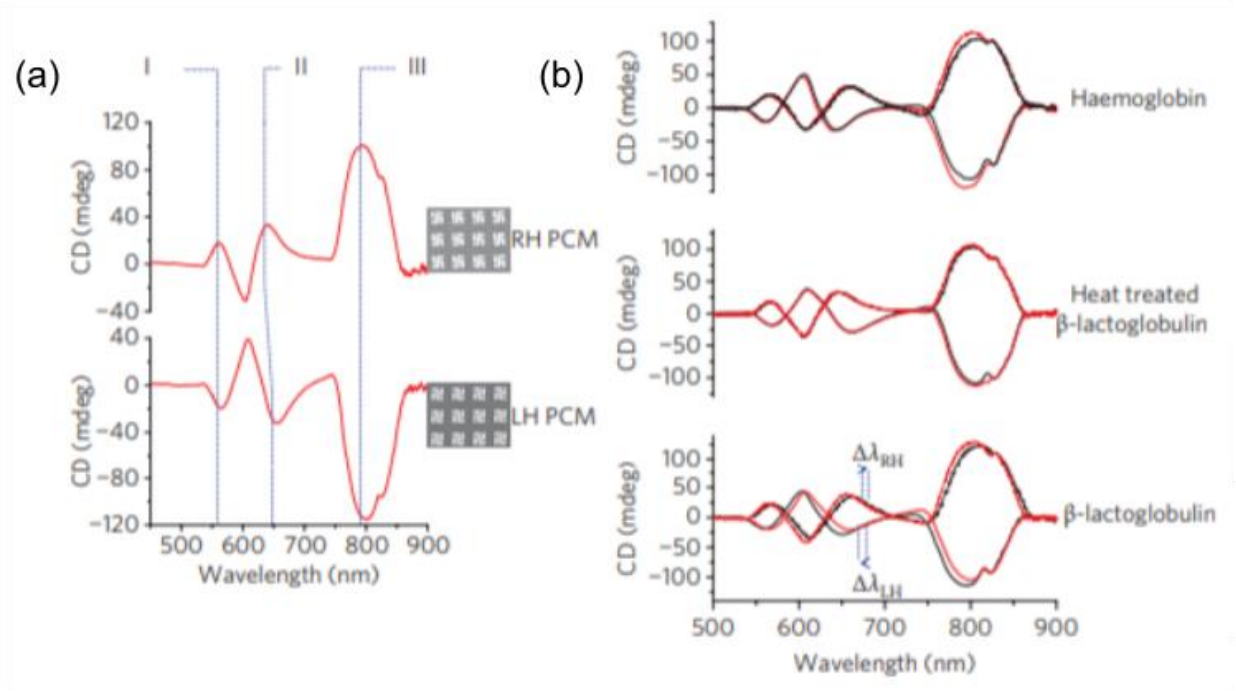

Figure 3.5 a) CD spectra of right handed (top) and left-handed gammadions (bottom) immersed in the distilled water, b) Influence of adsorbed proteins hemoglobin, β-lactoglobulin and thermally denatured β-lactoglobulin on the CD signal of gammadion plasmonic structures. Red spectra were collected before protein adsorption and black spectra were collected after protein adsorption[102].

To explain the mechanisms leading to the shift in the spectra, the local field enhancement of a left-handed gammadion illuminated with left-handed circularly polarized light is presented in Figure 3.6. The spatial distribution of the local density of chirality of an electromagnetic field is described by optical chirality (or chiral density) parameter C, which represents the helicity of light [97]:

$$C(r) = -\frac{1}{2}\,\varepsilon_0 \omega\, Im\,(E^*.B)$$

where E and B are electric and magnetic fields respectively, ε_0 is vacuum permittivity, and r is the position vector.

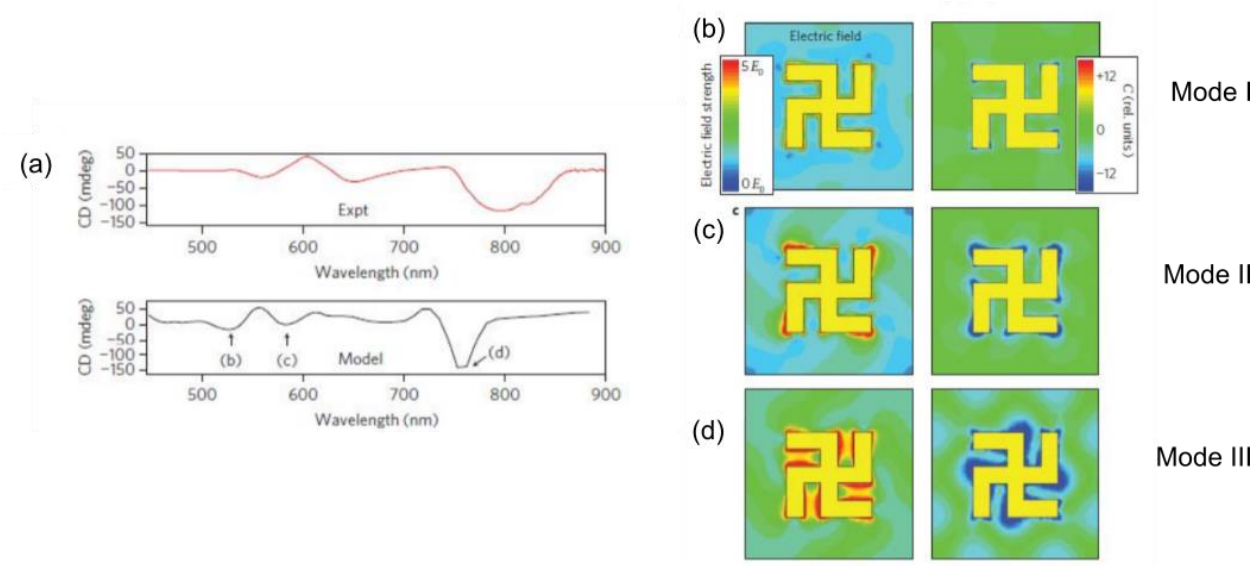

Figure 3.6 Finite element modeling of the local electromagnetic fields around the gammadion, a) Comparison between experimental and modeled CD spectra, b-d) Left panel: time averaged electric field strength calculated the three modes of the CD spectrum calculated at the substrate interface and normalized to the incident electric field. Right panel: optical chirality of near field normalized by the magnitudes of left handed circularly polarized light [102].

Optical chirality of superchiral field generated near metamaterial structures is one to two orders of magnitude larger than optical chirality of circularly polarized light [103]. The right hand panel of Figure 3.6 b demonstrates the optical chirality of near fields generated. The results suggest

that larger values of chirality of the electromagnetic field C will result in stronger light-molecule interactions and will be beneficial for chiral molecule detection.

Another factor considered in this line of work in the dissymmetry factor g. Vasquez et.al demonstrated that achiral cavity coupled hole-disks array can generate chiral near field and enhance the detection sensitivity of 0.6 M camphor (chiral molecules) about four orders of magnitude compared to conventional CD measurements [97]. This achiral plasmonic structure is shown in Figure 3.7. It is composed of nanostructured square array of gold hole disk with period of 740 nm, diameter of 480 nm, hole disk separation 350 nm, and film thickness of 30 nm coupled with a cavity, i.e. a gold back mirror which is separated from the plasmonic pattern by a dielectric spacer. The array was designed to have resonances in the infrared range at 2900 cm^{-1} (Figure 3.7 b). The calculations showed that the field enhancement could retain chirality at near field as shown in Figure 3.7 c. Next, a chiral molecule (camphor) with the same absorption wavelength as the array ($\sim 3000\ cm^{-1}$) was deposited on the substrate.

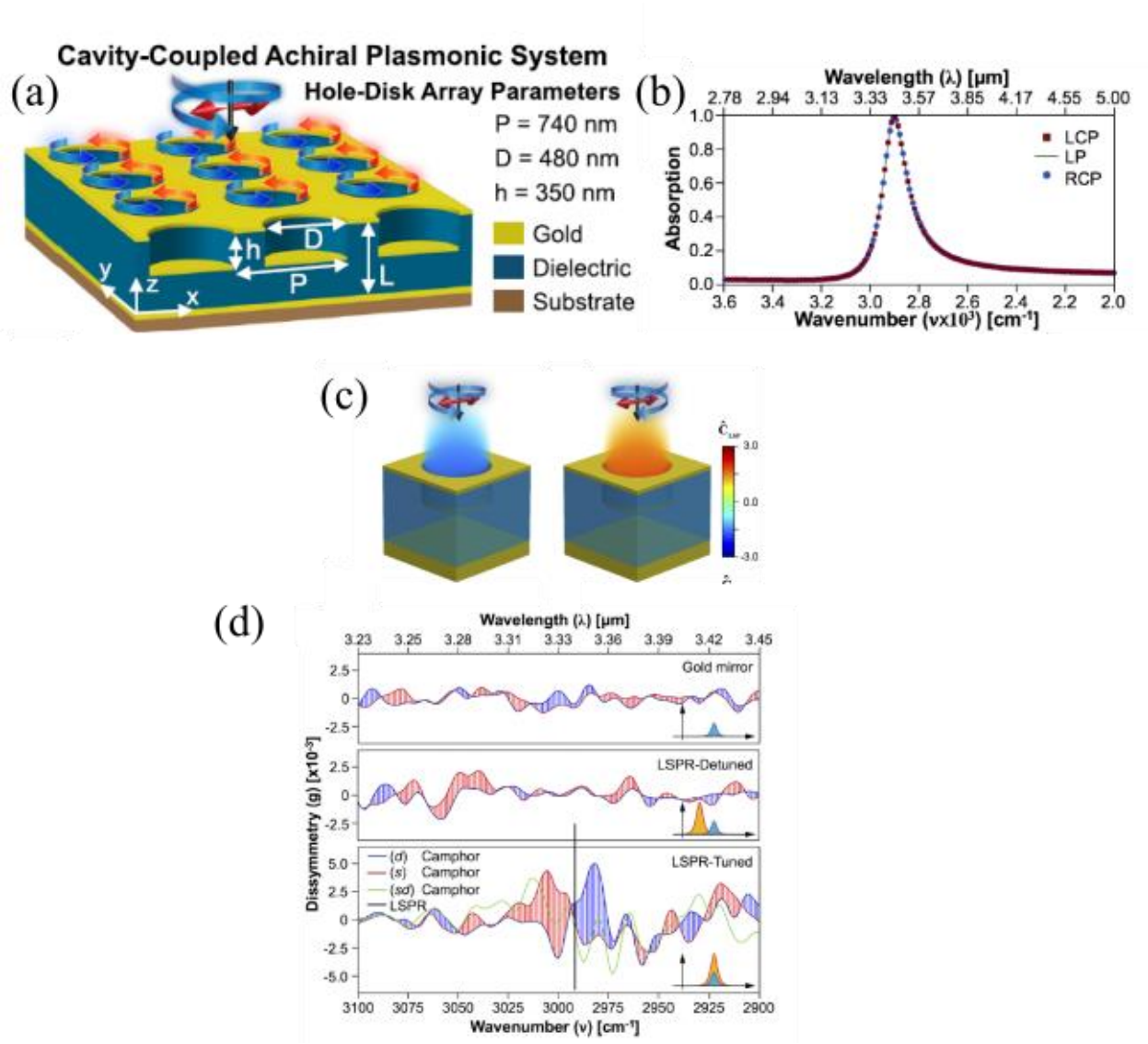

Figure 3.7 a) Achiral plasmonic system, cavity coupled hole disk array, b) Simulated absorption spectra for hole-disk array structure for LCP, RCP and linear polarized (LP) light, c) Free space normalized chiral near field distribution for LCP (left figure) and RCP (right figure) excitation demonstrated for one array unit cell. The chirality of near field is the same as the chirality of the irradiated light [97]. d) Dissymmetry for camphor on bare gold mirror, detuned and tuned achiral plasmonic substrate, the black vertical line shows the resonance of tuned substrate [97].

The dissymmetry g (or normalized CD) is measured using circularly polarized light using a far-field setup coupling FTIR to an optical microscope adapted for IR light. As shown in Figure 3.7d the dissymmetry for bare gold and hole-disk detuned substrates was around zero, while the tuned substrate enhanced the dissymmetry of 0.6 M of camphor about 4 orders of magnitude compared to conventional CD spectroscopy of the same concentration of camphor. This enhancement is due to the interaction of molecule with chiral near field [97]. Although the authors demonstrated that this technique can measure the vibrational CD (VCD) of the molecules, the diffraction limit would prevent from single or few molecule detection or from identification of contaminants (such as the presence of an undesired enantiomer) in heterogeneous samples.

Lateral resolutions below the inherent diffraction limit of light have been achieved for other types of optical microscopies and spectroscopies using near-field and scanning probe approaches [104] . Recently, Zhao et al. demonstrated a technique to measure enantioselective optical force using an AFM probe coupled with a plasmonic aperture (Figure 3.8 c) [99]. Optical force was shown to depend on the handedness of the illumination. The measurements also considered a chiral AFM probe, designed with focused ion beam (FIB) (Figure 3.8 b). The arrangement was found to enhance enantioselective optical forces and to control optical chirality. The optical forces measured with a commercial AFM tip under RCP and LCP illumination observed the same decay as a function of distance (Figure 3.9 b), whereas the same experiment with a chiral AFM tip (Figure 3.9 c) experienced different forces.

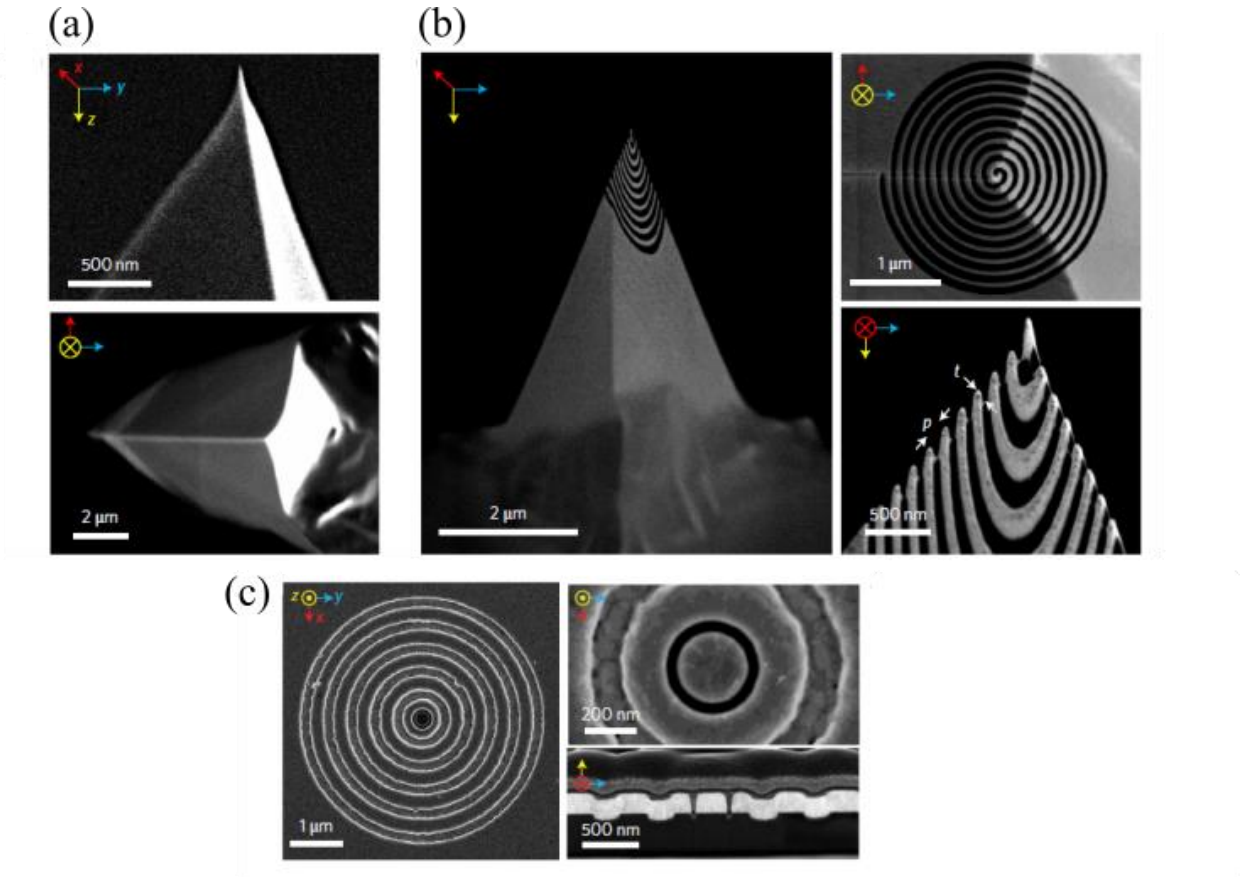

Figure 3.8 a) SEM image of achiral silicon tip, b) SEM image of chiral tip which is fabricated by focused ion beam milling, c) SEM image of coaxial nano-aperture [99]

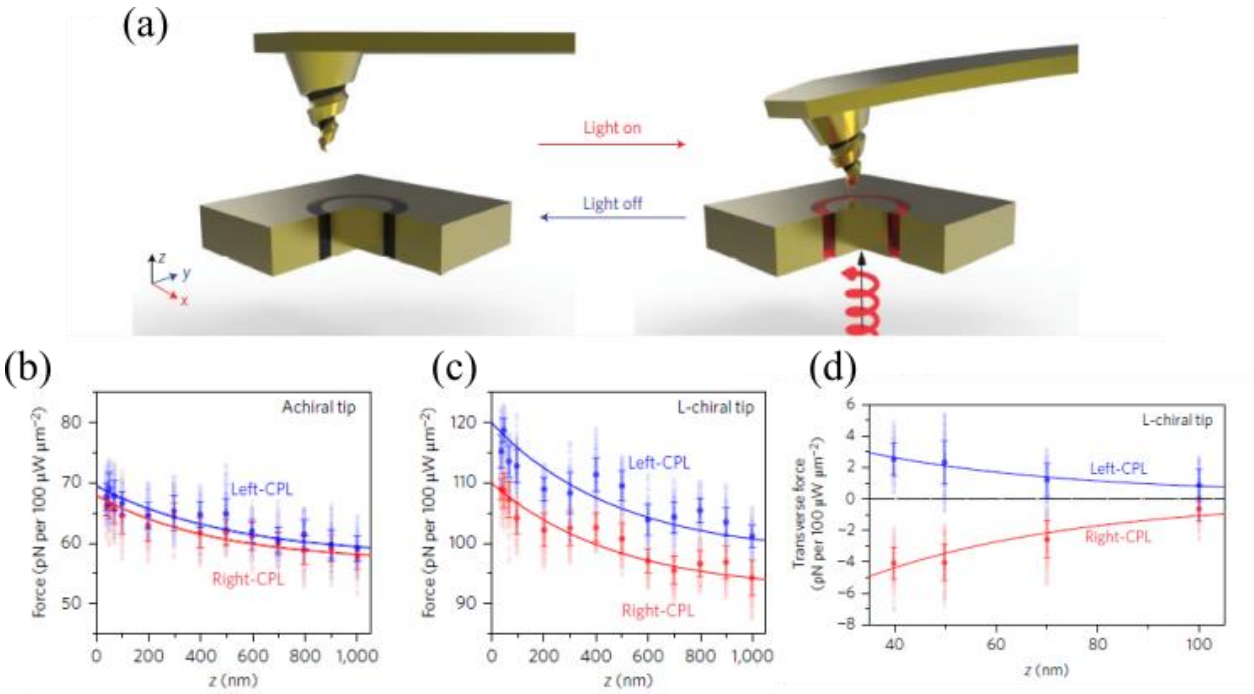

Figure 3.9 a) Schematic of enantioselective force mapping where circularly polarized light illuminates a coaxial nano-aperture which is made of gold. b) Optical forces by using an achiral tip with LCP (blue) and RCP (red) illumination, c) Optical force using the left-handed chiral tip with LCP (blue) and RCP (red) illumination, d) Transverse forces with left-handed chiral tip with LCP (blue) and RCP (red) illumination [99].

The forces observe results from circulating current is generated in the tip due to the chirality of the structure, thus inducing a magnetic dipole moment that interacts with the electric dipole moment. This additional force is proportional to the chirality of the structure. Transverse forces make it possible to visualize enantioselective optical forces [99].. This study paves the way to studying chiral material, for instance by functionalizing an achiral tip with a chiral molecule or chiral nanoparticle and measuring the optical force or by considering a substrate with a chiral near field.

A microcantilever with a sharp metallic tip can be used as a powerful nano-antenna for optical detection [105, 106] or as a sensitive nanomechanical sensor for detection of the local material photothermal expansion [10, 11, 53, 54, 62, 91, 107]. The latter is referred to as AFM-IR in this work. Such approaches have not yet been considered for CD spectroscopy.

Remaining opportunities

Based on the review of the state-of-the art work, we have designed a new approach to probe the vibrational CD signal of biomolecules, which we will present and evaluate in the following sections.

3.2 Experimental section

Here we present the first nanoscale CD spectroscopy approach exploiting the chiroptical properties of a planar metamaterial together with the nanoscale-resolved infrared spectroscopy performance of AFM-IR. We use a non-chiral array of gold microdisks combined with a gold reflector (mirror). We demonstrate that AFM-IR can be used to map the optical activity of the structures with oblique incident of circularly polarized light to produce maps representing the CD at selected wavelengths. The results are in good agreement with the computational modeling. The photothermal expansion of the structure was found to be dependent on the orientation of the structures in the plane with respect to the angle of incidence of light. Lastly, we measured the vibrational circular dichroism response of Poly-L-lysine using the plasmonic achiral metamaterial (cavity coupled microdisks) as a substrate. Photothermal expansion of the molecules indicates a thermal gradient near the regions of the microstructures with the high level of plasmonic confinement and chirality.

3.2.1 Fabrication and sample preparation

The fabrication was carried out by Abraham Vasquez in Dr. Chanda's group.

The microdisk arrays were fabricated using soft-lithography and lift-off techniques as shown in Figure 3.10. Two devices with different configurations were fabricated with the same microdisk array, one on plain glass substrate and the other on a gold and silicon dioxide stack. The process started with a clean glass substrate coated with 3 nm of titanium, 80 nm of gold, 3 nm of titanium and 100 nm of silicon dioxide using e-beam evaporation. Then, a diluted SU-8 2000.5 (Microchem Corp.) was spun coated at 3000 rpm followed by one min soft bake at 95ºC. The micropattern was thermally embossed using a polydimethylsiloxane (PDMS) stamp that contains the phase information (3 μm period and diameter from 1.98 to 2.57 μm) leaving an array of holes on the polymer film followed by one-minute UV (365 nm) exposure. Reactive ion etching removed the excess polymer on the holes leaving the substrate exposed. Finally, 3 nm of titanium and 30 nm of gold were e-beam evaporated followed by piranha lift-off (H_2SO_4:H_2O_2 in 3:1 ratio) to complete the process. Oxygen plasma cleaning was performed to remove polymer residues prior to characterization.

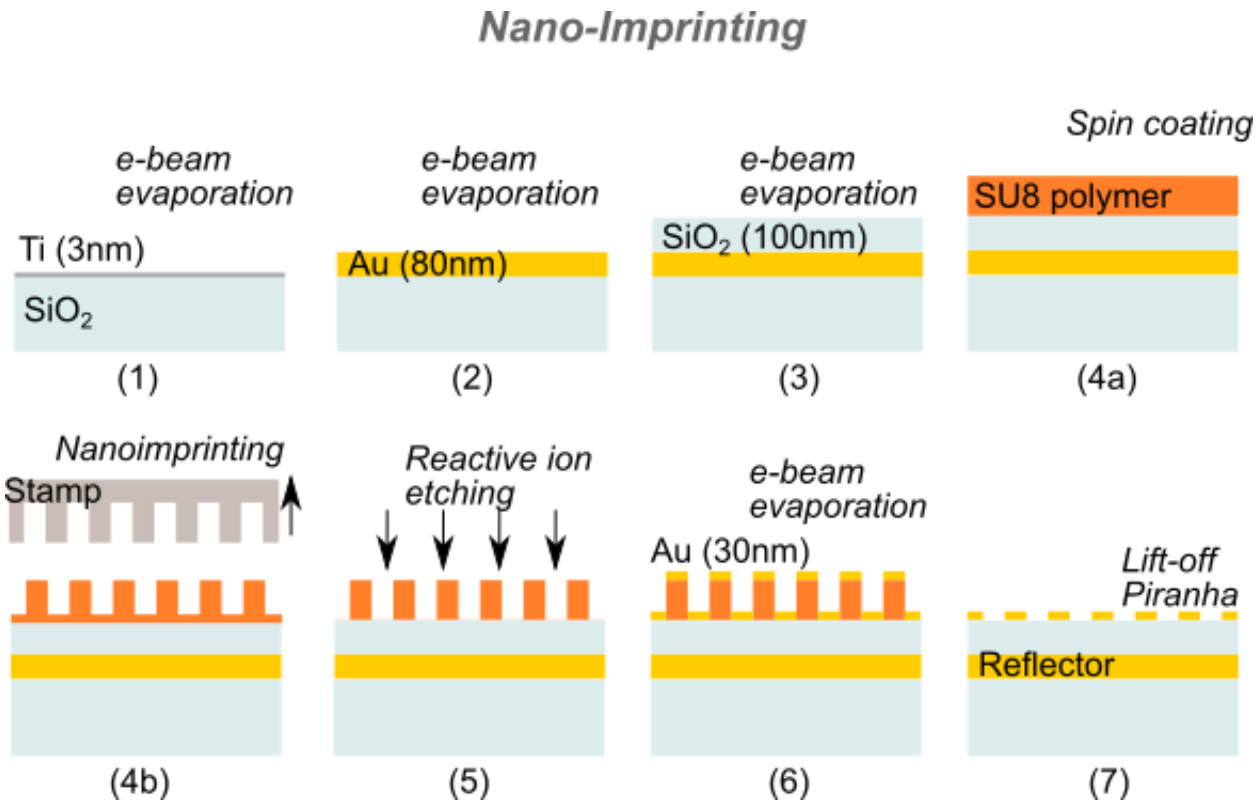

Figure 3.10 Nanoimprinting fabrication process. The following steps are undertaken to design the microdisks array on a clean glass slide: 1) 3 nm of titanium, 2) 80 nm of gold, 3) 100 nm of silicon dioxide, 4) Spin coat SU8 and thermally emboss the pattern, 5) reactive ion etching to remove the residue in the holes, 6) Deposit 30 nm of gold, and 7) Piranha lift-off

3.2.2 Plasmonic structures evaluation

The characterization was carried out in collaboration with Abraham Vasquez in Dr. Chanda's group.

Planar metamaterials, in particular arrays of microdisks were produced using traditional soft lithography, which is shown in the previous section. The design was first optimized theoretically using 3D finite differences in the time domain FDTD simulations Figure 3.11. represents the IR

absorption of the structures calculated for a design of gold (Au) microdisks with diameter ranging from 1.98 (blue) to 2.57 μm (red), constant thickness of 30 nm, and period of 3.4 μm, deposited on SiO_2 substrate. Once fabricated, the absorption of each array was measured with Fourier Transform Infrared (FTIR) spectroscopy Figure 3.11a. The experimental spectra were found to be in good agreement with the predictions. We note that FTIR measurements were carried out with incident light at 30º with respect to the normal to the sample surface to mimic the AFM-IR setup that will be used for the localized AFM-IR measurements. Experimentally, the band corresponding to the computational prediction was observed. A broadening of the bands is observed that is attributed to variations in thickness, diameter or shape of the disks across the region probed, compared to the modeled system where the motif is identical throughout. A second band around 1610 cm^{-1} can also be seen. This range corresponds to the aromatic vibration (C=C), which could potentially attributed to polymeric residues [108] , but the amplitude of the band suggests that this is not the main contribution, especially given that the AFM images did not indicate significant contamination. Previous studies on localized surface plasmon polaritons in metal/SiO2/metal Fabry–Pérot configurations, such as the one by Ye et al[109], discuss the presence of an asymmetric longitudinal optical (LO) phonon vibration mode of the SiO2 layer at 0.15 eV. In the case of a sufficiently thin SiO_2 layer, the LO mode was accompanied with additional modes at 0.12 eV and 0.19 eV resulting from the coupling of the surface plasmons in the direction of the interface induced at the top and bottom interfaces of SiO_2 with the metal. The coupling effect was found to form local surface plasmon polaritons (LSPP) underneath the metallic structures. The additional modes were thus assigned to the first LSPP mode (m=1) where each mode can be determined using the expression $2d = m \lambda/n_{eff}$, with d the thickness of

the cavity (100 nm), λ the wavelength at which the fringe is observed, and n_{eff} the effective index of refraction of SiO_2 (estimated at 1.23 at 0.19 eV). The band observed at 1610cm^{-1} (~ 0.19 eV) is thus most likely due to the SiO_2 coupling to the Fabry–Pérot Au-SiO_2-Au cavity. Based on the absorption band of the disk, we selected the Au microdisks with diameter 2.16 μm for maximum absorption in the range of illumination (1530-1810 cm^{-1}) of the infrared laser available on the AFM-IR system used hereafter Figure 3.11.c illustrates the nanoscale topography of the array of microdisks with diameter 2.16 μm, which will constitute our main substrate for the remainder of the manuscript. Unless specified otherwise, the measurements were carried out on Au microdisks fabricated on a Fabry-Perot cavity which is formed of SiO_2 substrate coupled with an Au reflector layer (Figure 3.11.c). The same array without the reflective layer was also produced and the comparison of the results is provided in Figure 3.18.

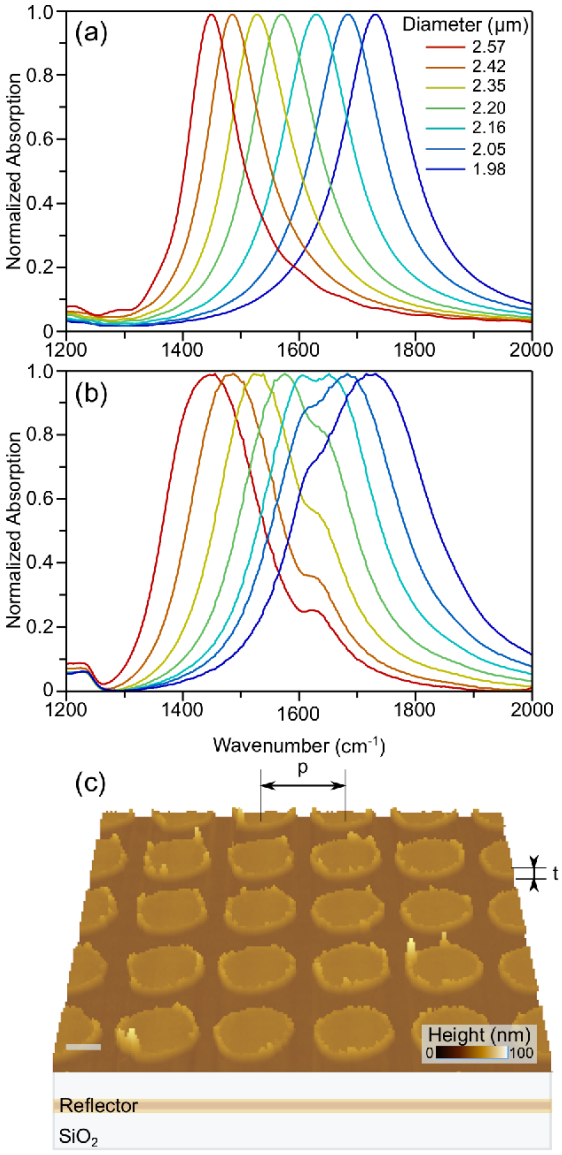

Figure 3.11(a) Theoretical far field absorption of arrays of Au microdisks with diameters varying from 1.95 μm to 2.57 μm. (b) FTIR absorption of corresponding arrays of Au microdisks with same diameters fabricated with soft lithography. (c) AFM topography of the array Au microdisks with diameter 2.16 μm, period p of 3.4 μm and thickness t of 30 nm for maximum absorption in the 1530-1810cm^{-1}, with a reflector layer designed beneath the metasurface in a SiO_2 substrate. Scale bar image is 1 μm.

The optical activity of the array was first evaluated with FTIR by measuring the difference in absorption of microdisks under RCP and LCP illumination. A cassegrain reflective objective was used to focus the light on the microarray, giving the incident light angle that was measured to about 20-30 degree from normal to the sample plane. The two spectra obtained are presented in Figure 3.12.a. The difference in absorption ΔA was calculated and the resulting CD spectrum is shown in Figure 3.12.b. Given the profile of ΔA for the selected array in the 1550-1800cm^{-1} range, we confirmed the optical array of the achiral planar metamaterial.

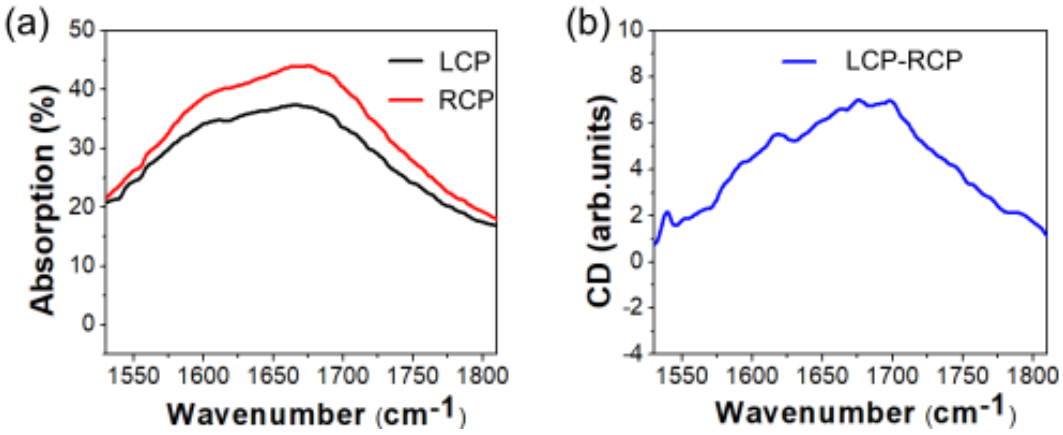

Figure 3.12(a) Absorption of microdisks measured with FTIR for right right -handed (black) and left -handed (red) circular polarization. (b) Circular Dichroism (CD) corresponding to the the difference of absoprtion ΔA between LCP and RCP, measured with FTIR.

3.2.3 Experimental setup

The sample is illuminated by QCL IR pulsed laser with wavelength 5.5 to 6.5 μm (1538-1818 cm^{-1}) at the angle of 70° from normal to the sample (20 ° from the sample plane) with power of 3.45 mW. The laser light is linearly polarized with vertical direction at the laser output Figure 3.13.

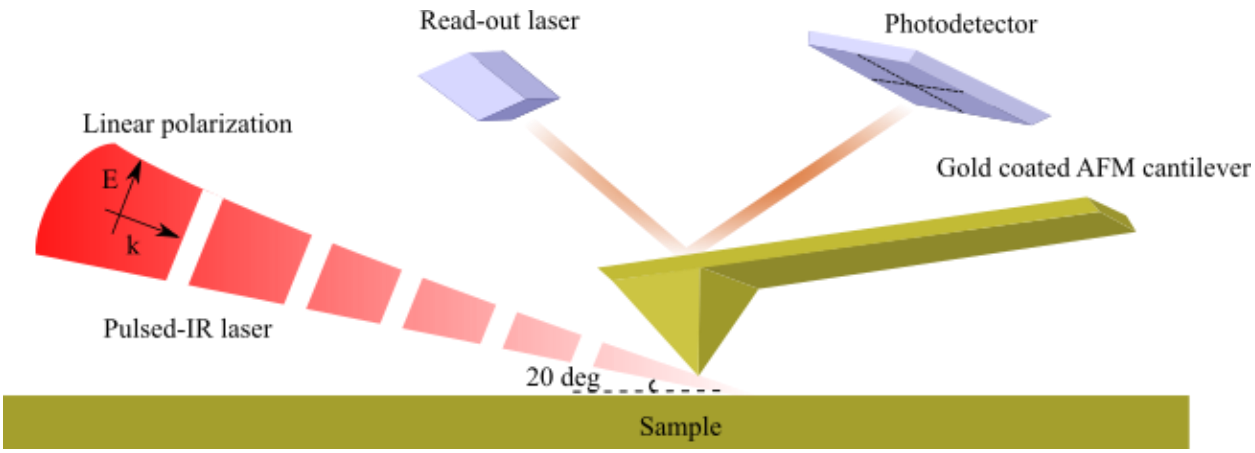

Figure 3.13 Schematic of AFM-IR setup, the sample is illuminated with QCL IR pulsed laser at 20 degrees from the sample plane. The laser light is linearly polarized.

The laser light is focused beneath the gold coated AFM tip using Au-coated curved mirrors to obtain a focused spot, which has the shape of an ellipse with about 50 μm*100 μm as shown in Figure 3.14. The map presented here corresponds to the variation of photothermal expansion of a homogeneous material due to the laser excitation. The area covered by the highest amplitude shown in red overlaps with about 80-100 microdisks, thus we make the approximation that the few disks probed at the center of this region are illuminated with constant light.

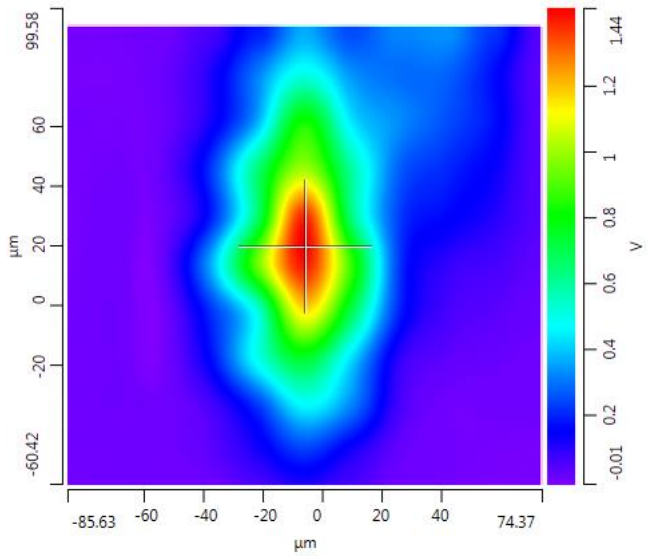

Figure 3.14 Profile of the region affected by the QCL laser spot on the sample obtained in AFM-IR system.

To change the linear polarization of our laser light to circular polarization, a quarter waveplate was placed at the output of the laser. A quarter waveplate is a birefringence material with two orthogonal refractive index which are called ordinary (n_o) and extraordinary (n_e) axis. The polarization component has different speed along each axis meaning along the ordinary axis the speed is $v_o = \frac{c}{n_o}$, and along the extraordinary axis is $v_e = \frac{c}{n_e}$. When $n_e < n_o$, the extraordinary axis is called the fast axis and the ordinary axis is called slow axis. The quarter waveplate generates the $\frac{\pi}{2}$ phase shift between the polarization components.

To make sure that the light is circularly polarized light, an analyzer was aligned with the laser light after the quarter waveplate in front of IR detector. In order to find the principal axes of the quarter waveplate, the quarter waveplate located between aligned polarizer and analyzer was rotated until the maximum intensity was transmitted to the detector (Figure 3.15.a). Once the first principal axis

was located, the second axis was deducted as it is perpendicular to the principal one. Circular polarization is obtained by adjusting one of principal axes at an angle of 45° from the polarization of light. To confirm that the polarization was circular in this configuration, we rotated the analyzer continuously and recorded the intensity of transmitted light to detector. For a circular polarization, the intensity of the transmitted light should be constant for all angles of rotation, as shown in the Figure 3.15.b. Elliptical polarization is obtained by setting one of the principal axes at angle θ (different from 45) from the polarization of light. As shown in Figure 3.15.c when we rotate the analyzer in the case of elliptical polarization, the intensity varies as a function of the angle considered.

With the principal axis defined, the quarter waveplate can be aligned with the optimal angle in front of the laser aperture, in such a way that the linear polarization of laser light makes 45° from the slow axis of the quarter waveplate.

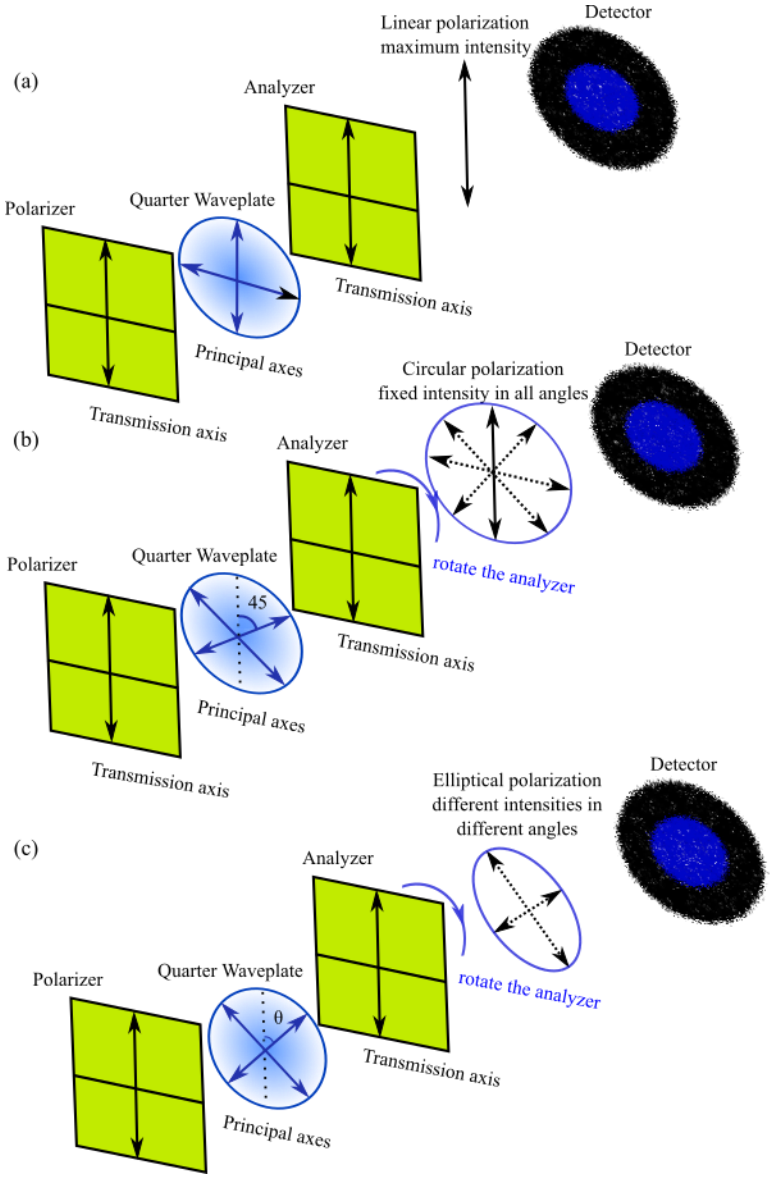

Figure 3.15 Identification of the principal axes of quarter waveplate. a) When the transmission axis of polarizer and analyzer are aligned with the quarter waveplate principal axis, b) When the transmission axis of polarizer makes a 45º angle with the principal axes of quarter waveplate, c) When the transmission axis of polarizer makes an angle θ degrees with the principal axis of the quarter waveplate.

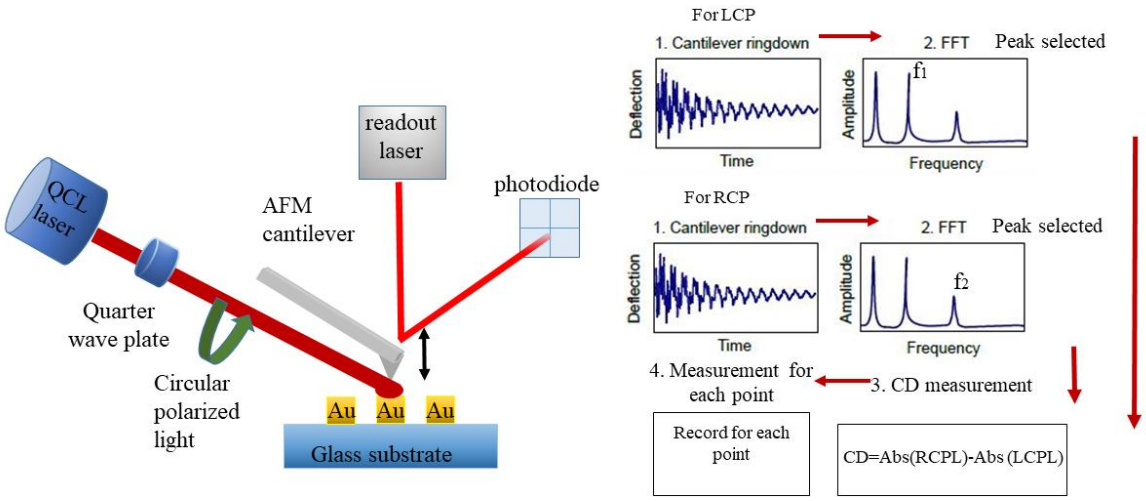

Figure 3.16. Developed chiroptical set up to measure circular dichroism locally. The light is polarized circularly using a quarterwave plate. The absortioin due to RCP and LCP light is measured separately. CD is obtained by subtrating the respective intensities obtained with LCP and RCP.

For the AFM measurement, after the light is aligned on the AFM tip, the cantilever is engaged in contact with the sample to monitor the photothermal expansion of the material. which is indicative of the heat released caused by molecular vibrations excited in the material. To enable the detection, the laser is pulsed at a fixed frequency, which makes it possible to detect using either a lock-in amplifier measurement or FFT of the AFM signal to monitor the amplitude at the selected frequency. To detect the minute amount of force generated by the expansion of the material beneath the AFM tip, we match the QCL laser pulse with one of the resonances of the AFM

cantilever [110]. At a fixed location, an IR spectrum of the material in contact with the tip can be obtained by sweeping the wavelength of illumination. At a fixed wavelength, a map of the photothermal expansion across the disks can be obtained. We explore the local chiroptical properties of the metamaterial substrate with nanoscale AFM-IR platform shown in Figure 3.16. The spatial resolution of this approach has previously been evaluated by the radius of apex of AFM tip, commercialized AFM tip normally have spatial resolution about less than 20 nm and in some cases down to molecular and atomic scale [10]. With this technique, near field absorption of metamaterial such as ring resonator [60] and planar chiral plasmonic structure [111] were reported previously.

3.3 Results and discussions

3.3.1 AFM-IR photothermal expansion of plasmonic structure for linear polarization

For all data presented in Figure 3.17 the polarization of the laser was linear. The spectrum representative of a local photothermal response of the microdisk measured with AFM-IR is presented in Figure 3.17 a. Direct comparison with the FTIR spectrum of the array for the 1530-1810 cm^{-1} range confirms the validity of the AFM-IR signature. We also evaluated the variations in photothermal expansion at different locations on the disk. In the left region of the disk (red), the amplitude is about half the value of the one collected in the right side (green) and at the top (yellow) of the structure. It is well known that plasmonic structures, such as those in metamaterials, locally enhance the electromagnetic fields at resonance, leading to joule (ohmic) heating in the metallic volume well above the environment temperature. Finite difference time domain (FDTD) simulations were carried out to obtain the optical response of the microarray. Figure 3.17.c shows

the density of absorbed power spatial distribution for off-normal TM illumination along the microarray axis at resonance, which is given by

$$P_{abs}(\mathbf{r}) = -\varepsilon_0 \omega \mathrm{Im}(\varepsilon(\mathbf{r}))|\mathbf{E}(\mathbf{r})|^2 \qquad (1)$$

where ε_0 is the vacuum electrical permittivity, ω is the optical frequency and $\varepsilon(\mathbf{r})$ is the spatial relative electrical permittivity and $\mathbf{E}(\mathbf{r})$ is the local electric field. Such an absorbed power density produces local heat [112, 113] , which further produce thermal expansion effects observed in the AFM-IR characterization.

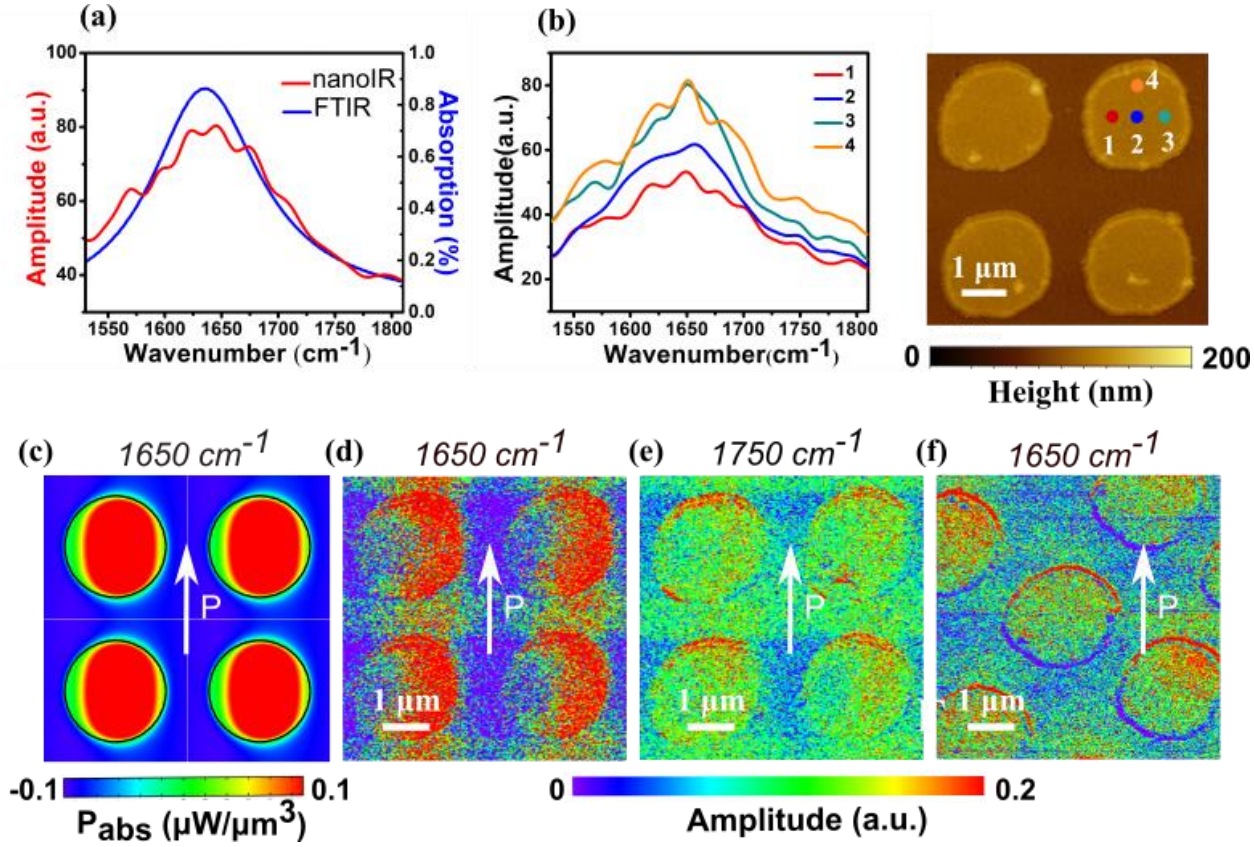

Figure 3.17 (a) Comparison of a representative AFM-IR spectrum obtained locally on a microdisk and the far-field absorption FTIR spectrum of the microdisk array. (b) AFM-IR spectra obtained at four different positions on the microdisks, indicated on the AFM topography. (c) FDTD calculated spatial distribution of the absorbed power for off-normal TM polarization, shown as P. (d-f) AFM-IR photothermal expansion maps for TM polarization along the microarray lattice axis with illumination at 1650 cm^{-1}(d), 1750 cm^{-1}(e) and TM polarization at 45° and illumination at 1650 cm^{-1} (f).

Across the disks, the position of the maximum absorption remained constant ~1650 cm^{-1}. Hence, the illumination wavelength was fixed at 1650 cm^{-1} to map the variations in photothermal amplitude across four microdisks (Figure 3.17.d-e). Regions with highest photothermal expansion

(hot spots) were observed across the achiral metamaterial at 1650 cm^{-1}, when the illumination wavelength matches with the maximum absorption of the structure (Figure 3.17.d) whereas the amplitude decreased significantly with no notable hot spot when the excitation wavelength was detuned (Figure 3.17.e).

Overall, the absorption profiles are in good agreement with FDTD maximum absorption $\lambda = 1650$ cm^{-1} Figure 3.17.e, despite a deviation from the predicted absorption in the center of the disk. The slight differences in patterns between the experimental and the computational maps can be explained by slight variations in the direction of illumination of IR laser in the instrument (obtained with a curved mirror) and what we calculated in the theory (parallel incident light). These results indicate that AFM-IR can detect local variations in the metamaterial that were not attainable with conventional methods or computational modeling. However, the orientation of the metasurface with respect to the EM field and polarization should be carefully optimized as demonstrated in Figure 3.17.f. When changing the orientation of the array, the expansion of the microdisks was significantly lowered (by a factor of 10 in this case). In addition, a dipolar response with highest signal measured at the top of the structure and lowest signal at the bottom was observed in this orientation.

We repeated the measurements after coating the arrays with the low-absorption polymer SU8 (40nm thickness), which exhibit a higher photothermal expansion. As shown in Figure 3.18, the signal could be enhanced about 100 times with this scheme. As the polymer is amorphous, the expansion obtained is expected to be higher than for a crystalline material. The photothermal expansion maps were obtained for three wavenumbers as shown in the Figure 3.18 a,b, and c. It

was confirmed that the maximum signal is observed at 1650 $cm^{1.}$ And that no hot spot is observed off-resonance such as 1750 cm^{-1}.

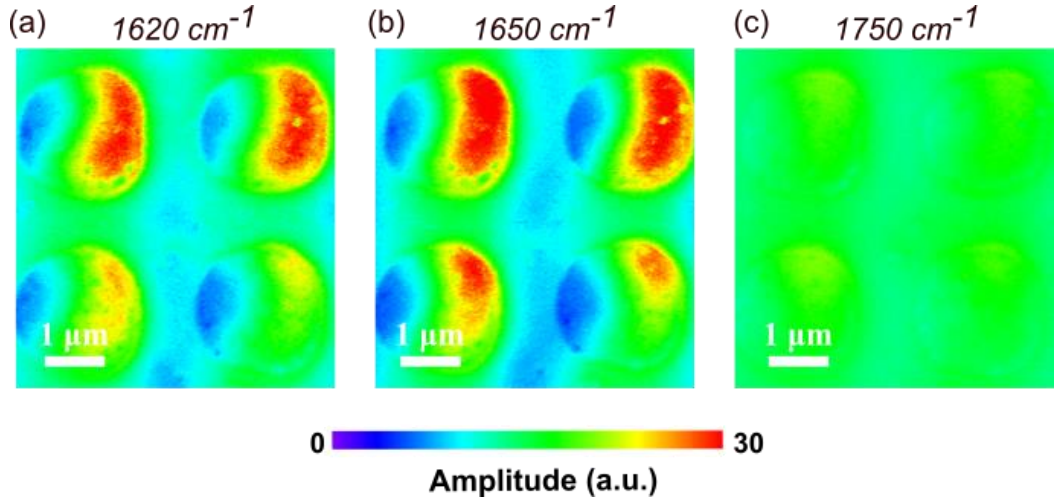

Figure 3.18 Photothermal expansion map for microdisks covered with about 40 nm of polymer SU8, at different wavenumbers, (a) 1620 cm^{-1} , (b) 1650 cm^{-1} , and (c) 1750 cm^{-1}

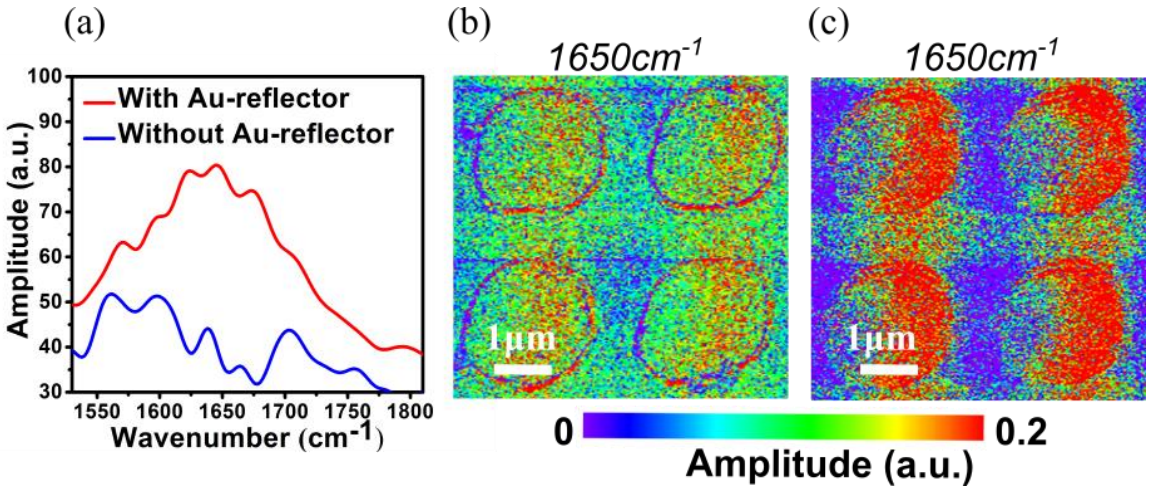

Figure 3.19 (a) Comparing the localized spectral response of microdisks with and without Au reflector at the center of the microdisk, (b). Absorption profile of microdisks without Au reflector at 1650 cm^{-1}, (c). Absorption profile of microdisks with Au reflector at 1650 c

Now that the settings for maximal photothermal expansion have been determined, we study the effect of the Au reflector (Fabry-Pérot cavity) on the signal. We find that the presence of the cavity doubles the response of the microdisks, as shown in Figure 3.19.a. Figure 3.19 b, and c show the photothermal expansion map at 1650 cm^{-1} for the microdisks array with and without cavity [97, 114]. As described earlier, the cavity confines the electromagnetic field in LSPP at the top interface, thus enhancing the photothermal response locally. The propagation phase inside the cavity is proportional to optical path length *k.n.L* where k is the wavenumber, n is the refractive index of dielectric medium and L is the thickness of dielectric spacer. C For our proposed plasmonic structure, FDTD calculation shows the strongest absorption for SiO_2 dielectric spacer for thickness of L=100 nm. hanging any of these parameters leads in different absorption spectra, which will be studied in more details in the future.

3.3.2 AFM-IR photothermal expansion of plasmonic structure for circular polarization

Next, we studied the local CD signal of the structures by using a quarter waveplate in front of the laser beam path to generate circular polarization of the incident light. In Figure 3.20, the spatially resolved map of the structures responding to LCP and RCP light at λ = 1650 cm^{-1} and the subtraction of these two maps are presented. The microdisks clearly exhibit different photothermal response when illuminated with LCP and RCP light, suggesting that this achiral plasmonic substrate can be exploited for circular dichroism (CD) spectroscopy at nanoscale. Our results are in good agreement with the FDTD simulations of CD (Figure 3.20.d).

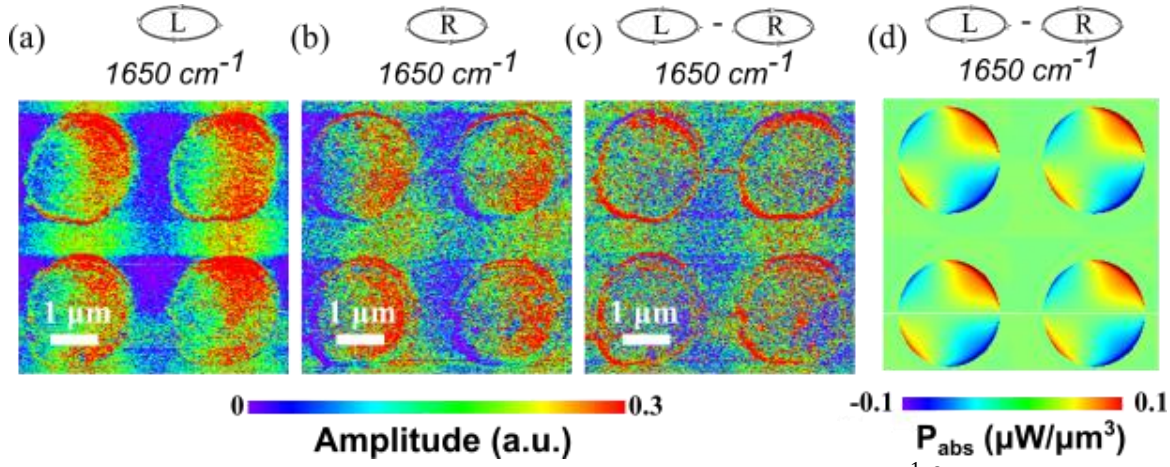

Figure 3.20 AFM-IR photothermal expansion map obtained at 1650 cm^{-1} for (a) LCP light, (b) RCP light, (c) Resulting difference between the photothermal expansion images obtained in (a) and (b) representing $A(1650)_{LCP}$ - $A(1650)_{RCP}$, (d) Corresponding P_{abs} calculated by FDTD by subtracting the Pabs of LCP and RCP models.

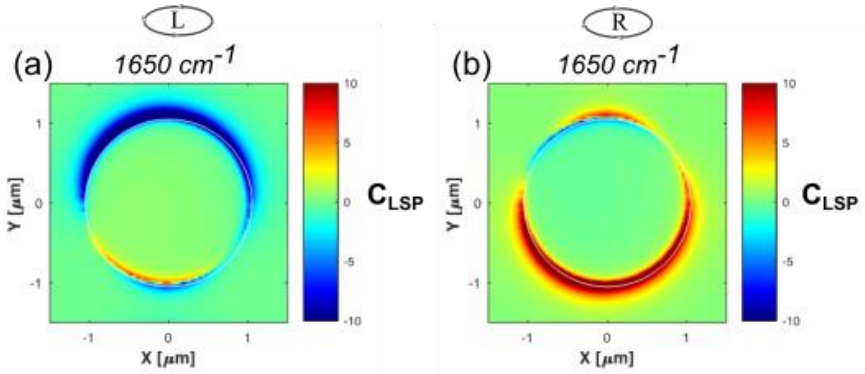

Figure 3.21 Free space normalized calculated optical chirality C of localized surface plasmons (LSP) for (a) LCP and (b) RCP illumination. Blue shows that the helicity of the near field is left-handed due to LCP illumination, and red shows that the helicity of near field is right-handed due to the RCP illumination.

To explain our experimental data, the optical chirality (C) is calculated by FDTD simulation at 5 nm above the microdisks 1650 cm^{-1} . The free space normalized optical chirality is calculated for LCP and RCP illumination at an angle of 70^{oo} from the normal to the substrate surface, by:

$$C(r) = -\frac{1}{2}\,\varepsilon_0 \omega\, Im\,(E^*.B) \qquad (2)$$

Figure 3.21 shows the free space normalized near field optical chirality C of a microdisk unit cell for LCP and RCP illumination. The C has the same handedness as the chirality of incident light. The blue region in Figure 3.21 a shows that the helicity of the near field exhibits left-handed chirality due to LCP illumination, while the red region in Figure 3.21 b shows the right-handed helicity of the near field due to the RCP illumination.

These results suggest that when chiral molecules are located in these regions, stronger interaction with chiral light will occur based on their chirality. For example, we expect to have strongest photothermal expansion signal from left-handed molecules at regions where the stronger signal appears in Figure 3.20 a and Figure 3.21 a overlap due to LCP illumination. In the next section, we will investigate this hypothesis.

3.3.3 Vibrational-CD spectroscopy at nanoscale

Next, we exploited the previously discussed enhanced plasmonic electromagnetic field to excite Poly-L-lysine, a known left-handed chiral molecule with absorption in the same range as the plasmonic resonance around 1650 cm^{-1} [115], as shown in Figure 3.22. This band corresponds to C=O stretching and a small amount of C-N stretching in Amide I [116].The vibrational circular

dichroism (VCD) of the molecule also lies in the same regions, with couplet of 1640/1660 cm^{-1} representative of a α-helix.

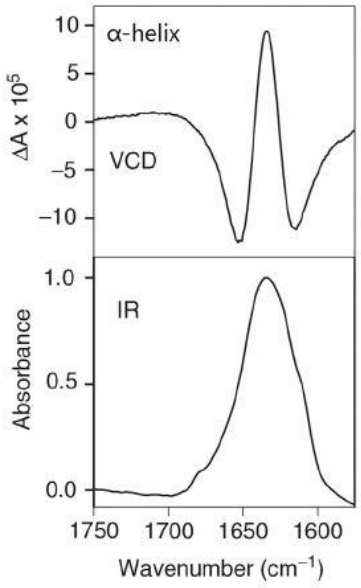

Figure 3.22 IR absorption and vibrational circular dichroism (VCD) of Poly-L-Lysine - from reference [115].

Here, we used Poly-L Lysine (1% (w/v) in H_2O) from Sigma. 3 μL of Poly-L-lysine solution was drop casted on cavity coupled microdisks array and air dried. Poly L lysine was illuminated with circularly polarized light with power of 0.44 mW. The AFM height image of microdisks covered with Poly-L-lysine is shown in (Figure 3.24 a). Since Poly-L-lysine is left handed, it is expected to respond more strongly to left handed circular polarized light. As shown in Figure 3.23 b and c, we did indeed observe higher photothermal absorption signal of Poly-L-Lysine for left handed polarization and a weaker AFM-IR signal for right handed polarization. The response of Poly-L-lysine molecules without cavity and without plasmonic structure was also measured as a control. A clean glass slide was used as the substrate. For the same amount of Poly-L-lysine, the signal

was about two orders of magnitude smaller, as shown in Figure 3.23.a. We found that when Poly-L-lysine molecules were located in the vicinity of interface, in the range of the evanescent field, they exhibited stronger response than for thicker films. This will have to be carefully quantified in future studies.

In the subtracted image in Figure 3.24.d, we find that the left-handed molecules have a stronger signal on the top side of microdisk which is related to the region with superchiral left-handed near field was predicted Figure 3.23 a (blue regions). This is the region where left-handed molecules have stronger interaction with chiral light.

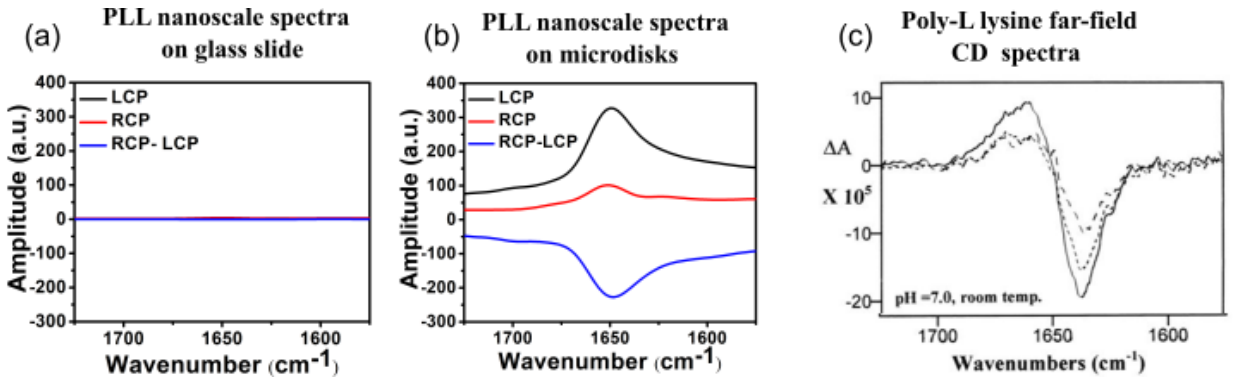

Figure3.23 (a). AFM-IR spectra of Poly-L-lysine on glass substrate, (b). AFM-IR spectra of Poly-L-lysine on microdisks with Au-reflector, (c). Comparison of circular dichroism of Poly-L-lysine on microdisks with Au-reflector and glass substrate [117].

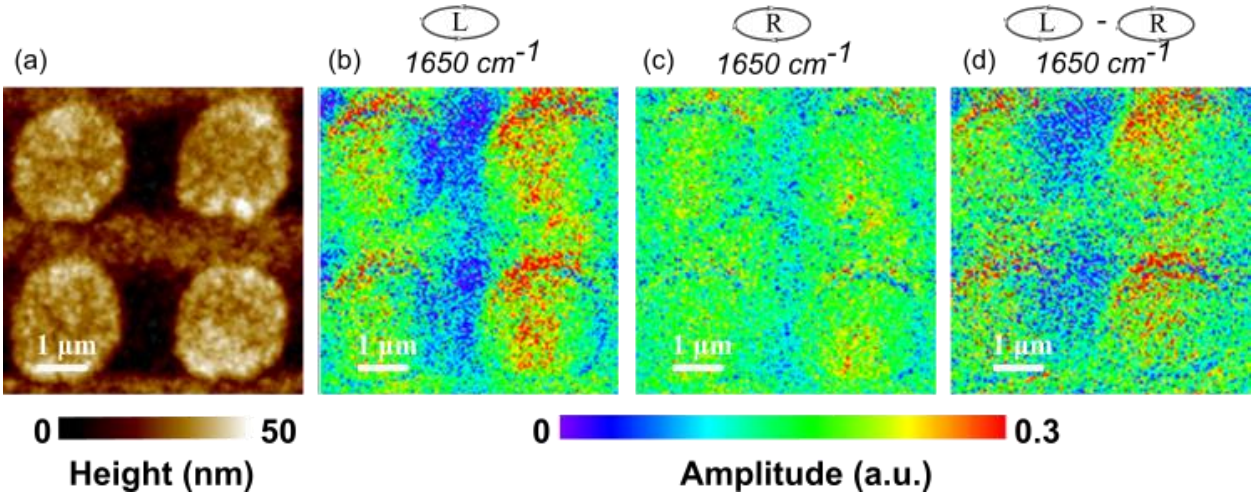

Figure 3.24.(a) Height image of microdisks covered with Poly-L-lysine. (b-c) AFM-IR photothermal expansion maps obtained at illumination wavelength 1650 cm^{-1} for Poly-L-lysine covered microdisks for polarizarion (b) LCP and (c) RCP illumination, (d) Localized CD map at 1650 cm^{-1} resulting from $A(\lambda)_{LCPL}$ - $A(\lambda)_{RCPL}$ in the form of the photothermal absorption in the microsdisks under circular polarized light of left and right handedness.

3.3.4 IR nanopolarimetry of Poly-L Lysine beyond vCD

Anisotropy is a crucial factor in biological and medical research including for diagnostics of some disease such as cardiovascular [118], and Alzheimer diseases [119-121] . Polarized light plays an important role to understand the asymmetric nature of biological molecules, differentiating between normal and precancerous cells in tissue layer [122], beyond CD. Infrared spectroscopic ellipsometry and polarimetry are the characterization techniques for studying anisotropy at macroscopic scale [123]. Anisotropy in structure is associated with the molecular architecture (orientation) and morphology at the nanoscale, which cannot be determined with conventional IR

methods due to the diffraction limit. Near field spectroscopy [124, 125] and AFM-IR have been used as a polarimetric and polarization dependent technique for nanoscale studies [126].

Here, we demonstrate the absorption of Poly-L Lysine (1% (w/v) inH_2O) with AFM-IR technique at nanoscale for linear polarized light and also for different elliptical polarizations. Poly-L Lysine is drop casted on gold substrate and then dried in air without heating. The IR spectra of Poly-L-Lysine are measured for different thicknesses of Poly-L-Lysine deposited (80, 400, 600 nm). First, each sample is illuminated with linear polarization at 1650 cm^{-1} with 11.52% of the laser power. As shown in Figure 3.25, by increasing the thickness of the protein or in other words by increasing the density of molecules, the IR absorption signal is getting stronger, up to a threshold. Next, by rotating the principal axis of quarter wave plate for different angles, the sample is illuminated with different elliptical polarizations. As shown in the Figure 3.26, the wavenumber is fixed at 1650 cm^{-1} while the tip is scanning over the sample for different polarization of light, and photothermal expansion map is obtained for each polarization. Here we demonstrate that Poly-L Lysine is anisotropic protein and polarization sensitive molecule. For four different angles, different maps are obtained. Figure 3.28.b is on the closest angle to circularly polarized light (only 3º off from circularly polarized light). The yellow regions demonstrate that the molecules have higher photothermal expansion than other regions based on the scale bar data. For Figures 3.28.a, b, and c, we can recognize that for elliptical polarization the photothermal expansion signal is not as strong as for close-to-circular polarization (Figure 3.28.b). The absorption changes as a function of the orientation of the chiral molecules with respect to the polarization of light. This should be quantified in more details in the future.

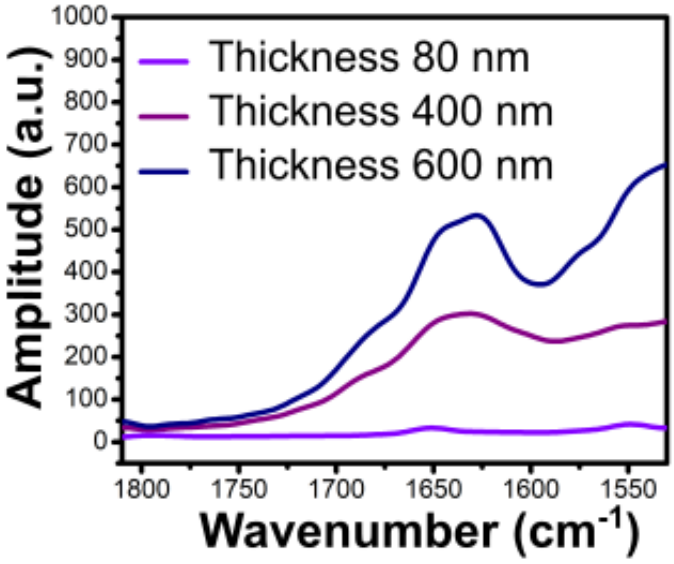

Figure 3.25 IR absorption spectra measured by AFM-IR at nanoscale for different thicknesses 80. 400, 600 nm of Poly-L lysine on gold substrate.

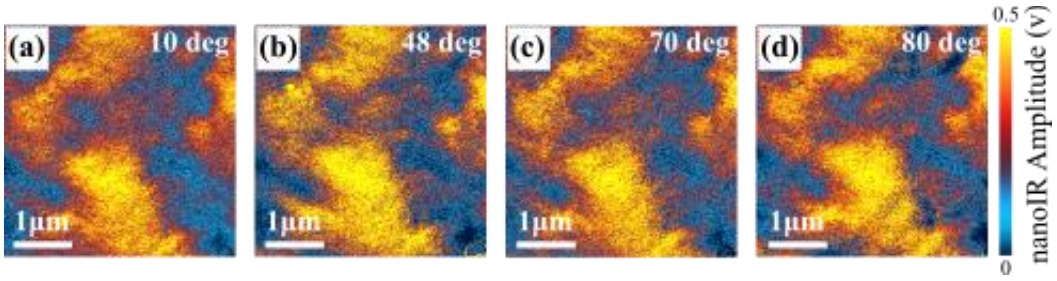

Figure 3.26 NanoIR map of Poly-L lysine on gold substrate for four different elliptical polarizations, when the principal axis is at 10, 48, 70, 80 degrees at a fixed wavenumber 1650 cm^{-1}.

3.4 Conclusion

The emergence of AFM-IR in nanoscience technology has brought about new opportunities for nanoscale chemical characterization. This new technique has overcome major limitation in both IR spectroscopy and AFM. Here, we develop and provide initial considerations for a technique aiming at enhancing circular dichroism spectroscopy by using achiral cavity coupled microdisk structures and a high spatial resolution AFM-IR. This technique makes it possible to characterize the handedness of molecules, just in homogeneous solution, but with the potential to extend it to heterogeneous sample such as racemic drugs or complex biological tissues. Overall, we showed a preliminary study of nano-polarimetry with AFM-IR can be used for anisotropic samples.

CHAPTER 4 BACTERIA CHARACTERIZATION

4.1 Introduction

Bacterial infections can cause serious health concerns in humans, animals, and plants. In recent years, antibiotics or other products such as copper-based treatments are used to treat bacterial infections. However, their widespread use is leading to a global challenge of multidrug-resistance, which poses severe threats to humans. This highlights an urgent need for the development of new compounds to efficiently kill pathogenic microorganisms when today's treatments fail [127].

Advances in nanotechnology have provided a plethora of applications, including for nanoparticle-based disinfectant and therapeutic systems. These are now considered as promising a new generation of antibacterial treatments, because of their unique physical and chemical properties. Nanoparticle-based treatments have been found to be very potent due to the high surface area interacting with the cells. In addition, nanoparticles can design multifunctional systems that will introduce new modes of actions to inhibit bacterial growth and bypass the developing resistance [128]. Because of these new opportunities, understanding the detailed mechanisms of interactions between nanoparticles and living systems is becoming of paramount importance. The mechanisms of antibacterial activity of nanoparticles are known to be nanoparticle-dependent, but are not yet well understood. Accessing the information locally, at the site of nanoparticle-cell interaction, or tracking nanoparticle penetration into a cell has proven difficult with conventional optical microscopic techniques, as well as with high spatial

resolution imaging such as electron microscopy and scanning probe microscopy. Nonetheless a wealth of information available with these techniques has not yet been exploited for antibacterial studies.

In this chapter, the consequences of the interaction of antibacterial nanoparticles with plant pathogens are explored with high spatial resolution imaging and AFM-IR. Our results illustrate the importance of considering local variations in cells to get a more complete picture of processes of interest for large scale applications such as antibacterial treatments in field conditions.

4.2 Bacteria and their cell wall composition

Bacteria are classified in two groups based on the composition of their cell wall: Gram- positive and Gram-negative. As shown in Figure 4.1a., Gram-positive bacteria have a thick cell wall composed of peptidoglycans and teichoic acids. Peptidoglycan is a negatively charged polymer composed of glycan strands formed from disaccharide residues cross-linked with amino acids. The peptidoglycan layer is responsible for maintaining the cellular shape among other functions ensuring cell viability. Teichoic acids are anionic glycerol phosphate-containing polymers, which are joined to either the peptidoglycan or to the membrane lipids [129].

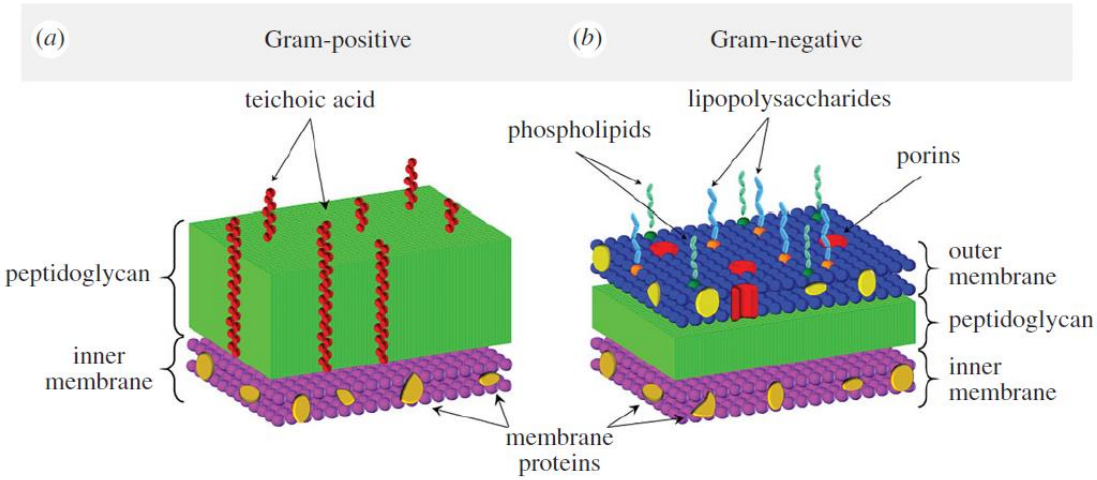

Figure .4.1 Schematic illustration of the composition of the cell wall for a) Gram-positive and b) Gram-negative bacteria [130].

In contrast, Gram-negative bacteria have an outer and inner membrane separated by a thin layer of peptidoglycans, as shown in Figure 4.1b. The outer membrane of Gram-negative bacteria contains lipopolysaccharides, phospholipids and porins. It acts as a barrier to the external environment. It is also responsible for nutrition uptake and waste removal through porins [130].

4.3 Bacterial diseases in plants

Microbial diseases in plants are very common. Most lesions observed on plant leaves, vegetables or fruits are the result of bacterial or fungal infections. The infections can be superficial or systemic. Here we focus on bacterial spot disease in tomato plants.

Bacterial spot disease was identified first in South Africa in 1921. Four species of *Xanthomonas* bacteria have been associated to the disease in tomatoes*: Xanthomonas euvesicatoria, X. perforans, X. gardenri, and X. vesicatoria* [131]. These are Gram negative bacteria. *X. perforans*

is a dominant strain in Florida since 2006 [132]. The lesions on tomatoes resulting from this infection are shown in Fig. 4.2.b. They also affect stems and leaves and can result in defoliation of the plant and early tomato drop. At the single cell level, the bacteria form bacilli shaped with length of 1-3 µm and width of 0.4-1 µm, as shown in Figure 4.2.a. A study of the 2007-2008 production costs and market values evaluated tomato losses attributed to bacterial spot disease to about $3090 per acre in southwest Florida [133]. The problem worsened since then.

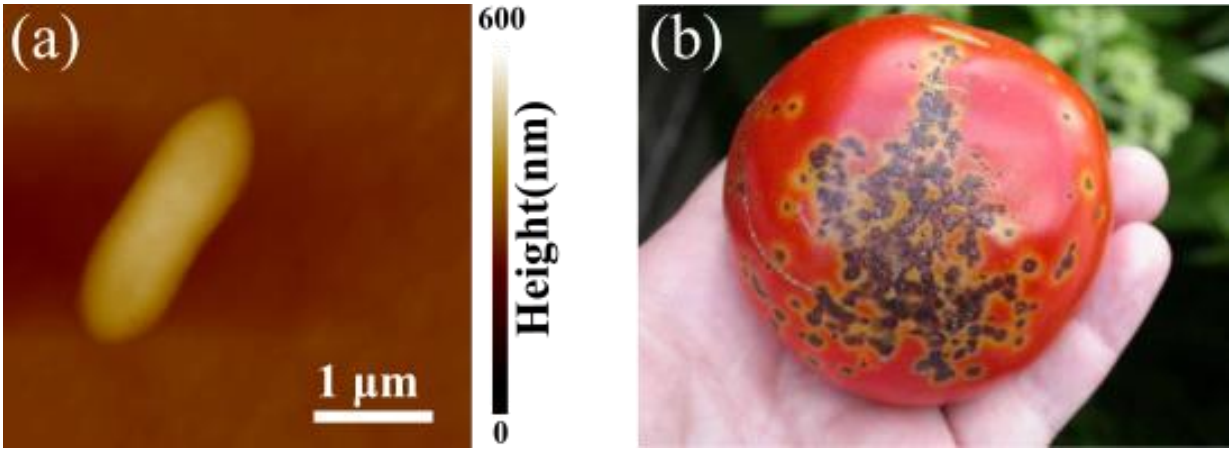

Figure 4.2 a) AFM height image of *Xanthomonas perforans* b) Tomato bacterial spot disease

One challenge in managing plant diseases, in general, is that the conventional bactericides on the market have become ineffective in killing the bacteria. In addition, the leaching of the high concentration of Copper used to overcome the resistance to the soil and surrounding water poses significant and growing environmental threats.

4.4 Plant bacteria treatment

Traditional management of bacteria in plants current involves copper-based bactericides mostly. Antibiotics, such as streptomycin, were used in the 1950s and early 1960s but bacteria quickly developed resistance [134]. Since then bacteria have also developed tolerance to Copper, which is today resulting in high resistance [135].

For tomatoes, new disease management plans have been evaluated, such as the adding of a non-Cu compound to the treatment cocktail to increase of the modes of actions. Mancozeb, a dithiocarbamate mixture, was for instance added to copper-based bactericides to treat *Xanthomonas vesicatoria*. The results showed that the benefits were limited in presence of copper tolerant bacteria [131]. Another study showed that a small molecule additive, 2-aminoimidazole (2AI), combined with copper successfully controlled biofilm formation of *Xanthomonas euvesicatoria* [136]. Paret et al. demonstrated the benefit of light activated nanoscale Titanium dioxide (TiO_2) and nanoscale TiO_2 doped with different elements such as zinc (Zn) and silver (Ag) to manage the bacterial spot. However, this technique exhibited signs of plant phytotoxicity [137]. Silver (Ag) nanoparticles have been considered due to their antimicrobial activity *in vitro*, against animal pathogens such as *Escherichia Coli*, Hepatitis B virus and human immunodeficiency virus type1 [138]. Unfortunately, aggregation problems arose in the environment of the plant [139, 140].

From this brief review of the literature, it is evident that more efficient disease management approaches are needed to benefit sustainability and yields in plant-based food production. To better understand the rules of design with positive impact on this area of research, developing better suited characterization platforms is critical. For instance, the ability to understand the mechanism

of bacterial resistance and the antibacterial activity of NPs to develop more effective antimicrobial materials would be very valuable.

4.5 Antibacterial mechanisms of action of nanoparticles

Various modes of actions have been reported for nanoparticles used as antibacterial formulations. Metal NPs can modify the metabolic activity of bacteria leading to bacterial death. In other cases, NPs penetrate cells and biofilms, which results in inhibition of growth [127]. NPs can instead interact with bacterial cell's components such as ribosomes, DNA, and enzymes [127]. Other proposed antibacterial mechanisms include: to modify the cell membrane permeability, disrupt the cell wall (Figure 4.3 a and b - respectively), to generate reactive oxygen species (ROS) (Figure 4.3 d), to deactivate proteins, or to inhibit enzyme activity [141-143]. Size, shape, surface charge, zeta potential, crystal structure, doping modification and surface morphology can all impact the actions of NPs on the bacterial cell [144]. Decreasing the nanoparticle size increases the surface area to volume ratio, which leads to greater surface interaction with cells. Reactivity can also be tuned with these properties [127].

Cell wall or membrane constitutes a barrier between the external environment and bacterial content. Changes in chemistry of cell membrane, such as between Gram positive and negative bacteria, can affect the nature of the interaction with the nanoparticles. For Gram-negative bacteria, lipopolysaccharides on the outer layer of the cell are negatively charged. Thus, they tend to attract positively charged nanoparticles electrostatically. Gram-positive bacteria have teichoic acid and peptidoglycan on their cell walls, which has been shown to allow foreign molecules to penetrate [130]. Membrane damage and cell death from nanoparticle treatments have been reported on

Gram-positive bacteria [145]. In addition, the membrane is negatively charged, which can electrostatically attract positively charged nanoparticles [127]. Despite the general considerations, the charge of the membrane can vary over time and under various environments. Thus, the antimicrobial mechanisms of action of NPs should be studied on a case-by-case basis until a more general model can be unveiled.

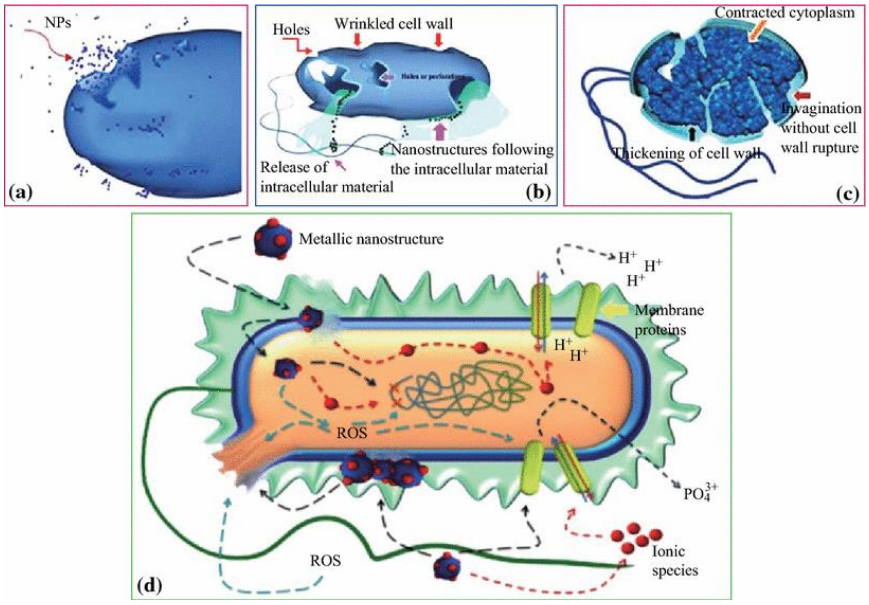

Figure 4.3 Antibacterial activity of metal NPs a), b) and c) decomposition of cellular membrane, and release of intercellular material d) generation of oxidative stress (ROS) [146]

One important antibacterial mechanism of nanoparticles is the formation of Reactive Oxygen Species (ROS). Four different ROS types have been reported in [127]:the superoxide radical (O_2^-), the hydroxyl radicals ($OH^{\cdot}$), hydrogen peroxide (H_2O_2), and singlet oxygen (O_2). Different types of nanoparticles have been found to generate different types of ROS. For instance, copper oxide (CuO) nanoparticles which are roughly spherical with a diameter of 50-60 nm [147] seem to generate four types of ROS, whereas zinc oxide (ZnO) nanoparticles which have hexagonal shape

with particle size of 60 nm produce only H_2O_2, and $OH^{\cdot}$ [148]. The creation of ROS is related to the presence of defect sites in the surface of the NPs, such as vacancies or structural defects. Although ROS generation in bacterial cells is safe as it remains under a threshold, the excessive production of ROS can generate oxidative stress and harm the components of bacterial cells. ROS can affect the permeability and integrity of the cell membranes [149] or disrupt the activity of specific enzymes and proteins, which are responsible for regulating the morphology and physiological activity of cell membrane [150].

Other non-oxidative antibacterial mechanisms have been reported with MgO NPs on *E. coli*. Lipopolysaccharide and phosphatidylethanolamine did not change after treatment with MgO NPs. Rather, NPs bound to the membrane and released Mg ion, causing the pH to change [151]. Slowly dissolving metal ions from metal oxide NPs, which are then diffused through the cell wall has been described as a means to modify functional groups of proteins and nucleic acids like carboxyl (-COOH) groups and amino (-NH) groups. This interaction results in modifying the internal cell structure, changing the physiological process, and inhibiting the growth of the microorganism [152].

4.6 Conventional methods to assess antibacterial activity of nanoparticles

Common methods used to quantify the antimicrobial effects of a treatment on bacteria include plate counting, fluorescence bioassays for microscopy and flow cytometry, scanning electron microscopy (SEM), transmission electron microscopy (TEM) and IR spectroscopy. We provide a brief description of these methods in next subsections, including their advantages and limitations.

4.6.1 Plate counting

Plate counting is a basic microbiological technique that is routinely used to define the number of viable cells in a culture under selected treatment. In this method, healthy bacteria are selected and cultured on agar plate under exposure of NPs treatment. The number of viable cells is counted based on the colony forming unit (CFU) which is a measure of only viable bacterial and fungal cells. Plate counting starts with diluting the sample to obtain a concentration that can be easily counted. Afterwards, the sample is placed into an agar plate with mixing growth medium in the incubator at growth temperature for a pre-determined time, which depends on the sample and growth medium. After the incubation period, the bacterial colonies are counted. The remaining number of colonies after exposure to NPs is compared to the untreated control.

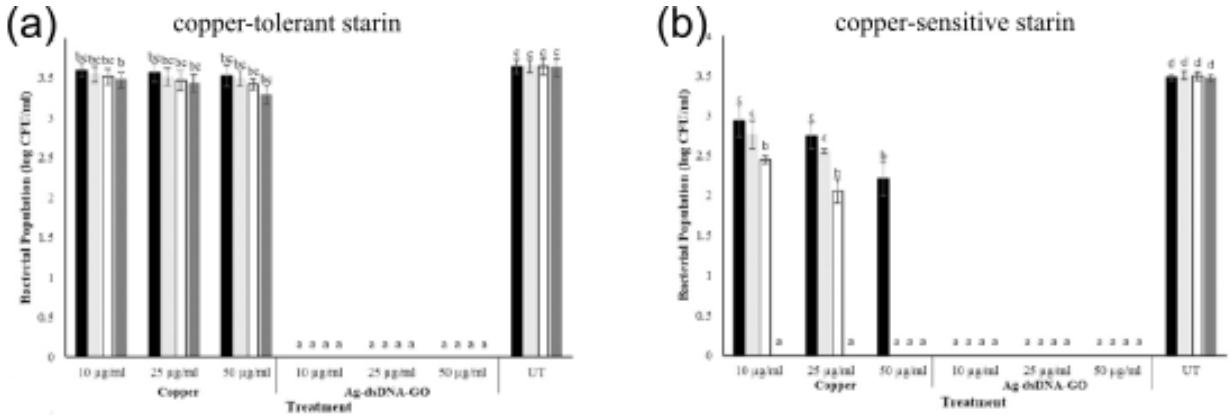

Figure 4.4 Plate-counting results of various concentration of Ag-dsDNA-GO and copper treatments on *Xanthomonas perforans* a) copper-tolerant and b) copper-sensitive survival over time. Black bars show over 15 min and gray bars show 1 h, white bars show 4 h, and light gray bars show 24 h [135].

Figure 4.4 shows the results of a plate counting experiment carried out on two types of treatments on copper-tolerant and copper-sensitive *X. perforans*. All concentrations of Ag-dsDNA-GO treatment, 10, 25, and 50 $\mu g/ml$, completely inhibit bacterial growth for both copper-tolerant and copper-sensitive bacteria. In contrast, none of the copper treatment concentrations was effective in inhibiting bacterial population for the copper-tolerant strain as shown in Figure 4.4.a. The bacterial growth was reduced for the same treatment on the copper-sensitive strains[135]. By this technique the concentration of treatment required to inhibit bacterial growth can be determined. However, the information regarding the kinetics of the treatment is not accessible. In addition, the mode of action remains unknown.

4.6.2 Epifluorescence microscopy

In this microscopy two kinds of viability dyes are used to distinguish viable and non-viable cells: propidium Iodide fluorescence dye (PI) (red dye) and SYTO 9 (green dye). PI is a nucleic acid binding dye which attaches to DNA, which makes it possible to track only permeant or dead cells. SYTO 9 is a protein binding dye which stains viable cells [153].

As shown in Figure 4.5, *E. coli* and *P. aeruginosa* are stained with SYTO 9 and PI before and after treatment. The results indicate that the treatment killed the cells in both cases [128]. The data is collected by illuminating the sample at the required wavelength to excite the dyes. The fluorescence emitted provides a rapid screening of the live / dead bacteria in the plates. However, it does not provide any information on the mechanisms of action or the bacterial response to the treatment.

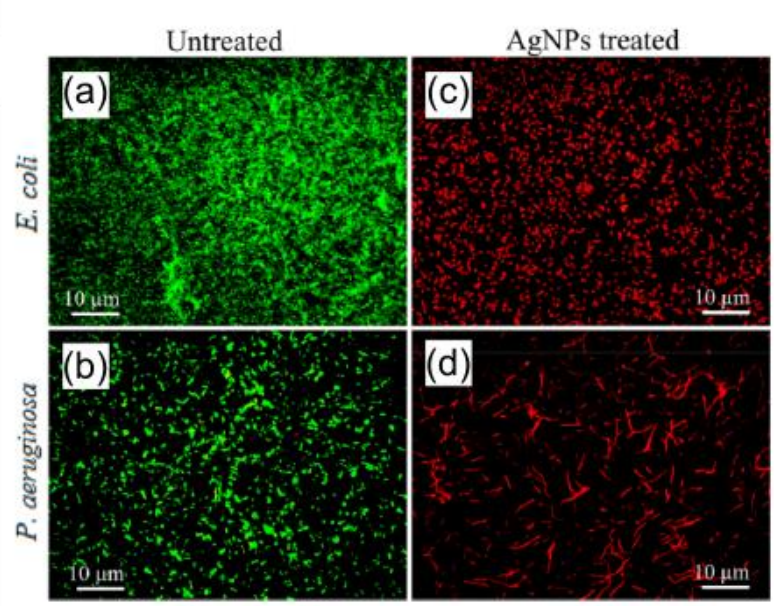

Figure 4.5 *E. coli* and *P. aeruginosa* before and after treatment with Ag NPs. The untreated bacteria appear in green indicated that they are intact and live cells (a and b), whereas treated bacteria in red which indicates that the cells are dead after treatment [128].

4.6.3 Flow cytometry

Flow cytometry is another technique to monitor the live and dead bacterial populations. Similar to the epifluorescence spectroscopy, the aforementioned two dyes (SYTO 9 and PI) are employed to identify live and dead bacteria. In flow cytometry, bacteria or cells flow through the chamber and pass across the laser light one by one for individual analysis. As shown in Figure 4.6, when a cell crosses the laser beam path, the light is scattered. The fluorescence of the scattered light is collected and provides the information of the status of the cell.

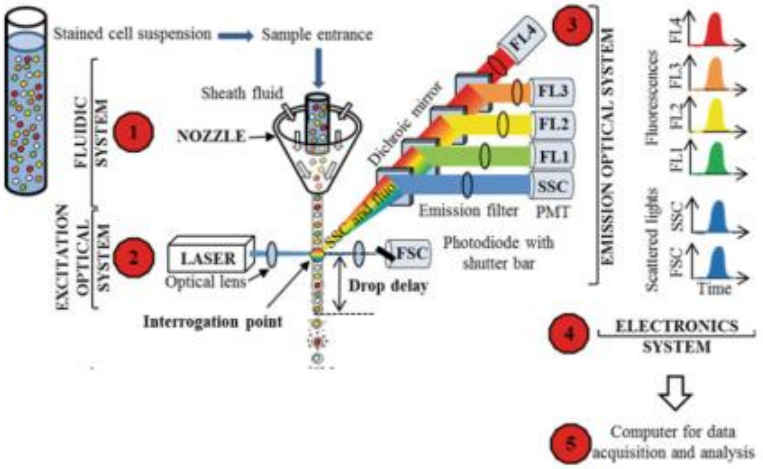

Figure 4.6 Schematic flow cytometer with forward scatter (FSC) detector and side scatter (SSC) detectors [154]

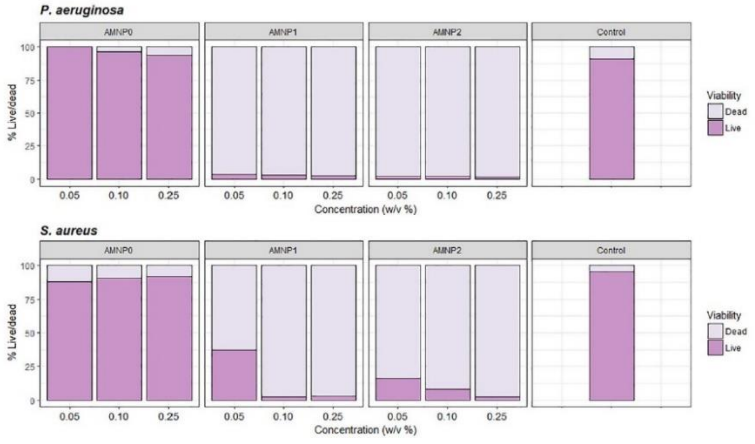

Figure 4.7 Viability of bacterial population before and after nanoparticle combination (AMNP0, AMNP1, and AMNP2) treatments measured by flow cytometry. These treatments efficacy is compared with the antibiotic (oxytetracycline) control. As the treatment concentration is increased, there is trend of dead bacteria [155].

4.6.4 Oxidative stress (ROS) detection assay

As explained in section 4.5, the interaction of NPs treatment with bacterial cell walls often leads to ROS which damages nucleic acids and proteins [128]. This intercellular ROS production can be detected by $H_2 - DCFDA$ assay. When $H_2 - DCFDA$ enters the cell membrane, it is oxidized in the presence of intercellular ROS and under excitation at 503 nm, it fluoresces (green). As shown in Figure 4.8, although ROS generation occurs even in control sample, the interactions of the bacterial cell with the nanoparticle treatment significantly increases ROS generation, as indicated in Figure 4.8 b. The positive and negative control (PC and NC) indicate the range expected for ROS in low and high oxidative stress conditions [128].

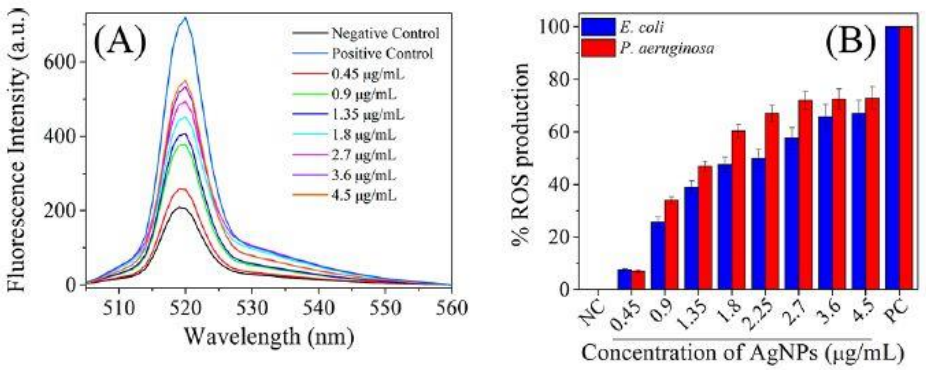

Figure 4.8 a) $H_2 - DCFDA$ assay for intercellular ROS generation detection for different concentration of Ag NPs, b) intercellular ROS generation due to Ag NPs which is concentration dependent for both *E. coli* and *P. aeruginosa.*

4.6.5 Scanning electron microscopy (SEM) and Transmission electron microscopy (TEM)

Electron microscopy are commonly used in characterizing nanoparticles and bacterial systems, even though the conditions for imaging require for the samples to be dry, coated with a metal and placed in high vacuum environment. In SEM the sample is bombarded with a focused beam of high energy electrons. The electron beam raster scans the sample. As the electrons interact with the sample, they generate secondary electrons and backscattered electrons that can be collected to gain some insight on the sample morphology.

Elemental analysis can be performed on the same system, using the electron beam to remove inner shell electrons and monitoring the X ray photons emitting as a high energy electron decays to fill the unoccupied inner shell state. The energy of the X-ray radiation can be assigned to specific atoms. This approach is called energy dispersive X-ray spectroscopy (EDS).

Figure 4.9 shows the SEM image of untreated *E.coli* and treated with Ag NPs. The EDS confirmed that attachment of Ag NPs caused bacterial death (Figure 4.9 c) [15].

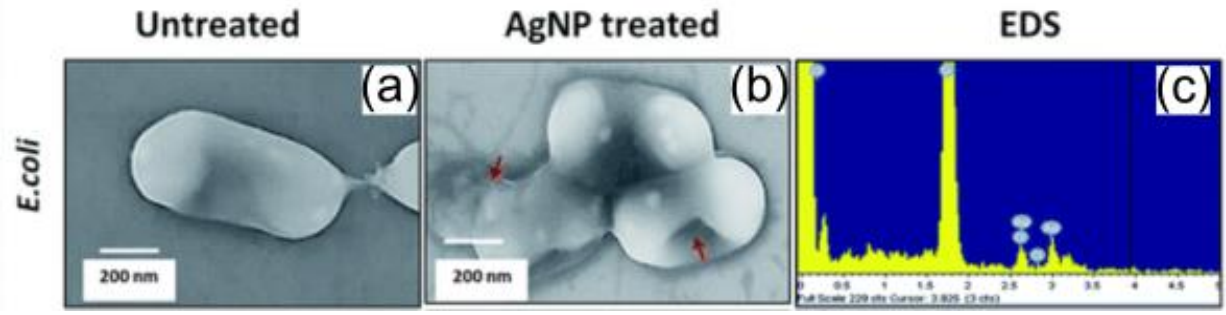

Figure 4.9 a) SEM image of untreated *E. coli* b) SEM image treated *E. coli* with Ag NPs, c) EDS analysis confirmed the presence of Ag NPs on the surface of bacteria [15]

To gain more information about the inner structures of the bacteria, or their interaction with nanoparticles, TEM imaging has been used rather frequently. A beam of electron transmits through a sample and the interaction between electrons and sample atoms reveals the information of the sample such as crystal structure, the details of internal structure. In this method, sample should be very thin to transmit electrons, making sample preparation very challenging. Figure 4.10 shows an example of TEM image of untreated (a) and treated *E. coli* with MgZnO NPs (b) [51].

An important limitation of the methods described so far is the absence of chemical information at the level of the functional groups, which is necessary to identify the mode of actions of the treatments.

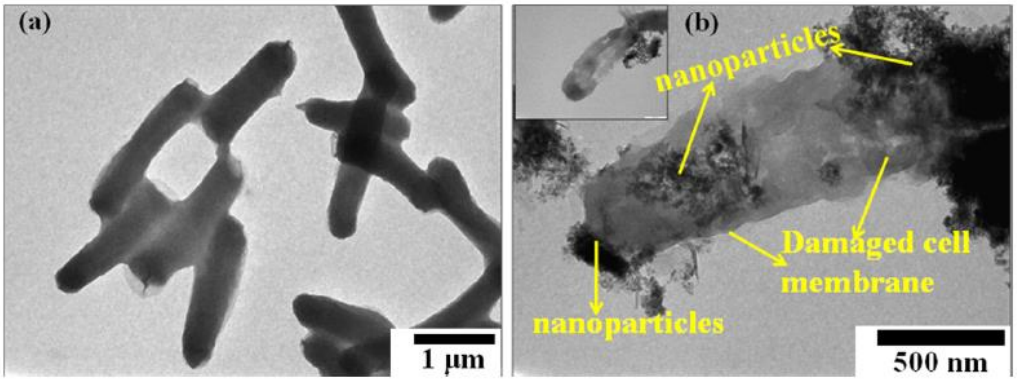

Figure 4.10 TEM image of a) untreated *E. coli* and b) treated *E.coli* with MgZnO NPs [16]

4.6.6 FTIR

IR spectroscopy has been used to understand the antimicrobial activity of NPs treatments. Using an attenuated total reflectance (ATR) configuration for FTIR, the evanescent wave created at the

surface of the prism allows to selectively probe the sample in contact with the prism, limiting the contribution of water in the signature collected [21, 156].

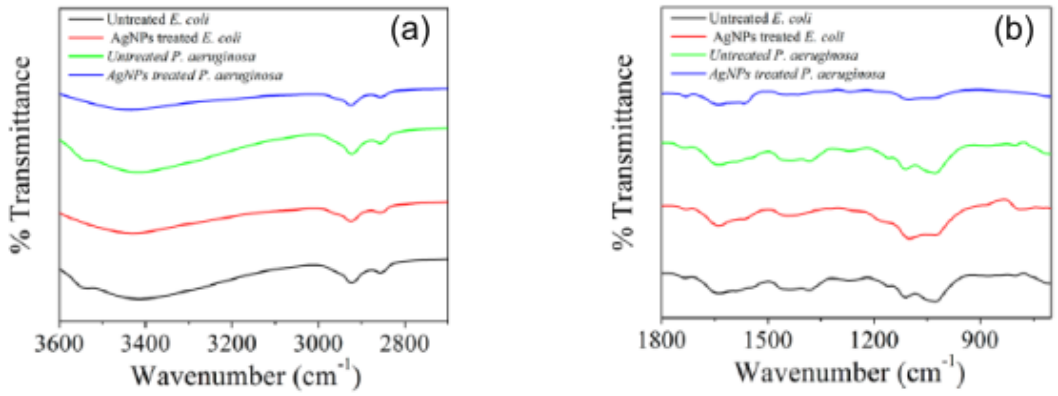

Figure 4.11 FTIR transmission spectra of untreated and treated *E.coli* and *P. aeruginosa* for two different range of wavenumbers a) 3600-2700 cm^{-1}, b)1800-700 cm^{-1}[128].

FTIR spectra were shown to be sensitive to binding of the NPs to the cell surface and to changes in cell membranes [128]. Comparing the IR signatures of untreated and treated *E. coli* and *P. aeruginosa* in Figure 4.11, peak shifts and reduction in band intensity can be observed. For instance, the peak at 3555 cm^{-1} in untreated *E. coli* disappears after the Ag NPs treatment, and the intensity of methyl group stretching at 2926 and 2851 cm^{-1} is diminished for treated *E. coli.* These peaks have been related to the fatty acids in the cell membrane, suggesting a transformation of *E. coli* upon treatment [128, 157]. Amide I and amide II bands were affected, which also suggest changes in the protein structure of the cell wall – likely due to the lysis of the cell membrane [128].

Furthermore, the interaction between nanoparticles and cells depends on nanoparticle-protein and nanoparticle-macro-molecules interactions. Proteins may be in the form of structural proteins

like tubulin and actin or proteins responsible for cell signaling like hormones or enzymes. Nanoparticle- protein interactions may modify the conformation of the proteins [158]. For example, polystyrene and gold NPs interaction with cells results in decrease the α-helix and increase β-turn structures [159]. Thus, it is crucial to understand how nanoparticles interact with proteins, and how they interrupt protein conformation, which FTIR can provide.

Although all these methods have been proven as useful methods in determining the antibacterial activity of nanoparticles, they have some limitations to define the mode of actions of treatments. In plate counting technique, counting colonies only provides a superficial insight into the effect of the treatment. Fluorescence spectroscopy suffers from photobleaching and the dye can itself have an effect on the cell systems. Electron microscopy, as mentioned earlier, requires to fix and dry the cells and to deposit a conductive top coating, which may disrupt the natural state of the system. These high-resolution techniques are costly and time consuming. FTIR offers the chemical insight missing from the other methods but suffers low spatial resolution due to the optical diffraction limit. The microscale resolution of FTIR cannot resolve single bacteria and thus the information recorded corresponds to an average view of the interaction of nanoparticles and cells, without the ability to access local cell response.

Overall, none of these approaches is currently suitable to explore the local response of individual cells to NPs treatments. To overcome this limitation, we implemented AFM-IR measurements for cell analysis. We detail our work below.

4.7 AFM-IR measurements

The sub-100nm lateral resolution of AFM-IR is very applicable for cell studies. In addition, the nanomechanical detection of AFM-IR is well suited to monitor the photothermal response of organic materials, and by extension, of cells and bacteria. In principle, infrared spectra of a cell can be used to infer the healthy and stressed status of a cell. With AFM-IR, the variation of chemical composition of cell wall at nanoscale before and after treatment can be detected [160]. AFM-IR can be used to collect the IR fingerprint of untreated and treated cells to detect changes in chemistry induced by the cell-nanoparticle interaction.

Nanoscale infrared spectroscopy was performed on a nanoIR2 (Anasys instrument) system. The IR source available for this measurement (Daylight solution QCL laser) emits in the range of 1500-1800 cm^{-1}. A gold coated Si n-type cantilever was with free flexural resonance in the 11-19 kHz range and force constant of 0.1-0.6 N/m was used for the measurements. The second contact resonance of the cantilever was selected (181 kHz) for imaging and IR mapping. Hence, the laser source generated 150 ns pulses with a repetition rate of 180 kHz at 3.45 mW. AFM-IR spectra were obtained by co-average of 256 scans. AFM-IR maps were obtained with a scan rate of 0.1 Hz and 512 by 512points at illumination wavelength. In our AFM-IR measurement, we first acquired AFM height images in contact mode to find the best region and preferably a single bacterium before carrying out the IR measurements.

4.8 Sample preparation

4.8.1 Nanoparticle treatment preparation

As discussed in section 4.6, there is a need for a novel nanoparticle treatment to oppose the copper-resistant *X. perforans* strain and also does not cause copper contamination in the environment. To achieve this aim, we consider here a multivalent silica core-shell nanoparticle with embedded copper multivalent ions (Cu^{0+}, Cu^{1+}, Cu^{2+}) and quaternary ammonium (quat) designed and produced by Dr. Santra's group with the name of local systemic pesticide (LSP) particle whose schematic is shown in Figure 4.12 .

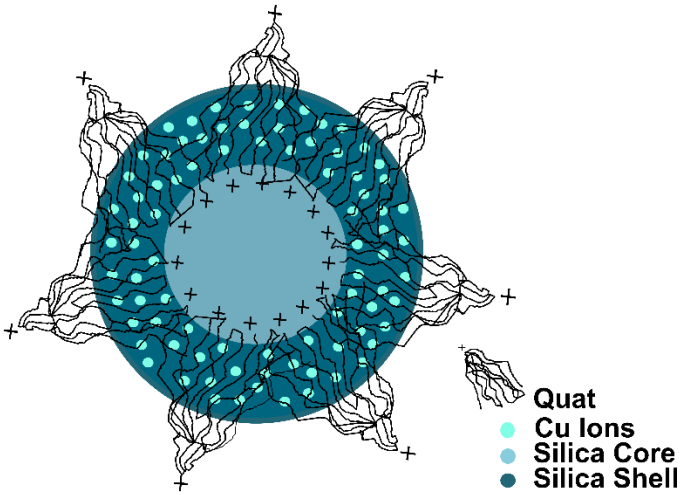

Figure.4.12 Schematic of LSP nanoparticles including silica core-shell with 2 active ingredients, multivalent Cu^{0+}, Cu^{1+}, Cu^{2+}, and quat. *Courtesy of Briana Lee at UCF.*

This LSP particle was designed to be non-phytotoxic with the aim to seek EPA approval if field applications were to show interesting results. LSP particles were designed with a Silica nanoparticles core with diameter of about 35-50 nm synthesized by Strober sol-gel method

[161] . A silica shell was added [161] to load the multivalent copper. In the last step, the quaternary ammonium was coated over the silica core-shell to create a gel-like formulation [162].

We tested here the response of the cells to the LSP treatment with the both active components of copper and quaternary ammonium (2000 ppm copper and 500 ppm quaternary ammonium). The solvent of the LSP particles is DI water.

4.8.2 Bacteria sample preparation

Bacterial sample preparation starts with a culture of *X. perforans* at 27° C between 18-22 h. Then the bacteria incubate with the LSP solution (2000 ppm Cu: 500 ppm quat) in growth medium for 30 min in a 27° C incubator. We aliquot 1:1 treatment with bacteria. After 30 min, the bacteria are harvested and washed 3 times by removing supernatant. Then the bacteria are centrifuged at 3000 rpm for 3 min. The supernatant is discarded each time and the bacteria pellet is resuspended by adding up to 1 mL of dH_2O. This washing protocol is repeated 3 times.

4.8.3 Substrate preparation

For AFM-IR measurement, an IR transparent material is used as the substrate in order to prevent any interference with the sample spectra. Calcium fluoride (CaF_2) was chosen here because it provides the lowest background signal [163].

CaF_2 substrates were prepared by rinsing with ethanol and dH_2O respectively and drying by blowing compressed air. Next, 2 µL of bacteria solutions was placed onto the CaF_2 substrate by drop casting method. The sample was air dried in a close container for about 1 h.

4.9 Results and discussion

From the preliminary data, we confirmed treatment killing efficacy via minimum inhibitory concentration (MIC). We investigated the effect of LSP on *X. perforans* at nanoscale with AFM-IR (Figure 4.13). As shown in Figure 4.13. b the averaged spectra recorded for untreated *X. perforans* indicates the amide I and amide II signatures at 1648 and 1548 cm^{-1}, respectively [160]. In contrast, the treated *X. perforans* exhibited amide I and II peaks at 1660 and 1557 cm^{-1}, respectively. These amides I and II peak shifts indicate the transition of the protein conformation from α-helical to β-sheets and β-turn like structures which is coming from the breakage of H bonds due to interaction with nanoparticles which ends in cell wall damage [12, 160]. The data for the amide I band was analyzed and evaluated statistically, as shown in Figure 4.14. ANOVA analysis confirms that the shift is statistically significant ($p<0.5$). The degradation or lysis of the peptidoglycan layer or cell wall could be responsible for the alteration in the protein structure.

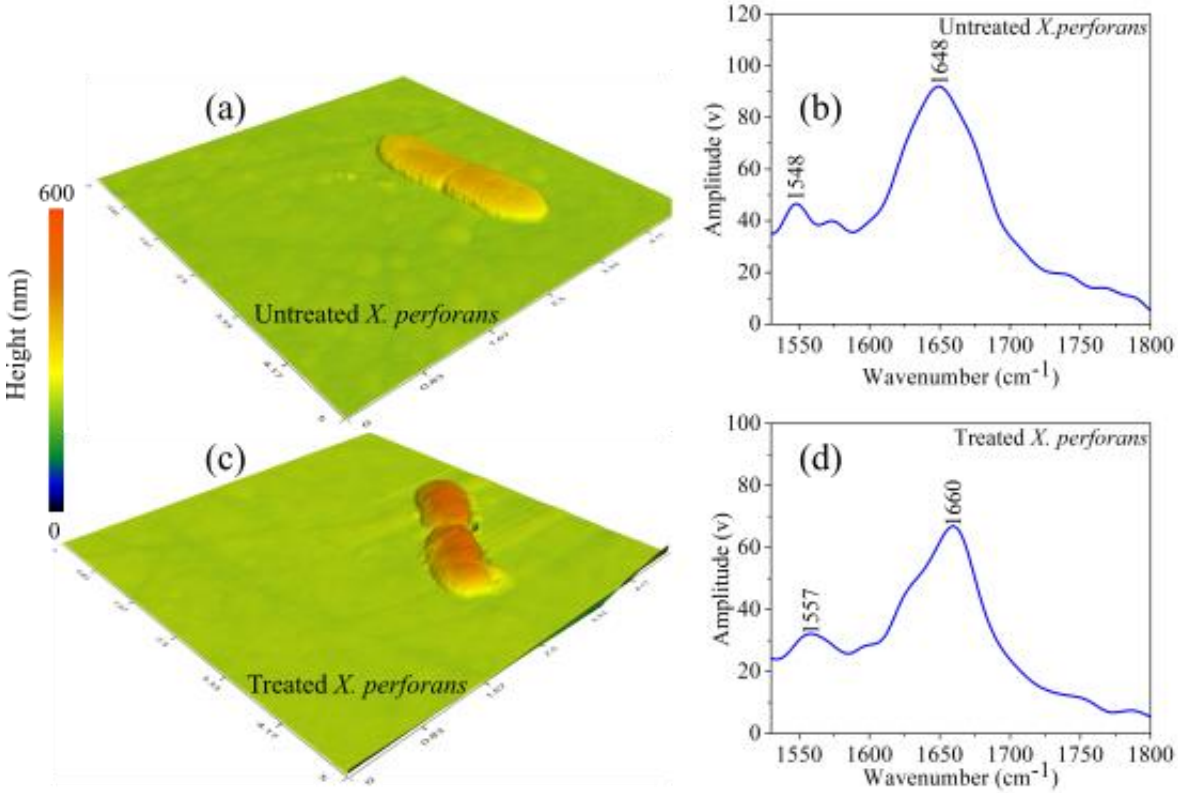

Figure 4.13 (a) AFM height image of untreated *X. perforans* (b) the AFM-IR spectrum of untreated *X. perforans* at the center of bacteria, which shows amide I and II (c) AFM height image of treated *X. perforans*, (d)) the AFM-IR spectrum of untreated *X. perforans* at the center of bacteria, which shows that amide I is affected by the treatment.

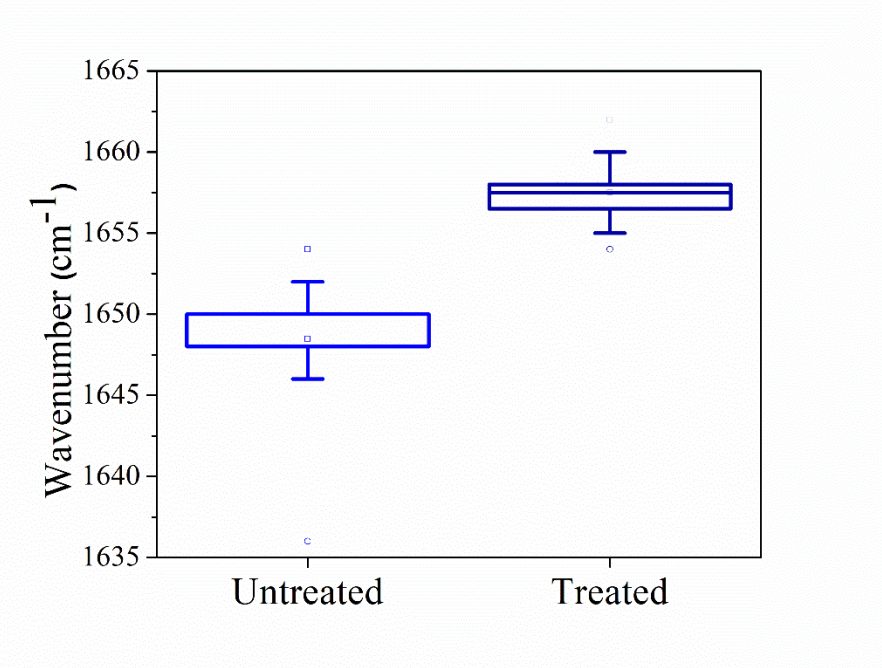

Figure 4.14 Average position of amide I band in treated and untreated *X. perforans* bacterial cell wall spectra measured by AFM-IR. The whiskers indicate the standard deviation, and the line in the middle is the mean. The amide I band peak shifts from about 1648 cm^{-1} (in untreated bacteria) to 1660 cm^{-1} (in treated bacteria with LSP 2 active).

Figure 4. 15 a, b shows the AFM height (and d, e corresponding deflection) images of untreated (a-c) and treated (d-f) *X. perforans*. The chemical maps were acquired at 1650 cm^{-1}. The signal

from the untreated cell is stronger than in the treated cell, in agreement with the shift observed in the AFM-IR spectra discussed above.

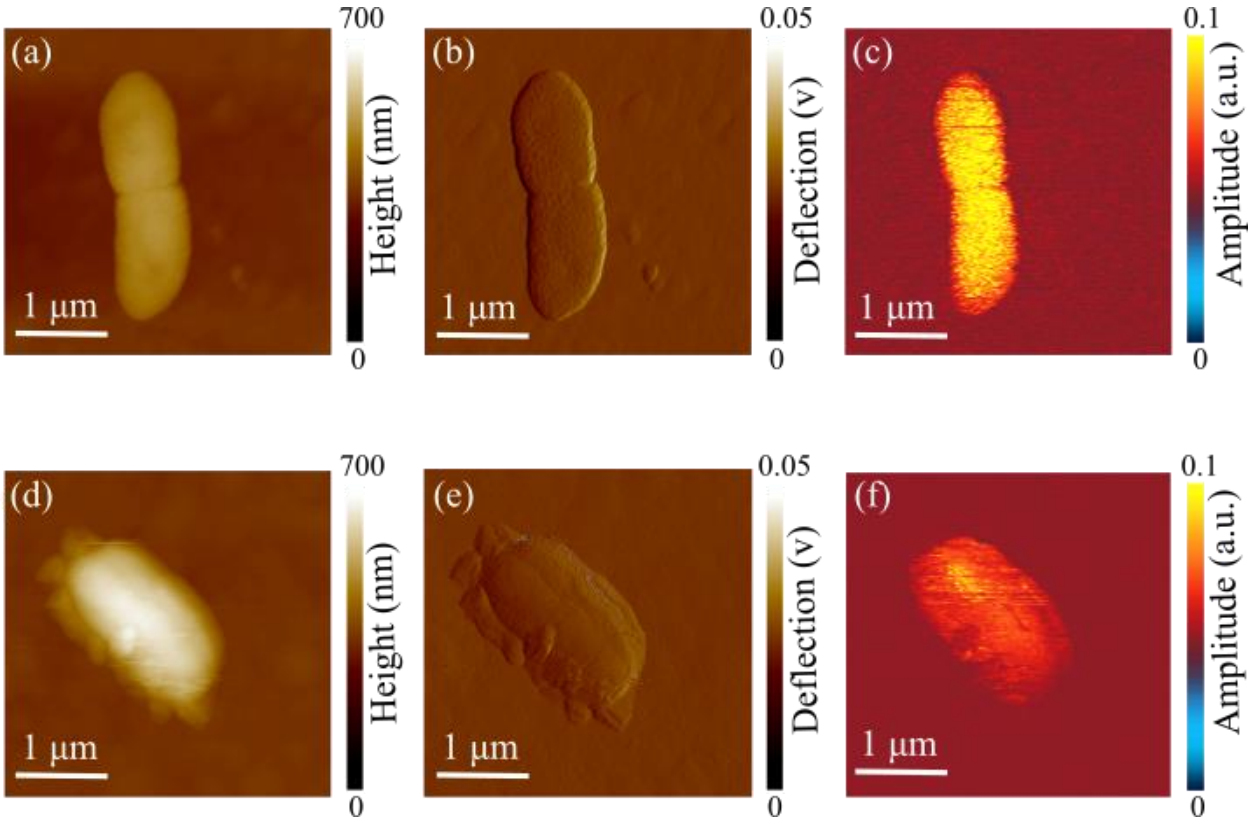

Figure 4.15 (a) AFM height image, (b) deflection image (c) AFM-IR amplitude map at 1650 cm^{-1} of untreated *X. perforans* and (d) AFM height image, (e) deflection image, (f) AFM-IR amplitude map at 1650 cm^{-1} of treated *X. perforans* with LSP particles.

Next, we investigate surface roughness for the cells, shown in Figure.4.16. Surface roughness is one of the parameters used to quantify changes due to environmental effects [164]. The comparison of the surface roughness for treated and untreated bacteria indicates higher roughness for treated bacteria which confirms that LSP particles damage the cell wall membrane of *X. perforans*.

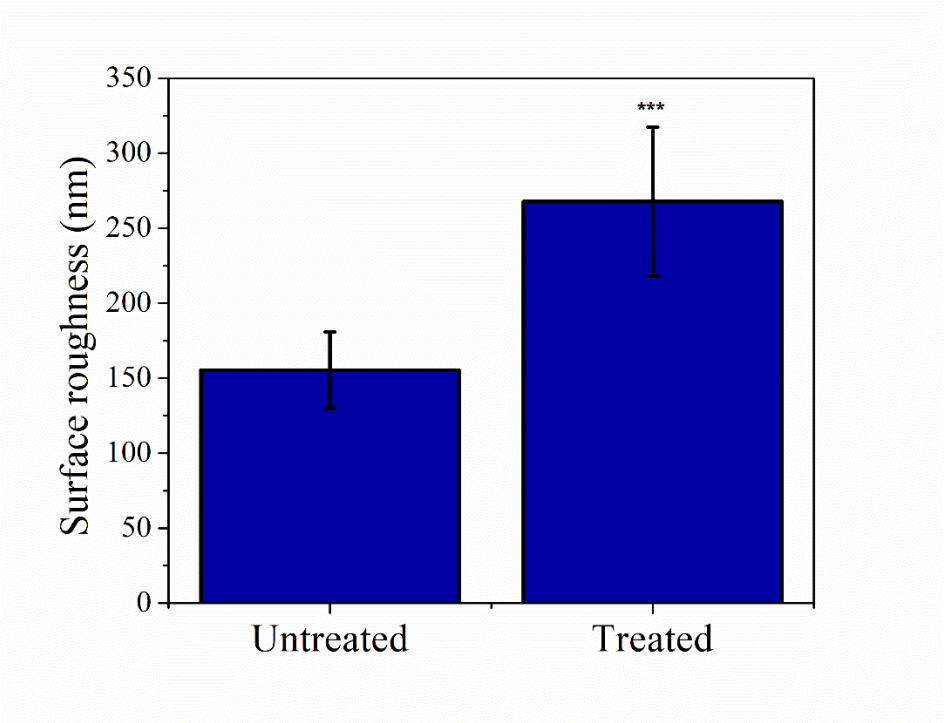

Figure 4.16 Surface roughness for treated and untreated *X. perforans*. Surface roughness of the bacteria cell wall is about doubles in roughness with LSP treatment ($p<0.001$).

4.10 Conclusion

Here we have shown that AFM-IR has great potential to explore new fundamental processes in nanobiotechnology, such as the study of bacterial cell wall response to individual nanoparticles. We demonstrated that bacterial cell wall proteins undergo conformational change after treatment with LSP. These results strengthen our understanding about the nanomaterial toxicity to be used in plant for pathogen inhibition. Since toxicity of nanoparticles is related to the size, shape, and surface chemistry of nanoparticles, this technique enables us to optimize the nanoparticle characteristics for their safe use in food production or other future biomedical applications

CHAPTER 5 CONCLUSION

Studying light-matter interaction at the molecular level is critical to accelerate our understanding of important life science processes. Chemical speciation has successfully been implemented to Atomic Force Microscopy (AFM) measurements. By exciting the material with infrared light and using the AFM cantilever it is possible to monitor the photothermal expansion resulting from the vibrational modes excited in the material.

In this work, we have expanded the capabilities of AFM-IR to probe local field enhancement and CD in plasmonic structure. We have demonstrated the proof-of-concept that chiral biomolecules vCD can be detected from this measurement. Specifically, we show the benefit of using a cavity-coupled plasmonic structures. Chiral biomolecules with absorption and vibrational circular dichroism signature overlapping with the absorption of the cavity-coupled plasmonic structure are identified for this measurement. Other molecules could be characterized by tuning the properties of the substrate. We show that the substrate responds to both linearly and polarized excitation, and that the response is dependent on the orientation of the array of structure with respect to the incident light. For circular polarization, the field distribution clearly depends on the left-handedness and right-handedness of the incident polarization. We demonstrate that using the “hot spots” of the cavity coupled plasmonic structures are significant and offer great potential for characterizing the chirality of molecules distributed with lower density, which will be addressed in future studies.

In our second study we continue to exploit the potential of AFM-IR to address important and timely questions in life science. The response of individual bacterial cell to NP-based antibacterial treatments is explored. In recent years, there has been growing interest in how nanoparticles interact with living systems. The fundamental molecular mechanism of antibacterial activity of nanoparticles is not yet well understood. The state of the art still suffers from limitations, such as the lack of technologies in accessing changes in chemical and functional properties at the single cell level. Although high spatial resolution microscope is becoming popular for the bacterial study, AFM-IR has not been considered to study mechanisms of bacterial response to treatments. We investigated the response of *X. perforans* to LSP copper-based particles. A significant change in Amide I band (1650 cm^{-1}) was revealed accompanied by a change in surface roughness of the cells. These indicate that LSP acts to modify the membrane of the cell for killing.

Overall the work presented here provides some insight on the new fundamental knowledge that is accessible with nanoscale characterization. Future studies will be required to advance this knowledge.

LIST OF REFERENCES

1. Drake, S., *Telescopes, tides, and tactics : a Galilean dialogie about the "Starry messenger" and systems of the world*. 1983, Chicago; London: University of Chicago.
2. Gest, H., *The discovery of microorganisms by Robert Hooke and Antoni van Leeuwenhoek, Fellows of The Royal Society.* 2004. **58**(2): p. 187-201.
3. Scheuring, S., et al., *Nanodissection and high-resolution imaging of the Rhodopseudomonas viridis photosynthetic core complex in native membranes by AFM.* Proceedings of the National Academy of Sciences, 2003. **100**(4): p. 1690.
4. Hansma, H.G., et al., *Reproducible Imaging and Dissection of Plasmid DNA Under Liquid with the Atomic Force Microscope.* Science, 1992. **256**(5060): p. 1180.
5. Thalhammer, S., et al., *The Atomic Force Microscope as a New Microdissecting Tool for the Generation of Genetic Probes.* Journal of Structural Biology, 1997. **119**(2): p. 232-237.
6. Hansma, H.G., *SURFACE BIOLOGY OF DNA BY ATOMIC FORCE MICROSCOPY.* Annual Review of Physical Chemistry, 2001. **52**(1): p. 71-92.
7. Hansma, H.G., K. Kasuya, and E. Oroudjev, *Atomic force microscopy imaging and pulling of nucleic acids.* Current Opinion in Structural Biology, 2004. **14**(3): p. 380-385.
8. Fotiadis, D., et al., *Imaging and manipulation of biological structures with the AFM.* Micron, 2002. **33**(4): p. 385-397.
9. Weisenhorn, A.L., et al., *Deformation and height anomaly of soft surfaces studied with an AFM.* Nanotechnology, 1993. **4**(2): p. 106.
10. Dazzi, A. and C.B. Prater, *AFM-IR: Technology and Applications in Nanoscale Infrared Spectroscopy and Chemical Imaging.* Chemical Reviews, 2017. **117**(7): p. 5146-5173.
11. Dazzi, A., et al., *Local infrared microspectroscopy with subwavelength spatial resolution with an atomic force microscope tip used as a photothermal sensor.* Optics Letters, 2005. **30**(18): p. 2388-2390.
12. Ruggeri, F.S., et al., *Infrared nanospectroscopy characterization of oligomeric and fibrillar aggregates during amyloid formation.* Nature Communications, 2015. **6**: p. 7831.
13. Cooley, R.B., D.J. Arp, and P.A. Karplus, *Evolutionary Origin of a Secondary Structure: π-Helices as Cryptic but Widespread Insertional Variations of α-Helices That Enhance Protein Functionality.* Journal of Molecular Biology, 2010. **404**(2): p. 232-246.
14. Gopinath, S.C.B., et al., *Bacterial detection: From microscope to smartphone.* Biosensors and Bioelectronics, 2014. **60**: p. 332-342.
15. Verma, S.K., et al., *Mechanistic insight into the rapid one-step facile biofabrication of antibacterial silver nanoparticles from bacterial release and their biogenicity and concentration-dependent in vitro cytotoxicity to colon cells.* RSC Advances, 2017. **7**(64): p. 40034-40045.
16. Gupta, J. and D. Bahadur, *Defect-Mediated Reactive Oxygen Species Generation in Mg-Substituted ZnO Nanoparticles: Efficient Nanomaterials for Bacterial Inhibition and Cancer Therapy.* ACS Omega, 2018. **3**(3): p. 2956-2965.
17. Palmer, R.J. and C. Sternberg, *Modern microscopy in biofilm research: confocal microscopy and other approaches.* Current Opinion in Biotechnology, 1999. **10**(3): p. 263-268.
18. Sakurai, J.J. and J. Napolitano, *Modern Quantum Mechanics*. 2 ed. 2017, Cambridge: Cambridge University Press.

19. Bransden, B.H. and C.J. Joachain, *Introduction to Quantum Mechanics*. 1989: Longman Scientific & Technical.
20. Cohen-Tannoudji, C., J. Dupont-Roc, and G. Grynberg, *Photons and Atoms: Introduction to Quantum Electrodynamics*. 1989: Wiley.
21. Thompson, J.M., *Infrared Spectrometry.* 2018.
22. https://www.thorlabs.com/images/Tabimages/Polarization_Handedness_Tutorial.pdf. Available from: https://www.thorlabs.com/images/Tabimages/Polarization_Handedness_Tutorial.pdf.
23. Rius, G., et al., *Properties and applications of carbon nanofibers for atomic force microscopy*. 2015. 571-574.
24. Haugstad, G., *Atomic Force Microscopy, understanding basic modes and advanced applications.* 2012.
25. Doktycz, M.J., et al., *AFM imaging of bacteria in liquid media immobilized on gelatin coated mica surfaces.* Ultramicroscopy, 2003. **97**(1): p. 209-216.
26. Cross, S.E., et al., *AFM-based analysis of human metastatic cancer cells.* Nanotechnology, 2008. **19**(38): p. 384003.
27. Bieletzki, M., et al., *Topography and work function measurements of thin MgO(001) films on Ag(001) by nc-AFM and KPFM.* Physical Chemistry Chemical Physics, 2010. **12**(13): p. 3203-3209.
28. Van Bael, M.J., et al., *Magnetic properties of submicron Co islands and their use as artificial pinning centers.* Physical Review B, 1999. **59**(22): p. 14674-14679.
29. Frone, A.N., et al., *Morphology and thermal properties of PLA–cellulose nanofibers composites.* Carbohydrate Polymers, 2013. **91**(1): p. 377-384.
30. Bridger, P.M., et al., *Measurement of induced surface charges, contact potentials, and surface states in GaN by electric force microscopy.* Applied Physics Letters, 1999. **74**(23): p. 3522-3524.
31. Sugawara, Y., et al., *Simultaneous Observation of Atomically Resolved AFM/STM Images of a Graphite Surface.* Japanese Journal of Applied Physics, 1990. **29**(Part 2, No. 1): p. L157-L159.
32. Yamamoto, S.-i., et al., *Identification of Materials using Direct Force Modulation Technique with Magnetic AFM Cantilever.* Japanese Journal of Applied Physics, 1997. **36**(Part 1, No. 6B): p. 3868-3871.
33. Lekka, M. and P. Laidler, *Applicability of AFM in cancer detection.* Nature Nanotechnology, 2009. **4**: p. 72.
34. Muller, D.J., *AFM: A Nanotool in Membrane Biology.* Biochemistry, 2008. **47**(31): p. 7986-7998.
35. Alonso, J.L. and W.H. Goldmann, *Feeling the forces: atomic force microscopy in cell biology.* Life Sciences, 2003. **72**(23): p. 2553-2560.
36. Goldsbury, C.S., S. Scheuring, and L. Kreplak, *Introduction to Atomic Force Microscopy (AFM) in Biology.* Current Protocols in Protein Science, 2009. **58**(1): p. 17.7.1-17.7.19.
37. Oesterhelt, F., M. Rief, and H.E. Gaub, *Single molecule force spectroscopy by AFM indicates helical structure of poly(ethylene-glycol) in water.* New Journal of Physics, 1999. **1**: p. 6-6.
38. Shirakashi, J.-i., et al., *Surface Modification of Niobium (Nb) by Atomic Force Microscope (AFM) Nano-Oxidation Process.* Japanese Journal of Applied Physics, 1996. **35**(Part 2, No. 11B): p. L1524-L1527.
39. Bordag, M., et al., *Shear Stress Measurements on InAs Nanowires by AFM Manipulation.* Small, 2007. **3**(8): p. 1398-1401.
40. Kassies, R., et al., *Combined AFM and confocal fluorescence microscope for applications in bio-nanotechnology.* Journal of Microscopy, 2005. **217**(1): p. 109-116.

41. Zou, Q., et al., *CONTROL ISSUES IN HIGH-SPEED AFM FOR BIOLOGICAL APPLICATIONS: COLLAGEN IMAGING EXAMPLE.* Asian Journal of Control, 2004. **6**(2): p. 164-178.
42. Radmacher, M., *Measuring the elastic properties of biological samples with the AFM.* IEEE Engineering in Medicine and Biology Magazine, 1997. **16**(2): p. 47-57.
43. Margenau, H., *Van der waals forces.* Reviews of Modern Physics, 1939. **11**(1): p. 1-35.
44. Israelachvili, J.N., *Intermolecular and Surface Forces.* 1991(2nd edition): p. p.450.
45. Yuya, P.A., D.C. Hurley, and J.A. Turner, *Contact-resonance atomic force microscopy for viscoelasticity.* Journal of Applied Physics, 2008. **104**(7): p. 074916.
46. Lee, C., et al., *Measurement of the Elastic Properties and Intrinsic Strength of Monolayer Graphene.* Science, 2008. **321**(5887): p. 385.
47. Jiang, T. and Y. Zhu, *Measuring graphene adhesion using atomic force microscopy with a microsphere tip.* Nanoscale, 2015. **7**(24): p. 10760-10766.
48. Jee, A.-Y. and M. Lee, *Comparative analysis on the nanoindentation of polymers using atomic force microscopy.* Polymer Testing, 2010. **29**(1): p. 95-99.
49. Smolyakov, G., et al., *AFM PeakForce QNM mode: Evidencing nanometre-scale mechanical properties of chitin-silica hybrid nanocomposites.* Carbohydrate Polymers, 2016. **151**: p. 373-380.
50. Tobias, H.J., et al., *Chemical Analysis of Diesel Engine Nanoparticles Using a Nano-DMA/Thermal Desorption Particle Beam Mass Spectrometer.* Environmental Science & Technology, 2001. **35**(11): p. 2233-2243.
51. Hammiche, A., et al., *Photothermal FT-IR Spectroscopy: A Step Towards FT-IR Microscopy at a Resolution Better Than the Diffraction Limit.* Applied Spectroscopy, 1999. **53**(7): p. 810-815.
52. Anderson, M.S., *Infrared Spectroscopy with an Atomic Force Microscope.* Applied Spectroscopy, 2000. **54**(3): p. 349-352.
53. Dazzi, A., et al., *AFM-IR: Combining Atomic Force Microscopy and Infrared Spectroscopy for Nanoscale Chemical Characterization.* Applied Spectroscopy, 2012. **66**(12): p. 1365-1384.
54. Clède, S., et al., *Detection of an estrogen derivative in two breast cancer cell lines using a single core multimodal probe for imaging (SCoMPI) imaged by a panel of luminescent and vibrational techniques.* Analyst, 2013. **138**(19): p. 5627-5638.
55. Paluszkiewicz, C., et al., *Differentiation of protein secondary structure in clear and opaque human lenses: AFM – IR studies.* Journal of Pharmaceutical and Biomedical Analysis, 2017. **139**: p. 125-132.
56. Aksyuk, V., et al., *Near-field asymmetries in plasmonic resonators.* Nanoscale, 2015. **7**(8): p. 3634-3644.
57. Chae, J., B. Lahiri, and A. Centrone, *Engineering Near-Field SEIRA Enhancements in Plasmonic Resonators.* ACS Photonics, 2016. **3**(1): p. 87-95.
58. Chae, J., et al., *Metal-dielectric-metal resonators with deep subwavelength dielectric layers increase the near-field SEIRA enhancement.* Optics Express, 2015. **23**(20): p. 25912-25922.
59. Katzenmeyer, A.M., et al., *Nanoscale Imaging and Spectroscopy of Plasmonic Modes with the PTIR Technique.* Advanced Optical Materials, 2014. **2**(8): p. 718-722.
60. Lahiri, B., et al., *Nanoscale Imaging of Plasmonic Hot Spots and Dark Modes with the Photothermal-Induced Resonance Technique.* Nano Letters, 2013. **13**(7): p. 3218-3224.
61. Felts, J.R., et al., *Near-field infrared absorption of plasmonic semiconductor microparticles studied using atomic force microscope infrared spectroscopy.* Applied Physics Letters, 2013. **102**(15): p. 152110.

62. Dazzi, A., F. Glotin, and R. Carminati, *Theory of infrared nanospectroscopy by photothermal induced resonance.* Journal of Applied Physics, 2010. **107**(12): p. 124519.
63. Kumar, J., K.G. Thomas, and L.M. Liz-Marzan, *Nanoscale chirality in metal and semiconductor nanoparticles.* Chemical Communications, 2016. **52**(85): p. 12555-12569.
64. Nguyen, L.A., H. He, and C. Pham-Huy, *Chiral drugs: an overview.* International journal of biomedical science : IJBS, 2006. **2**(2): p. 85-100.
65. N. Berova, K.N., R. Woody, *Circular Dichroism principles and applications*. 2000, Canada: WILEY-VCH.
66. Amabilino, D., *chirality at the nanoscale*. 2009: Wiley.
67. V.K. Valev, J.J.B., C. Sibilia, T. Verbist, *Chirality and chiroptical effects in plasmonic nanostructures: Fundamnetals, recent progress, and outlook.* Adv. Mater. , 2013. **25**: p. 2517-2534.
68. Rentsch, K.M., *The importance of stereoselective determination of drugs in the clinical laboratory.* Journal of Biochemical and Biophysical Methods, 2002. **54**(1): p. 1-9.
69. Pham-Huy, C., et al., *Enantioselective high-performance liquid chromatography determination of methadone enantiomers and its major metabolite in human biological fluids using a new derivatized cyclodextrin-bonded phase.* Journal of Chromatography B: Biomedical Sciences and Applications, 1997. **700**(1): p. 155-163.
70. Olsen, G.D., et al., *Clinical eftects and pharmacokinetics of racemic methadone and its optical isomers.* Clinical Pharmacology & Therapeutics, 1977. **21**(2): p. 147-157.
71. Holm, K.M.D. and K. Linnet, *Determination of the unbound fraction of R- and S-methadone in human brain.* International Journal of Legal Medicine, 2016. **130**(6): p. 1519-1526.
72. Barrett, A.M. and V.A. Cullum, *The biological properties of the optical isomers of propranolol and their effects on cardiac arrhythmias.* British Journal of Pharmacology, 1968. **34**(1): p. 43-55.
73. Cheng, H., et al., *Pharmacokinetics and Bioinversion of Ibuprofen Enantiomers in Humans.* Pharmaceutical Research, 1994. **11**(6): p. 824-830.
74. Marzo, A. and E. Heftmann, *Enantioselective analytical methods in pharmacokinetics with specific reference to genetic polymorphic metabolism.* Journal of Biochemical and Biophysical Methods, 2002. **54**(1): p. 57-70.
75. https://www.fda.gov/drugs/guidancecomplianceregulatoryinformation/guidances/ucm122883.htm, 2018.
76. Labuta, J., et al., *NMR spectroscopic detection of chirality and enantiopurity in referenced systems without formation of diastereomers.* Nature Communications, 2013. **4**: p. 2188.
77. Luy, B., *Distinction of enantiomers by NMR spectroscopy using chiral orienting media.* Journal of the Indian Institute of Science, 2010. **90**(1): p. 119-132.
78. Wenzel, T.J. and C.D. Chisholm, *Using NMR spectroscopic methods to determine enantiomeric purity and assign absolute stereochemistry.* Progress in Nuclear Magnetic Resonance Spectroscopy, 2011. **59**(1): p. 1-63.
79. Chen, M., et al., *Comparative Analysis of Proline Enantiomer in Chiral Recognition of Biological Macromolecule in Immunoassay.* Electroanalysis, 2009. **21**(21): p. 2339-2344.
80. Trojanowicz and M. Kaniewska, *Chiral Biosensors and Immunosensors*. 2011.
81. Izake, E.L., *Chiral discrimination and enantioselective analysis of drugs: An overview.* Journal of Pharmaceutical Sciences, 2007. **96**(7): p. 1659-1676.

82. Miller, H., et al., *Single-molecule techniques in biophysics: a review of the progress in methods and applications.* Reports on Progress in Physics, 2017. **81**(2): p. 024601.
83. Moerner, W.E. and D.P. Fromm, *Methods of single-molecule fluorescence spectroscopy and microscopy.* Review of Scientific Instruments, 2003. **74**(8): p. 3597-3619.
84. Wang, X. and Z. Tang, *Circular Dichroism Studies on Plasmonic Nanostructures.* Small, 2016: p. n/a-n/a.
85. Sreerama, N., S.Y. Venyaminov, and R.W. Woody, *Estimation of Protein Secondary Structure from Circular Dichroism Spectra: Inclusion of Denatured Proteins with Native Proteins in the Analysis.* Analytical Biochemistry, 2000. **287**(2): p. 243-251.
86. Keiderling, T.A., *Protein and peptide secondary structure and conformational determination with vibrational circular dichroism.* Current Opinion in Chemical Biology, 2002. **6**(5): p. 682-688.
87. Kelly, S.M., T.J. Jess, and N.C. Price, *How to study proteins by circular dichroism.* Biochimica et Biophysica Acta (BBA) - Proteins and Proteomics, 2005. **1751**(2): p. 119-139.
88. Mason, S.F., *Molecular optical activity and the chiral discriminations*. 1982: Cambridge University Press, New York.
89. Lieberman, I., et al., *Plasmon-Resonance-Enhanced Absorption and Circular Dichroism.* Angewandte Chemie International Edition, 2008. **47**(26): p. 4855-4857.
90. Tang, Y., T.A. Cook, and A.E. Cohen, *Limits on Fluorescence Detected Circular Dichroism of Single Helicene Molecules.* The Journal of Physical Chemistry A, 2009. **113**(22): p. 6213-6216.
91. Dazzi, A., et al., *AFM–IR: Combining Atomic Force Microscopy and Infrared Spectroscopy for Nanoscale Chemical Characterization.* Applied Spectroscopy, 2012. **66**(12): p. 1365-1384.
92. Jatschka, J., et al., *Propagating and localized surface plasmon resonance sensing — A critical comparison based on measurements and theory.* Sensing and Bio-Sensing Research, 2016. **7**: p. 62-70.
93. Hartstein, A., J.R. Kirtley, and J.C. Tsang, *Enhancement of the Infrared Absorption from Molecular Monolayers with Thin Metal Overlayers.* Physical Review Letters, 1980. **45**(3): p. 201-204.
94. Kundu, J., et al., *Surface enhanced infrared absorption (SEIRA) spectroscopy on nanoshell aggregate substrates.* Chemical Physics Letters, 2008. **452**(1): p. 115-119.
95. Schäferling, M., et al., *Tailoring Enhanced Optical Chirality: Design Principles for Chiral Plasmonic Nanostructures.* Physical Review X, 2012. **2**(3): p. 031010.
96. Hentschel, M., et al., *Three-Dimensional Chiral Plasmonic Oligomers.* Nano Letters, 2012. **12**(5): p. 2542-2547.
97. Vázquez-Guardado, A. and D. Chanda, *Superchiral Light Generation on Degenerate Achiral Surfaces.* Physical Review Letters, 2018. **120**(13): p. 137601.
98. García-Guirado, J., et al., *Enantiomer-Selective Molecular Sensing Using Racemic Nanoplasmonic Arrays.* Nano Letters, 2018. **18**(10): p. 6279-6285.
99. Zhao, Y., et al., *Chirality detection of enantiomers using twisted optical metamaterials.* Nature Communications, 2017. **8**: p. 14180.
100. Gerard, V.A., et al., *Plasmon-induced CD response of oligonucleotide-conjugated metal nanoparticles.* Chemical Communications, 2011. **47**(26): p. 7383-7385.
101. Maoz, B.M., et al., *Amplification of Chiroptical Activity of Chiral Biomolecules by Surface Plasmons.* Nano Letters, 2013. **13**(3): p. 1203-1209.
102. HendryE, et al., *Ultrasensitive detection and characterization of biomolecules using superchiral fields.* Nat Nano, 2010. **5**(11): p. 783-787.
103. Y. Tang, A.C., *Optical chirality and its interaction with matter.* PRL, 2010. **104**.

104. Betzig, E. and J.K. Trautman, *Near-Field Optics: Microscopy, Spectroscopy, and Surface Modification Beyond the Diffraction Limit.* Science, 1992. **257**(5067): p. 189-195.
105. Khanikaev, A.B., et al., *Experimental demonstration of the microscopic origin of circular dichroism in two-dimensional metamaterials.* Nature Communications, 2016. **7**: p. 12045.
106. Chen, J., et al., *Optical nano-imaging of gate-tunable graphene plasmons.* Nature, 2012. **487**: p. 77.
107. Latour, G., et al., *Correlative nonlinear optical microscopy and infrared nanoscopy reveals collagen degradation in altered parchments.* Scientific Reports, 2016. **6**: p. 26344.
108. Nam, H.-G., et al., *Preparation of photoresist-derived carbon micropatterns by proton ion beam lithography and pyrolysis.* CARBONLETT, 2017. **24**: p. 55-61.
109. Ye, Y.-H., et al., *Localized surface plasmon polaritons in Ag⁄SiO2⁄Ag plasmonic thermal emitter.* Applied Physics Letters, 2008. **93**(3): p. 033113.
110. Lu, F., M. Jin, and M.A. Belkin, *Tip-enhanced infrared nanospectroscopy via molecular expansion force detection.* Nature Photonics, 2014. **8**: p. 307.
111. Khanikaev, A.B., et al., *Experimental demonstration of the microscopic origin of circular dichroism in two-dimensional metamaterials.* 2016. **7**: p. 12045.
112. Govorov, A.O. and H.H. Richardson, *Generating heat with metal nanoparticles.* Nano Today, 2007. **2**(1): p. 30-38.
113. Coppens, Z.J., et al., *Probing and Controlling Photothermal Heat Generation in Plasmonic Nanostructures.* Nano Letters, 2013. **13**(3): p. 1023-1028.
114. Ameling, R. and H. Giessen, *Microcavity plasmonics: strong coupling of photonic cavities and plasmons.* Laser & Photonics Reviews, 2013. **7**(2): p. 141-169.
115. Kurouski, D., *Advances of Vibrational Circular Dichroism (VCD) in bioanalytical chemistry. A review.* Analytica Chimica Acta, 2017. **990**: p. 54-66.
116. Yasui, S.C. and T.A. Keiderling, *Vibrational circular dichroism of polypeptides. 8. Poly(lysine) conformations as a function of pH in aqueous solution.* Journal of the American Chemical Society, 1986. **108**(18): p. 5576-5581.
117. Keiderling, T.A., et al., *Vibrational circular dichroism spectroscopy of selected oligopeptide conformations.* Bioorganic & Medicinal Chemistry, 1999. **7**(1): p. 133-141.
118. SPACH, M.S., *Anisotropy of Cardiac Tissue.* Journal of Cardiovascular Electrophysiology, 1999. **10**(6): p. 887-890.
119. Valderrábano, M., *Influence of anisotropic conduction properties in the propagation of the cardiac action potential.* Progress in biophysics and molecular biology, 2007. **94**(1-2): p. 144-168.
120. Allsop, D., et al., *Fluorescence Anisotropy: A Method for Early Detection of Alzheimer β-Peptide (Aβ) Aggregation.* Biochemical and Biophysical Research Communications, 2001. **285**(1): p. 58-63.
121. Knowles, T.P.J., M. Vendruscolo, and C.M. Dobson, *The amyloid state and its association with protein misfolding diseases.* Nature Reviews Molecular Cell Biology, 2014. **15**: p. 384.
122. Pierangelo, A., et al., *Ex-vivo characterization of human colon cancer by Mueller polarimetric imaging.* Optics Express, 2011. **19**(2): p. 1582-1593.
123. Furchner, A., et al., *Fast IR laser mapping ellipsometry for the study of functional organic thin films.* Analyst, 2015. **140**(6): p. 1791-1797.
124. Muller, E.A., B. Pollard, and M.B. Raschke, *Infrared Chemical Nano-Imaging: Accessing Structure, Coupling, and Dynamics on Molecular Length Scales.* The Journal of Physical Chemistry Letters, 2015. **6**(7): p. 1275-1284.

125. Hasenkampf, A., et al., *Surface-enhanced mid-infrared spectroscopy using a quantum cascade laser.* Optics Express, 2015. **23**(5): p. 5670-5680.
126. Hinrichs, K. and T. Shaykhutdinov, *Polarization-Dependent Atomic Force Microscopy–Infrared Spectroscopy (AFM-IR): Infrared Nanopolarimetric Analysis of Structure and Anisotropy of Thin Films and Surfaces.* Applied Spectroscopy, 2018. **72**(6): p. 817-832.
127. Wang, L., C. Hu, and L. Shao, *The antimicrobial activity of nanoparticles: present situation and prospects for the future.* Int J Nanomedicine, 2017. **12**: p. 1227-49.
128. Ramalingam, B., T. Parandhaman, and S.K. Das, *Antibacterial Effects of Biosynthesized Silver Nanoparticles on Surface Ultrastructure and Nanomechanical Properties of Gram-Negative Bacteria viz. Escherichia coli and Pseudomonas aeruginosa.* ACS Applied Materials & Interfaces, 2016. **8**(7): p. 4963-4976.
129. Ahmed, A., et al., *Biosensors for Whole-Cell Bacterial Detection.* Clinical Microbiology Reviews, 2014. **27**(3): p. 631.
130. Kochan, K., et al., *In vivo atomic force microscopy–infrared spectroscopy of bacteria.* Journal of The Royal Society Interface, 2018. **15**(140): p. 20180115.
131. Jones, J.B., et al., *Reclassification of the Xanthomonads Associated with Bacterial Spot Disease of Tomato and Pepper.* Systematic and Applied Microbiology, 2004. **27**(6): p. 755-762.
132. Horvath, D.M., et al., *Transgenic Resistance Confers Effective Field Level Control of Bacterial Spot Disease in Tomato.* PLOS ONE, 2012. **7**(8): p. e42036.
133. https://nifa.usda.gov/sites/default/files/resource/Tomato_Spot_Fact_Sheet_Rev1.pdf.
134. Stall, R.E., *Streptomycin resistance of the bacterial spot pathogen and control with streptomycin.* Plant Dis. Rep., 1962. **46**: p. 389-392.
135. Strayer, A., et al., *Low Concentrations of a Silver-Based Nanocomposite to Manage Bacterial Spot of Tomato in the Greenhouse.* Plant Disease, 2015. **100**(7): p. 1460-1465.
136. Worthington, R.J., et al., *Foliar-Applied Small Molecule that Suppresses Biofilm Formation and Enhances Control of Copper-Resistant Xanthomonas euvesicatoria on Pepper.* Plant Disease, 2012. **96**(11): p. 1638-1644.
137. Paret, M.L., et al., *Photocatalysis: Effect of Light-Activated Nanoscale Formulations of TiO2 on Xanthomonas perforans and Control of Bacterial Spot of Tomato.* Phytopathology, 2012. **103**(3): p. 228-236.
138. Kim, J.S., et al., *Antimicrobial effects of silver nanoparticles.* Nanomedicine: Nanotechnology, Biology and Medicine, 2007. **3**(1): p. 95-101.
139. Bae, E., et al., *Bacterial cytotoxicity of the silver nanoparticle related to physicochemical metrics and agglomeration properties.* Environmental Toxicology and Chemistry, 2010. **29**(10): p. 2154-2160.
140. Elechiguerra, J.L., et al., *Interaction of silver nanoparticles with HIV-1.* Journal of Nanobiotechnology, 2005. **3**(1): p. 6.
141. Xu, Y., et al., *Exposure to TiO2 nanoparticles increases Staphylococcus aureus infection of HeLa cells.* Journal of Nanobiotechnology, 2016. **14**(1): p. 34.
142. Shrivastava, S., et al., *Characterization of enhanced antibacterial effects of novel silver nanoparticles.* Nanotechnology, 2007. **18**(22): p. 225103.
143. Yang, W., et al., *Food storage material silver nanoparticles interfere with DNA replication fidelity and bind with DNA.* Nanotechnology, 2009. **20**(8): p. 085102.

144. Esfandiari, N., A. Simchi, and R. Bagheri, *Size tuning of Ag-decorated TiO2 nanotube arrays for improved bactericidal capacity of orthopedic implants.* Journal of Biomedical Materials Research Part A, 2014. **102**(8): p. 2625-2635.
145. Premanathan, M., et al., *Selective toxicity of ZnO nanoparticles toward Gram-positive bacteria and cancer cells by apoptosis through lipid peroxidation.* Nanomedicine: Nanotechnology, Biology and Medicine, 2011. **7**(2): p. 184-192.
146. Sirelkhatim, A., et al., *Review on Zinc Oxide Nanoparticles: Antibacterial Activity and Toxicity Mechanism.* Nano-Micro Letters, 2015. **7**(3): p. 219-242.
147. Angelé-Martínez, C., et al., *Reactive oxygen species generation by copper(II) oxide nanoparticles determined by DNA damage assays and EPR spectroscopy.* Nanotoxicology, 2017. **11**(2): p. 278-288.
148. Xu, X., et al., *Antimicrobial Mechanism Based on H2O2 Generation at Oxygen Vacancies in ZnO Crystals.* Langmuir, 2013. **29**(18): p. 5573-5580.
149. Cheloni, G., E. Marti, and V.I. Slaveykova, *Interactive effects of copper oxide nanoparticles and light to green alga Chlamydomonas reinhardtii.* Aquatic Toxicology, 2016. **170**: p. 120-128.
150. Padmavathy, N. and R. Vijayaraghavan, *Interaction of ZnO nanoparticles with microbes--a physio and biochemical assay.* Journal of biomedical nanotechnology, 2011. **7**(6): p. 813-822.
151. Leung, Y.H., et al., *Mechanisms of Antibacterial Activity of MgO: Non-ROS Mediated Toxicity of MgO Nanoparticles Towards Escherichia coli.* Small, 2014. **10**(6): p. 1171-1183.
152. Hussein-Al-Ali, S.H., et al., *Synthesis, characterization, and antimicrobial activity of an ampicillin-conjugated magnetic nanoantibiotic for medical applications.* International journal of nanomedicine, 2014. **9**: p. 3801-3814.
153. Arakha, M., et al., *The effects of interfacial potential on antimicrobial propensity of ZnO nanoparticle.* Scientific Reports, 2015. **5**: p. 9578.
154. Picot, J., et al., *Flow cytometry: retrospective, fundamentals and recent instrumentation.* Cytotechnology, 2012. **64**(2): p. 109-130.
155. Bankier, C., et al., *A comparison of methods to assess the antimicrobial activity of nanoparticle combinations on bacterial cells.* PLOS ONE, 2018. **13**(2): p. e0192093.
156. Stuart, B.H., *Infrared Spectroscopy : Fundamentals and Applications*. 2004, Hoboken, UNITED KINGDOM: John Wiley & Sons, Incorporated.
157. Gué, M., et al., *Bacterial Swarming: A Biochemical Time-Resolved FTIR−ATR Study of Proteus mirabilis Swarm-Cell Differentiation.* Biochemistry, 2001. **40**(39): p. 11938-11945.
158. Lynch, I. and K.A. Dawson, *Protein-nanoparticle interactions.* Nano Today, 2008. **3**(1): p. 40-47.
159. Shang, L., et al., *pH-Dependent Protein Conformational Changes in Albumin:Gold Nanoparticle Bioconjugates: A Spectroscopic Study.* Langmuir, 2007. **23**(5): p. 2714-2721.
160. Khanal, D., et al., *Biospectroscopy of Nanodiamond-Induced Alterations in Conformation of Intra- and Extracellular Proteins: A Nanoscale IR Study.* Analytical Chemistry, 2016. **88**(15): p. 7530-7538.
161. Maniprasad, P. and S. Santra, *Novel Copper (Cu) Loaded Core–Shell Silica Nanoparticles with Improved Cu Bioavailability: Synthesis, Characterization and Study of Antibacterial Properties.* Journal of Biomedical Nanotechnology, 2012. **8**(4): p. 558-566.
162. Young, M., et al., *Multimodal Generally Recognized as Safe ZnO/Nanocopper Composite: A Novel Antimicrobial Material for the Management of Citrus Phytopathogens.* Journal of Agricultural and Food Chemistry, 2018. **66**(26): p. 6604-6608.

163. Schuster, K.C., E. Urlaub, and J.R. Gapes, *Single-cell analysis of bacteria by Raman microscopy: spectral information on the chemical composition of cells and on the heterogeneity in a culture.* Journal of Microbiological Methods, 2000. **42**(1): p. 29-38.
164. Nikiyan, H., A. Vasilchenko, and D. Deryabin, *Humidity-dependent bacterial cells functional morphometry investigations using atomic force microscope.* International journal of microbiology, 2010. **2010**: p. 704170-704170.